Quantum dynamics of a high impedance microwave cavity strongly coupled to a Josephson junction

Gianluca Aiello

université
PARIS-SACLAY

Quantum dynamics of a high impedance microwave cavity strongly coupled to a Josephson junction

Thèse de doctorat de l'Université Paris-Saclay

École doctorale n° 564, physique en Ile-de-France (PIF)
Spécialité de doctorat: Physique
Unité de recherche: Université Paris-Saclay, CNRS, Laboratoire de Physique des Solides, 91405, Orsay, France
Référent: Faculté des sciences d'Orsay

Thèse présentée et soutenue à Paris-Saclay, le 17 décembre 2020, par

Gianluca AIELLO

Composition du jury:

Richard DEBLOCK Directeur de recherche, Université Paris-Saclay, CNRS, Laboratoire de Physique des Solides, Orsay	Président
Olivier BUISSON Directeur de recherche, CNRS, Institut Néel, Grenoble	Rapporteur & examinateur
Benjamin HUARD Professeur, ENS de Lyon, CNRS, Laboratoire de Physique, Lyon	Rapporteur & examinateur
Hélène LE SUEUR Chargée de recherche, CEA, CNRS, Service de Physique de l'Etat Condensé, Saclay	Examinatrice
Ioan POP KIT Fellow, Karlsruher Institut für Technologie, Physikalisches Institut, Karlsruhe	Examinateur
Julien GABELLI Chargé de recherche, Université Paris-Saclay, CNRS, Laboratoire de Physique des Solides, Orsay	Directeur de thèse
Jérôme ESTEVE Chargé de recherche, Université Paris-Saclay, CNRS, Laboratoire de Physique des Solides, Orsay	Invité

Thèse de doctorat

NNT: 2020UPASP089

Acknowledgments

The results discussed in this thesis would have not been possible without the contribution of many people to whom I owe many thanks. First of all, I would like to thank my thesis advisors, Jérôme and Julien. You welcomed me when I joined the NS2 group for my master's thesis and you taught me all the basics of cryogenic and microwave physics. It was your passion for research, your determination, and your attention to detail that made me decide to continue my academic career with a PhD, under your guidance. Today, after four years and at the end of this experience, I can consider myself very happy with the choice I made. There have been difficulties and hard moments, but thanks to your help I have always been able to progress and obtain results of which I am proud.

A big thanks go also Marco Aprili, who more than anyone taught me that in research you have to be patient and that when things seem to go wrong you just need to sit down, have a coffee, and calmly try again. I would also like to thank Freek, with whom I shared the office all these years and who always gave me useful advice and encouragement.

Of course, life in the lab wouldn't have been the same without my friends Alexis, Marko, and Mathieu. I couldn't have hoped for better PhD teammates. You have made these years lighter and funnier.

Thanks also to Julien Basset, for sharing with me his passion for teaching, to Charis Quay and the whole Meso group, for the interesting discussions, and for always sharing with me their knowledge and expertise.

Sample fabrication was probably the hardest part of my PhD, but I am sure it would have been much harder without the help of Sylvie Gautier and Raphael Weil. Their patience in helping me with evaporators and the SEM has always been remarkable.

Some of the results described in this thesis were accomplished thanks to the collaboration of Claire Marrache, Louis Dumoulin, Hélène le Sueur, Fabien Portier, Carles Altimiras, and Iouri Moukharski that I want to thank for their help.

Finally, I would also like to thanks my friend and family for all the support they gave me outside the lab. Many thanks to Carlotta and Matteo: these years wouldn't have been the same without all the evenings we spent hanging out together. A huge thanks to my parents, Giuseppe and Rita, and my brother Simone for always pushing me to follow my passions and for doing everything they could to put me in condition to achieve all my goals. Lastly, the most important person that I have to thank is Cinzia. Deciding to do a PhD in a foreign country is not an easy choice to support, but you always did it with a smile and encouraging me to do my best. I am very lucky to have you.

Contents

Introduction

The development of the physics of Josephson junctions coupled to transmission line resonators has been fundamental for the development of circuit-QED [1–4], and has lead to the realization of a wide range of experiments, involving quantum circuits, both in the field of quantum optics [5–7] and quantum information [8–10]. In this thesis we aim to study the quantum dynamics of a high impedance and high finesse microwave resonator galvanically coupled to a dc biased tunnel Josephson junction, with Josepshon energy E_J and normal state resistance R_N, as schematically shown below:

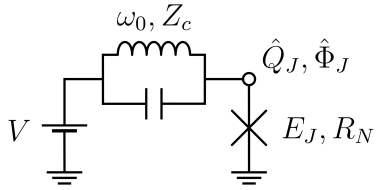

Figure 1: Schematic representation of the circuit consisting in a LC resonator, with characteristic impedance Z_c and resonant frequency ω_0, galvanically coupled to a dc biased Josephson junction, with energy E_J and normal state resistance R_N.

In this circuit, the electromagnetic mode of the resonator, here represented as a LC oscillator, is coupled to the transport of charges through the circuit: Cooper pairs as well as quasiparticles may tunnel while a photon is created or annihilated in the resonator mode. The order of magnitude of this coupling and the importance of quantum effects can be evaluated in the following way. The voltage seen by the junction is the sum of the dc bias V and the ac voltage of the LC resonator. This results in a flux at the junction terminals, which is the time integral of the voltage, that writes

$$\Phi_J = Vt - \sqrt{\frac{\hbar L^{1/2}}{2C^{1/2}}}(\hat{a} + \hat{a}^\dagger) = Vt - \Phi_0\sqrt{\frac{2Z_c}{\pi R_K}}(\hat{a} + \hat{a}^\dagger) \tag{1}$$

The first part of the equation comes from the quantification of the LC circuit in terms of creation and annihilation operators $\hat{a}^\dagger$ and $\hat{a}$, while the second one is the same expression rewritten in terms of the characteristic impedance of the mode $Z_c = \sqrt{L/C}$, the flux quantum $\Phi_0 = h/2e$ and the resistance quantum $R_K = h/e^2 \approx 25.8\,\mathrm{k}\Omega$. This second expression shows that quantum effects become important when the characteristic impedance Z_c is comparable to R_K.

Standard microwave resonators have a typical impedance close to $50\,\Omega$ and are thus far from the quantum regime. The quest for "superinductances", leading to large Z_c, has become an important direction of research with the long term goal of manipulating microwave signals

at the single photon level using dc voltages. Different routes have been followed including chains of Josephson junctions [11–13], structures with high electromagnetic inductance [14], or high kinetic inductance superconductors [15, 16]. In this thesis, we consider this last option and focus on two materials: NbSi and granular Aluminum. These materials have a much higher resistivity ($\sim 10^3$) at room temperature than conventional superconductors. As a consequence the density of Cooper pairs in the superconducting state is much smaller and, for a given super current, the kinetic energy of the pairs is large, giving rise to a large inductance. During this thesis, we have micro-fabricated resonators with modes resonating around 6 GHz and having a characteristic impedance up to 4.8 kΩ, together with a large quality factor (~ 20000). This combination of high impedance and high quality factor puts our experiment in an interesting regime where both quantum and out of equilibrium effects must be considered to describe the resonator state and the transport through the junction.

Dynamical Coulomb blockade and inelastic Cooper pair tunneling

Many early experiments considering the coupling between charge transport and the electromagnetic modes of a circuit focused on how the presence of these modes affect the transport properties of the junction. In the case where the modes have a rather low quality factor and a low impedance, a natural description is to consider that the modes remain at equilibrium and the current through the junction is obtained from the voltage fluctuations induced by the environment at the junction terminals [17–21]. This theory, known as $P(E)$ theory, predicts that for a normal junction coupled to a mode with resonant frequency ω_0, the tunnel current is reduced when the energy eV of the tunneling particle is below $\hbar\omega_0$. This prediction of a dynamical Coulomb blockade has been confirmed by many experiments starting with the ones in [22, 23].

In the case of Cooper pair tunneling in a Josephson junction, dynamical Coulomb blockade reduces as well the super-current at zero bias. But the presence of a mode at frequency ω_0 also results in a non-zero current below the gap in a narrow region of bias voltage around $2eV = \hbar\omega_0$. This current corresponds to the inelastic tunneling of Cooper pairs as shown in figure 2a: tunneling happens concomitantly with the emission of a photon in the environment mode, as first observed in [24].

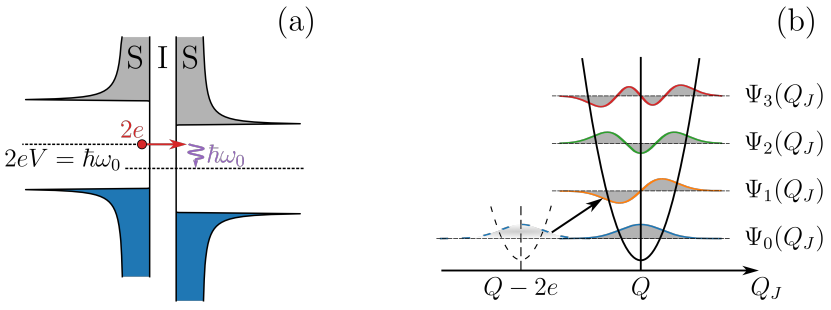

Figure 2: (a) Inelastic Cooper pair tunneling: when the voltage bias is such that $2eV = \hbar\omega_0$ a Cooper pair can tunnel and emit a photon in the resonator. (b) The tunneling process causes the charge of the resonator to change by $2e$. If the resonator is initially in the ground state, the matrix element for this process is proportional to the overlap between the wavefunctions $\Psi_0(Q_J - 2e)$ and $\Psi_1(Q_J)$.

Junction admittance and photo-assisted tunneling

In this thesis, we are more interested by how the junction affects the properties of the resonator. In the weak coupling regime, the response of a biased Josephson junction to a microwave signal can be described by a power dependent admittance function as measured and described in [25]. If the bias voltage is well below the gap, the junction can be approximated by an open circuit which reflects the incoming microwave signal. When the bias increases and becomes larger than $eV = 2\Delta - \hbar\omega_0$, a microwave photon can be absorbed by an electron tunneling through the junction as shown in figure 3a. Therefore the real part of the junction admittance sharply increases at $eV = 2\Delta - \hbar\omega_0$. If the incoming microwave power is strong, higher order photo-assisted tunneling processes are allowed and the real part of the admittance increases at voltages such that $eV > 2\Delta - m\hbar\omega_0$ where m is a positive integer. The dc tunneling current resulting from the absorption of the photons can be used as a sensitive wide-band detector of microwave signals [26]. Because of causality relations (Kramers-Kronig), the increase of the real part of the admittance corresponds to an increase of the imaginary part as measured in [25].

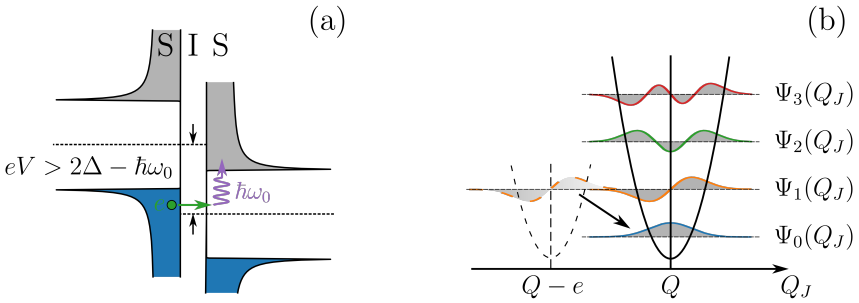

Figure 3: (a) Photo-assisted quasiparticle tunneling: when the voltage bias is such that $eV > 2\Delta - \hbar\omega_0$ electrons can tunnel by absorbing one photon from the mode. (b) The tunneling process translates the charge of the resonator by e. If the resonator initially contains a single photon, the corresponding matrix element for this process is given by the overlap between the wave-functions of the states $|1\rangle$ and $|0\rangle$.

When the junction is connected to a resonator, the results discussed above translate into the following scenario for the evolution of the resonator properties as a function of the bias voltage. When the bias voltage is well below the gap, the resonator is barely affected by the junction. When the bias approaches $eV = 2\Delta - \hbar\omega_0$, the imaginary part of the junction admittance increases, which results in a decrease of the resonance frequency of the resonator, while its linewidth remains constant as recently measured in [27]. When the voltage exceeds $eV = 2\Delta - \hbar\omega_0$, the junction absorbs photons from the resonator and its linewidth suddenly increases. For a high Q, high impedance resonator, the loss induced by the junction usually exceeds the coupling loss to the measurement lines by a large amount and the resonance signal vanishes.

Strong coupling regime

In the case where the mode has a high quality factor and is strongly coupled to the junction because its impedance Z_c is large, the coupling to the junction may bring the mode out of

equilibrium and a quantum description of the resonator field may be necessary. In such a situation, the $P(E)$ theory must be replaced by a master equation that describes the quantum evolution of the mode and compute the transport through the junction in a self consistent way. In [28], Gramich et al. develop the theory for the inelastic tunneling of Cooper pairs. They show that the circuit Hamiltonian can be reduced to the following Hamiltonian with one degree of freedom and is given by

$$\hat{H} = \hbar\omega_0 \left(\hat{a}^\dagger \hat{a} + \frac{1}{2}\right) - \frac{E_J}{2}\left(e^{2i\pi\hat{\Phi}_J/\Phi_0 - 2ieVt/\hbar} + e^{-2i\pi\hat{\Phi}_J/\Phi_0 + 2ieVt/\hbar}\right). \tag{2}$$

The first term is the Hamiltonian of the bare resonator mode, while the second term corresponds to the Josephson Hamiltonian with E_J being the Josephson energy that is proportional to $1/R_N$. The flux operator Φ_J has already been introduced in 1. The charge translation operator appearing in the Josephson term can be rewritten as

$$e^{2i\pi\hat{\Phi}_J/\Phi_0} = e^{i\Lambda_{\mathrm{cp}}(\hat{a}+\hat{a}^\dagger)}, \tag{3}$$

where $\Lambda_{\mathrm{cp}} = 2\sqrt{\pi Z_c/R_K}$ is a coupling parameter. In terms of charge and flux degrees of freedom, this operator displaces the charge Q_J, which is conjugate to Φ_J by $2e$. In more quantum optics terms, it displaces the resonator field by a quantity $i\Lambda_{\mathrm{cp}}$. The matrix element of this operator between the $|m\rangle$ and the $|m+l\rangle$ Fock states of the resonator is given by the overlap between the wavefunction $\Psi_m(Q_J - 2e)$ and $\Psi_{m+l}(Q_J)$ as pictured in 2b. This overlap has a non-trivial dependence on m when Λ_{cp} is on the order of unity. The steady state of the resonator is obtained by solving the master equation considering the Hamiltonian H and quantum jumps due to the losses of the resonator. In a recent work [29], Rolland et al. performed an experiment with a resonator such that $\Lambda_{\mathrm{cp}} \approx 1$. They show that antibunched photons are produced in the resonator, with a second order correlation function at zero delay equal to approximately 0.3. This is a consequence of the fact that the overlap between $\Psi_1(Q_J)$ and $\Psi_2(Q_J - 2e)$ cancels when $\Lambda_{\mathrm{cp}} = \sqrt{2}$.

The case of quasiparticle or electron tunneling in the quantum regime has attracted less attention and constitutes the heart of this thesis. In [30], Parlavecchio et al. have studied the behavior of a high impedance SQUID chain resonator coupled to a normal junction. But because the junction is normal, photons are always absorbed and the resonator mode remains empty, therefore the junction can still be mostly described in terms of admittance. In our experiment, the junction being a Josephson junction, there exists a voltage bias region ($2\Delta - 2\hbar\omega_0 < eV < 2\Delta - \hbar\omega_0$) where the Fock state $|1\rangle$ is not lossy and non trivial quantum dynamics happens because of quasiparticle tunneling. This tunneling Hamiltonian writes:

$$\hat{H}_I = T \sum_{k,q} \hat{c}^\dagger_{R,k} \hat{c}_{L,q} e^{i\frac{e}{\hbar}\left(\hat{\Phi}_J - Vt\right)} + \mathrm{h.c.} \tag{4}$$

where T is the tunneling energy that is inversely proportional to R_N, $\hat{c}_{L,q}$ and $\hat{c}^\dagger_{R,k}$ are operators describing the annihilation of an electron with wave vector q on the left side L of the junction and the creation of an electron with wave vector k on the right side R. The charge translation operator now translates the charge of the cavity by e, which is equivalent to a displacement of $i\Lambda_{\mathrm{qp}} = i\sqrt{\pi Z_c/R_k}$ in terms of $\hat{a}$ and $\hat{a}^\dagger$ operators. In contrast to the case of Cooper pair tunneling, this Hamiltonian couples the $\hat{a}$ mode to a large number of degrees of freedom and cannot be reduced to an Hamiltonian that only involve $\hat{a}$ operators. The

elimination of the electronic degrees of freedom rather leads to a quantum master equation as developed in [31]. By treating the electronic degrees of freedom as a Markovian bath at equilibrium, one obtains a master equation in the usual Lindblad form with Lamb shift terms and quantum jump terms. Because the matrix elements of the displacement operator are state dependent (see figure 3b), different Fock states of the resonator experience different frequency shifts and different exchange rates with the junction. The experiments shown in this thesis clearly demonstrate these effects.

Outline of the thesis

- Chapter 1 discusses the design and the properties of a high impedance microwave resonator made with a high kinetic inductance superconductor. In particular, we show how a distributed Bragg reflector (DBR) design allows us to obtain high quality and high impedance modes while keeping a galvanic (dc) coupling to the measurement line. We compute the different properties of the modes that will be used later as inputs in our theoretical models describing the coupling to the junction. For each mode, these properties are the resonance frequency, the characteristic impedance and the coupling loss to the measurement line.

- Chapter 2 is dedicated to experimental methods. We start by discussing the several fabrication processes we used for the realization of the high impedance cavities we tested. We then discuss the setup, both cryogenic and at room temperature, used for the microwave measurement of the cavity field and for the dc biasing of the junction. In conclusion, we characterize the properties of some test cavities and describe their behavior as a function of temperature and dc current using Mattis Bardeen theory.

- In Chapter 3, we present how the resonator modes evolve when the junction is biased close to the gap where quasiparticle tunneling happens. We discuss two models used to describe the data and we show how, in the strong coupling regime, our experimental results are best explained by a master equation treatment of the resonator mode. We observe a Lamb shift which is different for the $|1\rangle$ and $|2\rangle$ Fock states. And we show that when $2\Delta - 2\hbar\omega_0 < eV < 2\Delta - \hbar\omega_0$, the dynamics of the resonator mode is reduced to the subspace spanned by the $|0\rangle$ and $|1\rangle$ states. The resonator mode then behaves as a two-level system.

- Chapter 4 shows the results obtained when measuring the photon emission, due to inelastic Cooper pair tunneling, in the 6 GHz mode of the cavity. We observe more than 70 emission peaks, as a function of the voltage bias, that are linked to high order non-linear processes. We explain the data using a semi-classical approach which consists in using classical stochastic differential equations to simulate quantum trajectories.

Chapter 1

Sample design and electromagnetic simulations

Contents

The coupling Λ between a lumped element resonator and a junction can be written in terms of the resonator zero points fluctuations that are directly proportional to the characteristic impedance of the resonator. In this chapter we discuss how to compute Λ when the resonator is not a lumped circuit but corresponds to the resonant mode of an extended cavity. We consider an high finesse cavity realized using a distributed Bragg reflector (DBR) that involves several pieces of transmission lines with different impedance. We show that the coupling depends on the impedance of the cavity and on the confinement of the mode in the DBR structure. We apply these results to two different DBR designs. We use a 1D transfer matrix method to numerically compute the spatial distribution of the mode in the line and we discuss how the properties of the modes depend on the design of the DBR.

In section 1.3 we compare the results obtained with the transfer matrix method, with the ones derived using Sonnet, a microwave simulation software. We show that in presence of lines with different geometrical width, the 1D model only predicts the resonant frequency and the impedance of the modes while highly overestimating the coupling rate.

In the last part, we discuss the design chosen for the realization of the sample and how the presence of the junction affects the properties of the modes.

1.1 Junction cavity coupling

In this section we discuss how to derive the hamiltonian and the spatial dependence of the electromagnetic modes, in a structure made by a distributed cavity with a DBR. We do so in order to derive the expression of the mode zero point fluctuations that we use to calculate the coupling to the junction. We show that we can write Λ in terms of an effective characteristic impedance, $\tilde{Z}$, that depends on the impedance of the cavity and on the confinement of the mode, which we quantify through the mode "volume". This definition is equivalent to the one commonly found in literature, where $\tilde{Z}$ is related to the derivative of the admittance of the circuit seen by the junction. Both of them are used to design a circuit with the highest possible Λ.

We start by considering a cavity with a DBR that is connected to a grounded junction placed at its end. The DBR is made of $N-1$ pieces of transmission lines that alternates high and low impedance such that $Z_{2i-1} > Z_{2i}$ (fig. 1.1), with Z_i being the impedance of the i-th line and given by $\sqrt{L_{l_i}/C_{l_i}}$. C_{l_i} and L_{l_i} are the capacitance and inductance per unit length. The N-th element of the circuit is the high impedance cavity that is connected to the junction. The length of each line is $l_i = x_i - x_{i-1}$ and the total length of the structure is x_N. The impedance mismatch between the lines can be achieved by using lines with different geometrical width or with different kinetic inductance. Here we compute the hamiltonian of the modes under the assumption that the reflection coefficient at the interface between the cavity and the junction is one. We thus consider the cavity to be open at $x = x_N$. We will later better discuss this approximation and see that it is valid if the impedance of the junction is much larger than the impedance of the lines realizing the DBR structure[1]. At $x = 0$ the DBR is connected to a $Z_0 = 50\,\Omega$ line that is used to excite the modes of the structure.

[1] Typical values of junction's impedance are around $200\,\mathrm{k}\Omega$, while superconducting lines have an impedance of few $\mathrm{k}\Omega$

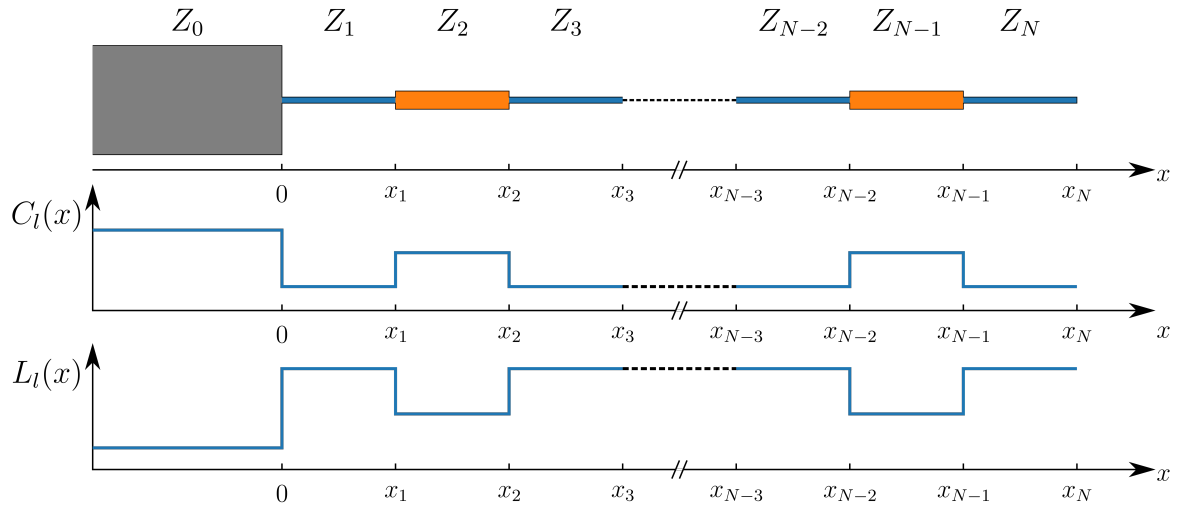

Figure 1.1: Scheme of the DBR cavity. A structure made of several transmission lines (here in microstrip geometry) with alternating high and low impedance. The impedance mismatch, is achieved using lines with different geometrical width or with different kinetic inductance. The capacitance $C_l(x)$ and inductance $L_l(x)$ per unit length depend on the position x as step like functions. The DBR is connected on one side to a $Z_0 = 50\,\Omega$ line and to a grounded junction to the other.

1.1.1 Cavity mode volume and characteristic impedance

Using the flux as degree of freedom, the Lagrangian of the field in the circuit is [32]:

$$\mathcal{L} = \int_0^{x_N} dx \left[\frac{C_l(x)}{2} \left(\frac{\partial \Phi(x,t)}{\partial t} \right)^2 - \frac{1}{2L_l(x)} \left(\frac{\partial \Phi(x,t)}{\partial x} \right)^2 \right], \tag{1.1}$$

where $C_l(x)$ and $L_l(x)$ are the capacitance and inductance per unit length that depend on the position x as step like functions (figure 1.1). To obtain the coupling parameter Λ to the junction, we expand the flux in the normal modes basis as:

$$\Phi(x,t) = \sum_{n=0}^{\infty} \phi_n(t)\varphi_n(x), \tag{1.2}$$

where $\phi_n(t)$ is the amplitude of the n-th resonant mode of the structure with spatial dependence $\varphi_n(x)$. Because the resonator is open on one side and connected to a $50\,\Omega$ line on the other, a strict mathematical definition of the modes can be complicated due to the leakage of the mode towards $x \to -\infty$. In order to overcome this problem, we follow the standard approach that consists in neglecting the leaky part of the mode and setting it to zero. It will be later reincorporated as a loss term with the loss rate κ_c.

The boundary conditions for $\varphi_n(x)$ are therefore:

$$\varphi_n(0) = 0, \qquad \left. \frac{\partial \varphi_n(x)}{\partial x} \right|_{x=x_N} = 0. \tag{1.3}$$

The boundary condition at $x = x_N$ corresponds to the zero current due to the open end of the line while the one at $x = 0$ is the approximation of small leakage discussed above.

Together with the second order differential equation

$$\frac{1}{L_l(x)}\frac{\partial^2\varphi_n(x)}{\partial x^2} = -\omega_n^2 C_l(x)\varphi_n(x), \tag{1.4}$$

the boundary conditions define a generalized eigenvalue problem whose solutions are the resonant modes of the DBR structure. They verify the following orthogonality relations:

$$\int_0^{x_N} dx\,[C_l(x)\varphi_n(x)\varphi_m(x)] = \tilde{C}_n\delta_{nm}, \tag{1.5}$$

$$\int_0^{x_N} dx\left[\frac{1}{L_l(x)}\left(\frac{\partial\varphi_n(x)}{\partial x}\right)\left(\frac{\partial\varphi_m(x)}{\partial x}\right)\right] = \omega_n^2\tilde{C}_n\delta_{nm}, \tag{1.6}$$

where $\tilde{C}_n$ is a normalization constant with the unit of a capacitance.

Because $C_l(x)$ and $L_l(x)$ are step like functions , the $\varphi_n(x)$ function is a piecewise function:

$$\varphi_n(x) = \begin{cases} \varphi_{n,1}\cos(k_{n,1}x + \alpha_1) & 0 < x < x_1 \\ \quad\vdots & \\ \varphi_{n,N}\cos(k_{n,N}x + \alpha_N) & x_{N-1} < x < x_N \end{cases} \tag{1.7}$$

with $k_{n,i} = \omega_n\sqrt{L_{l_i}C_{l_i}}$. The $\varphi_{n,i}$ and α_i are the amplitudes and phases in the section i. The Lagrangian 1.1 therefore becomes:

$$\mathcal{L} = \sum_{n=0}^{\infty}\frac{\tilde{C}_n}{2}\left(\frac{\partial\phi_n}{\partial t}\right)^2 - \frac{\tilde{C}_n}{2}\omega_n^2\phi_n^2. \tag{1.8}$$

The corresponding Hamiltonian is:

$$H = \sum_n \frac{Q_n^2}{2\tilde{C}_n} + \frac{\tilde{C}_n}{2}\omega_2^2\phi_n^2, \tag{1.9}$$

with $Q_n = \tilde{C}_n(\partial\phi_n/\partial t)$. Its quantization is straightforward and introducing the creation operator $\hat{a}_n^\dagger$ for the n-th mode, we obtain:

$$H = \sum_n \hbar\omega_n\left(\hat{a}_n^\dagger\hat{a}_n + \frac{1}{2}\right), \tag{1.10}$$

with:

$$\hat{Q}_n = i\sqrt{\frac{\hbar\omega_n\tilde{C}_n}{2}}(\hat{a}_n^\dagger - \hat{a}_n), \qquad \hat{\phi}_n = \sqrt{\frac{\hbar}{2\omega_n\tilde{C}_n}}(\hat{a}_n^\dagger + \hat{a}_n). \tag{1.11}$$

In the simplest case, the resonator consists of a simple $\lambda/4$ resonator made of an high impedance section of length x_1 ($x_N = x_1$) (fig. 1.2). The φ_n modes are then given by:

$$\varphi_n(x) = \cos\left(k_n x - (2n+1)\frac{\pi}{2}\right) \tag{1.12}$$

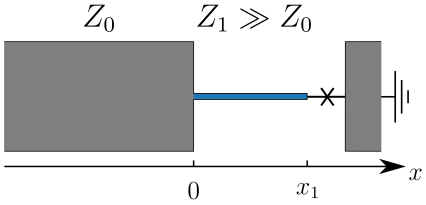

Figure 1.2: $\lambda/4$ cavity directly coupled to a 50 Ω line. The $\varphi_n(x)$ modes have a cosine shape with a maximum at $x = x_1$. The coupling Λ is proportional to $\sqrt{Z_1}$ and it is maximum for the $n = 0$ mode.

with $k_n = \omega_n\sqrt{L_{l_1}C_{l_1}} = (2n+1)\pi/(2x_1)$. The mode function $\varphi_n(x)$ has a maximum of one when $x = x_1$.

In order to maximize the coupling Λ_n, the junction must be connected at the end of the DBR. From equation 1.5, we obtain: $\tilde{C}_n = C_{l_1}x_1/2$. The flux, due to the n-th mode, at the position of the junction $x_J = x_1$ is then:

$$\hat{\phi}_n\varphi_n(x_1) = \sqrt{\frac{\hbar}{2\omega_n\tilde{C}_n}}(\hat{a}_n^\dagger + \hat{a}_n) = \sqrt{\frac{2\hbar Z_1}{(2n+1)\pi}}(\hat{a}_n^\dagger + \hat{a}_n), \tag{1.13}$$

with $Z_1 = \sqrt{L_{l_1}/C_{l_1}}$. Comparing this result to the lumped element case we obtain:

$$\Lambda_{n,\mathrm{cp}} = 4\sqrt{\frac{Z_1}{(2n+1)R_K}}, \tag{1.14}$$

while $\Lambda_{n,\mathrm{qp}} = \Lambda_{n,\mathrm{cp}}/2$. In the case of a DBR with more sections, we look for $\varphi_n(x)$ functions such that $\varphi_n(x_J)$ is one as above. The expression of the coupling is then given by 1.14:

$$\Lambda_{n,\mathrm{cp}} = 2\sqrt{\pi\frac{\tilde{Z}_n}{R_K}}, \tag{1.15}$$

where $\tilde{Z}_n$ is the effective characteristic impedance of the n-th mode as seen by the junction. It is given by:

$$\tilde{Z}_n = \frac{1}{\omega_n\tilde{C}_n} = \frac{1}{\omega_n}\left(\int_0^{x_N} dx\left[C_l(x)\varphi_n(x)^2\right]\right)^{-1}, \tag{1.16}$$

with $\varphi_n(x_J) = 1$.

In quantum optics, the coupling strength to a cavity is inversely proportional to the square root of the mode volume. Here, we recover this property by defining the mode "volume" v_n as:

$$v_n = \int_0^{x_N} dx\left[\frac{C_l(x)}{C_N}\varphi_n^2(x)\right], \tag{1.17}$$

such that $\tilde{C}_n = v_nC_N$, where C_N is the capacitance per unit length in the last section of the DBR. Because the resonator is a 1D structure, the mode volume has here the dimension of a length. The coupling can be rewritten as:

$$\Lambda_{n,\mathrm{cp}} = \sqrt{\frac{4\pi}{\omega_nC_Nv_nR_K}} = \sqrt{\frac{2\lambda_n}{v_n}\frac{Z_N}{R_K}}, \tag{1.18}$$

where λ_n is the wavelength of the n-th modes in the last section. The minimal mode volume is obtained for the fundamental mode of a $\lambda/4$ where $v_1 = x_1/2 = \lambda_1/8$. Adding more sections decreases the coupling because the mode volume increases. The concept of mode volume can be helpful to design a structure with a large coupling by trying to minimize the integral of $C_l(x)\varphi_n^2(x)$ while keeping the quality factor to the desired value.

1.1.2 Admittance seen by the junction

In the previous paragraph, we have seen that the coupling parameter $\Lambda_{n,\mathrm{cp}}$ of the n-th cavity mode to the junction is directly proportional to the square root of a characteristic impedance $\tilde{Z}_n$ defined as:

$$\tilde{Z}_n = \frac{\lambda_n}{2\pi v_n} Z_N. \tag{1.19}$$

If the mode is well confined and the junction connected at a flux maximum, then $v_n \simeq \lambda_n/8$ and $\tilde{Z}_n \simeq 4Z_N/\pi$. The equality is reached in the case of a $\lambda/4$ resonator with one section of a high impedance line $Z_N \gg Z_0$. Physically, the impedance $\tilde{Z}_n$ gives the voltage amplitude of the zero point fluctuations of the n-th mode at the position of the junction.

Supposing that the cavity is excited at $\omega = \omega_n$, the average of the two energy terms in the Lagrangian are equal:

$$\frac{\tilde{C}_n}{2}\langle\dot{\phi_n^2}\rangle = \frac{\tilde{C}_n}{2}\omega_n^2\langle\phi_n^2\rangle = \frac{W}{2}. \tag{1.20}$$

where W is the average energy stored in the cavity. We can rewrite:

$$W = \frac{\langle V_n^2\rangle}{\tilde{Z}_n\omega_n}, \tag{1.21}$$

where V_n is the voltage amplitude of the n-th mode at the position of the junction.
Again if we neglect the energy leakage due to the coupling to the Z_0 line, the energy stored in the cavity can be expressed as [33, 34]:

$$W = \frac{\langle V_n^2\rangle}{2i}\frac{\partial Y(\omega)}{\partial\omega}\Big|_{\omega=\omega_n}, \tag{1.22}$$

where Y is the admittance seen by the junction. We then obtain:

$$\tilde{Z}_n = \frac{2i}{\omega_n}\left(\frac{\partial Y(\omega)}{\partial\omega}\Big|_{\omega=\omega_n}\right)^{-1}. \tag{1.23}$$

This formula is the one often used in the literature to define the coupling $\Lambda_{n,\mathrm{cp}}$.

We can check that we indeed recover the same impedance as the one defined in 1.16 in the case of a $\lambda/4$ cavity. The admittance seen by the junction is:

$$Y(\omega) = Y_1\frac{Y_0 + iY_1\tan(kl_1)}{Y_1 + iY_0\tan(kl_1)}, \tag{1.24}$$

with $Y_{0,1} = 1/Z_{0,1}$. When $Y_1 \ll Y_0$, the small leakage approximation is valid and we recover our previous result:

$$\tilde{Z}_n = \frac{4}{(2n+1)\pi}Z_1. \tag{1.25}$$

The formula 1.23 is easier to use than 1.16 when dealing with numerical simulations made with an electromagnetic simulation software like Sonnet.

1.2 1D model simulations

We now want to apply the results previously discussed to different kinds of geometry in order to understand how the coupling Λ_n and the electromagnetic properties of the modes depend on the design of the circuit. To do so, we describe the circuit under study with a 1D model and we assume that the transversal component of voltage and current are negligible. By using the transfer matrix method we compute the admittance seen by the junction, from which we obtain the resonant frequency and the effective characteristic impedance of the modes. With the transfer matrix method we also calculate space dependence of voltage and current that allow us to obtain the mode zero point fluctuations and volume. We apply this method to two different DBR designs and we discuss the features of their modes.

1.2.1 Transfer matrix method

In a two port network, as the one shown schematically in figure 1.3, we can relate voltage and current measured at two different ports through the transfer matrix T of the circuit that connects the ports [35]:

$$\begin{bmatrix} V_2 \\ I_2 \end{bmatrix} = T \begin{bmatrix} V_1 \\ I_1 \end{bmatrix}, \tag{1.26}$$

with $V_{1,2}$ and $I_{1,2}$ being the voltage and current measured at port 1 and 2.

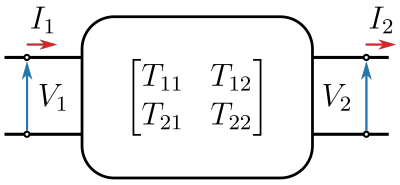

Figure 1.3: Schematics of a two port network device. The voltage and the current measured at the two ports are related through the transfer matrix of the circuit T.

The advantage of this method is that the transfer matrix of a cascade connection of two-ports networks is simply given by the product of the matrices representing the individual two-ports circuit. This is particularly useful when dealing with DBR structures composed of several pieces of transmission lines connected with each other.

To analyze the properties of the modes of a cavity with DBR we start by calculating the total transfer matrix of the circuit. We place the first port at the position of the junction (in our case at the end of the circuit $x = x_N$) and the second one at $x = 0$. The total matrix T is given by:

$$T = \prod_{i=1}^{N} T_{l_i}, \tag{1.27}$$

with T_{l_i} being the matrix of the i-th lossless section and equivalent to:

$$T_{l_i} = \begin{bmatrix} \cos(k_i l_i) & iZ_i \sin(k_i l_i) \\ iY_i \sin(k_i l_i) & \cos(k_i l_i) \end{bmatrix}. \tag{1.28}$$

We then convert the matrix T to the admittance matrix y. Its elements y_{ij} are defined as the ratio between the short circuit current measured at port i and the driving voltage applied at port j, and can be calculated, starting from the transfer matrix elements T_{ij}, though [35]:

$$y_{11} = \frac{T_{22}}{T_{12}}, \qquad y_{12} = \frac{T_{12}T_{21} - T_{11}T_{22}}{T_{12}}, \qquad y_{21} = -\frac{1}{T_{12}}, \qquad y_{22} = \frac{T_{11}}{T_{12}}. \tag{1.29}$$

As last step, we replace the port at $x = 0$ with a $Y_0 = 1/50\,\Omega^{-1}$ admittance to obtain the admittance $Y(\omega)$ seen by the junction:

$$Y(\omega) = y_{11} - y_{12} - y_{12}\frac{y_{22} + y_{12} + Y_0}{y_{22} + Y_0}. \tag{1.30}$$

We calculate the resonant frequency of the modes by solving the equation $\mathrm{Im}[Y(\omega)] = 0$, while their characteristic impedance is obtained using eq. 1.23. To compute the spatial dependence and the mode volume of the modes, we impose the open circuit boundary condition to the port connected to the junction ($x = x_N$) and we solve the transfer matrix equation, at $\omega = \omega_n$, with the second port placed at different positions x. Because the spatial dependence of voltage and flux is the same, solving equation 1.26 gives us directly $\varphi_n(x)$. To calculate v_n, we normalize the transfer matrix solution such that $\varphi_n(x_N) = 1$ and we compute the integral 1.17. Because the transfer matrix simulation contains a leaky term, it does not fulfill the exact boundary condition at $x = 0$. But, since we deal with high quality factor structures only, this lead to a negligible error on the mode volume and on the coupling factor Λ_n.

Last, from the knowledge of voltage and current at $x = 0$, we compute the reflection spectrum of the cavity defined as:

$$S_{11} = \frac{V(0) - Z_0 I(0)}{V(0) + Z_0 I(0)}, \tag{1.31}$$

whose linewidth allow us to calculate the coupling rate κ_c of the modes.

1.2.2 Characterization of the modes

The properties of the modes of a cavity with DBR mainly depend on the total number of layers N making the circuit and on the impedance mismatch between the layers. Here we take in consideration two possible designs, both in microstrip geometry and with $N = 3$ layers. In both designs, the first and the last layer (the cavity) are realized using an high impedance superconductor and they have the same geometry. For the layer $N = 2$, in the first design, we use again an high impedance superconductor and we achieve impedance mismatch between the layers by a geometrical width mismatch ($w_2 > w_1$). In the second design we use a superconductor with low impedance and, because of the different inductance of the various layers, the impedance mismatch can be very high and enhanced even more by using lines with different widths.

Design I: high impedance DBR

The design we are considering is the one shown in figure 1.4. All the layers are realized using the same high impedance superconductor. The first one is an exact replica of the cavity: they have the same geometrical dimension ($w_1 = w_3$, $l_1 = l_3$) and the same impedance

$Z_1 = Z_3$. The layer $N = 2$ is wider ($w_2 > w_1$) in order to ensure a good impedance mismatch ($Z_{1,3} > Z_2$). The total length of the structure is $2l_1 + l_2$ and l_1 is chosen such that $\pi v_{p_1}/(2l_1) = 2\pi \times 6\,\mathrm{GHz}$, with v_{p_1} being the phase velocity in the cavity layer. The length l_2 is adjusted to match the Bragg resonance condition ($l_2 = \lambda_2/4$). With x_1, x_2 and x_3 we indicate the delimitation of the various elements.

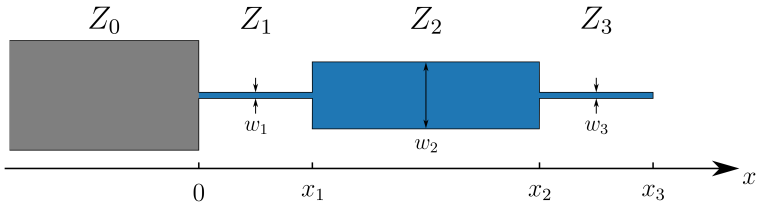

Figure 1.4: Scheme of the first DBR design realized using an high impedance superconductor for all the layers. The geometry of the first layer is identical to the one of the cavity while the second layer has to be wider in order to ensure impedance mismatch. For the transfer matrix calculation we place port 1 at $x = x_3$ and port 2 at $x = 0$.

Typical values of kinetic inductance per square for high impedance superconductor are around $L_k = 1\,\mathrm{nH}/\square$. For a few µm wide microstrip the electromagnetic contribution to the inductance is negligible while the capacitance per unit length C_l can be calculated using [36]:

$$C_l = \frac{\epsilon_r}{60\,c \ln\left(\frac{8h}{w} + \frac{4w}{h}\right)}, \tag{1.32}$$

where ϵ_r is the relative permittivity of the dielectric that separates the line and the ground, h is the thickness of the dielectric, w is the width of the microstrip and c is the speed of light in vacuum.

We start the analysis of the circuit by looking at the resonant frequency and characteristic impedance of the modes. We calculate them from the admittance seen by the junction, obtained using the transfer matrix method and we plot the results in fig. 1.5. The parameters used are: $w_1 = 1\,\mu\mathrm{m}$, $w_2 = 20\,\mu\mathrm{m}$, $l_1 = 142\,\mu\mathrm{m}$ and $l_2 = 500\,\mu\mathrm{m}$. In figure 1.6a we plot the phase of the spectrum S_{11} that we calculate using equation 1.31. Because we are considering the case of lossless transmission lines $|S_{11}|^2 = 1$ at all frequencies. From the fit of $\arg(S_{11})$, performed close to resonant frequencies, we extract the coupling rate of each mode, as shown in figure 1.6b for the $2\pi \times 6\,\mathrm{GHz}$ mode.

The analysis of the spectrum shows that the circuit with the DBR has more resonances with respect to the quarter wavelength cavity alone. Among all these modes only the first green one and all the red ones of figure 1.5 have a strong junction-cavity coupling. We understand the reason by looking at $\varphi_n(x)$ (fig. 1.7) for the first four modes and computing their effective mode impedance. The mode at $2\pi \times 6\,\mathrm{GHz}$ (fig. 1.7b), has the highest characteristic impedance ($3.6\,\mathrm{k}\Omega$) and this is related to the fact that $|\varphi(x)|^2$ has a maximum at the position of the junction and that its mode volume ($0.08\,\mathrm{mm}$) is close to the minimum value $l_1/2$. The mode at $2\pi \times 1.4\,\mathrm{GHz}$ (fig. 1.7a) also has a maximum of $|\varphi(x)|^2$ at $x = x_3$, but unlike the $2\pi \times 6\,\mathrm{GHz}$ mode, it has a bigger mode volume ($0.8\,\mathrm{mm}$) and therefore a smaller characteristic impedance ($1.6\,\mathrm{k}\Omega$). The last two modes, at $2\pi \times 10.6\,\mathrm{GHz}$ and $2\pi \times 13.4\,\mathrm{GHz}$ (1.7c and d), have the same mode volume than the $2\pi \times 1.4\,\mathrm{GHz}$ mode ($0.8\,\mathrm{mm}$) but they

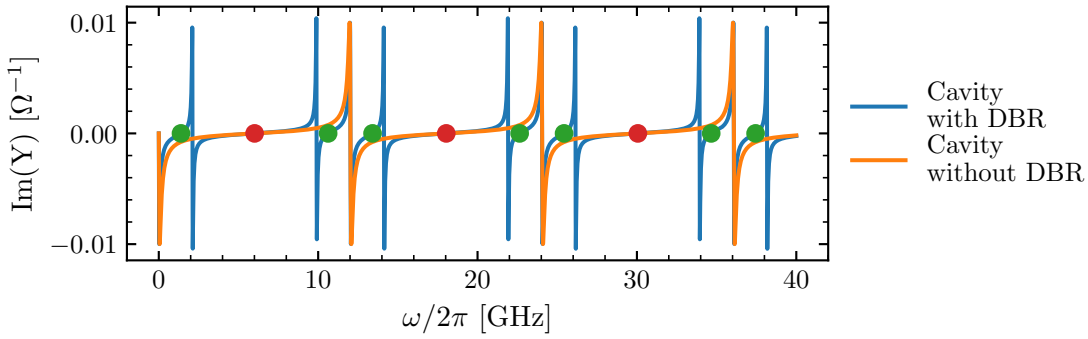

Figure 1.5: DBR design I: (a) imaginary part of the admittance seen by the junction for a cavity with DBR (in blue) with w_2/w_1 and for a cavity alone (in orange).The colored dots indicate the zeros of the admittance which corresponds to resonant modes of the circuit. The red points the resonances that are in common with a quarter wavelength cavity while in orange we indicate the extra ones due to the DBR

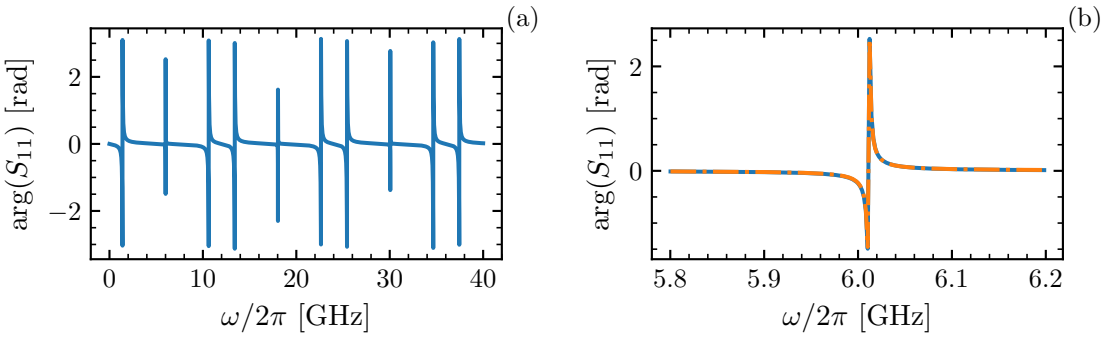

Figure 1.6: (a) Phase of the reflected spectrum of the cavity with the DBR. Every 2π phase shift corresponds to a resonance of the circuit. (b) Spectrum close to the $2\pi \times 6\,\mathrm{GHz}$ mode together with the fit (in orange) from which we extract the coupling rate of the mode.

are mainly confined in the first layer of the DBR with their maximum far from the port. Therefore their impedance is small ($210\,\Omega$ and $160\,\Omega$).

Because the low characteristic impedance modes have a small junction-cavity coupling Λ_n, we only focus on the high impedance ones. Their properties depend on the impedance mismatch between the layers of Bragg which, for this kind of design, means that they depend on the width ratio w_2/w_1. We fix $w_1 = w_3 = 1\,\mu\mathrm{m}$ and we compute the electromagnetic properties of the modes for different values of w_2, keeping into account that when changing w_2 the length l_2 has to be adjusted in order to fulfill the Bragg resonance condition. In fig. 1.8 we show the variation of the resonant frequency, of the coupling κ_c, of the effective mode impedance and the mode volume for the $n = 0$ mode. The big change of resonant frequency, shown in fig. 1.8a is due to change of l_2 and is less related to the change of impedance mismatch. The coupling rate is almost constant and around $2\pi \times 50\,\mathrm{MHz}$. The effective mode impedance decreases as we increase the width ratio and is due to an increase of the

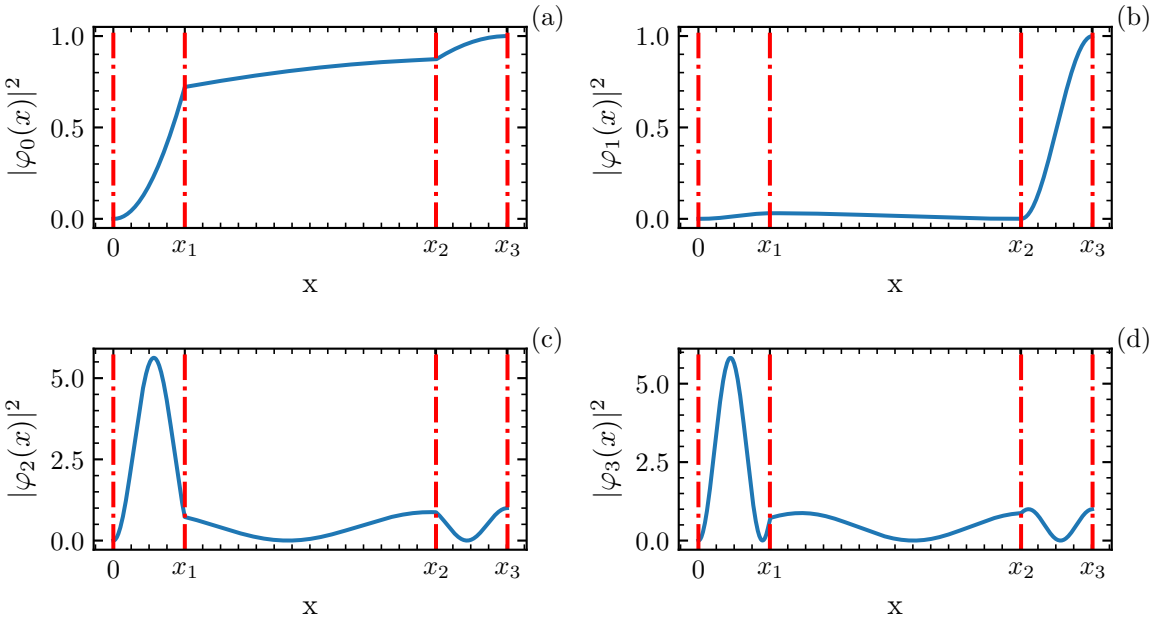

Figure 1.7: DBR design I: spatial distribution $\varphi(x)$ of the first four modes. (a) $\omega_0 = 2\pi \times 1.5\,\mathrm{GHz}$, $\tilde{Z}_0 = 1.6\,\mathrm{k\Omega}$, $v_0 = 0.83\,\mathrm{mm}$. (b) $\omega_1 = 2\pi \times 6\,\mathrm{GHz}$ $\tilde{Z}_1 = 3.6\,\mathrm{k\Omega}$, $v_1 = 0.08\,\mathrm{mm}$. (c) $\omega_2 = 2\pi \times 10.6\,\mathrm{GHz}$, $\tilde{Z}_2 = 210\,\Omega$, $v_2 = 0.83\,\mathrm{mm}$. (d) $\omega_3 = 2\pi \times 13.4\,\mathrm{GHz}$, $\tilde{Z}_3 = 160\,\Omega$, $v_3 = 0.83\,\mathrm{mm}$.

mode volume. To evaluate the effects of the DBR on the $2\pi \times 6\,\mathrm{GHz}$ mode we compare it to the same mode of a quarter wavelength cavity realized with the same geometry and same L_k. In table 1.1 we report the parameters of the mode in the case of the cavity, while in fig. 1.9 we plot the variation of the same parameters as a function of the DBR width mismatch.

$\kappa_c/2\pi$ [MHz]	$\tilde{Z}_n$[kΩ]	v_n[mm]
110	4.3	0.14

Table 1.1: Properties of the first mode of a $\lambda/4$ cavity realized with the same geometry and inductance as the cavity in DBR design I.

The coupling rate, even for small width ratio, it is much smaller than the bare cavity's one. As expected, it decreases when increasing w_2/w_1 as the impedance's mismatch increases. It ranges from around $2\pi \times 15\,\mathrm{MHz}$ to $2\pi \times 180\,\mathrm{kHz}$. At the same time, the mode impedance approaches the bare cavity's one as the width ratio increases. This is due to the fact the modes volume diminishes as the mode is more confined in the cavity.

Design II: low impedance DBR

The second design we discuss is obtained replacing the high impedance superconductor making the second layer with a low impedance one, as shown in figure 1.10.

In this case the impedance mismatch between the layers is much higher and doesn't require a geometrical width mismatch to be achieved. We perform the same analysis as before and

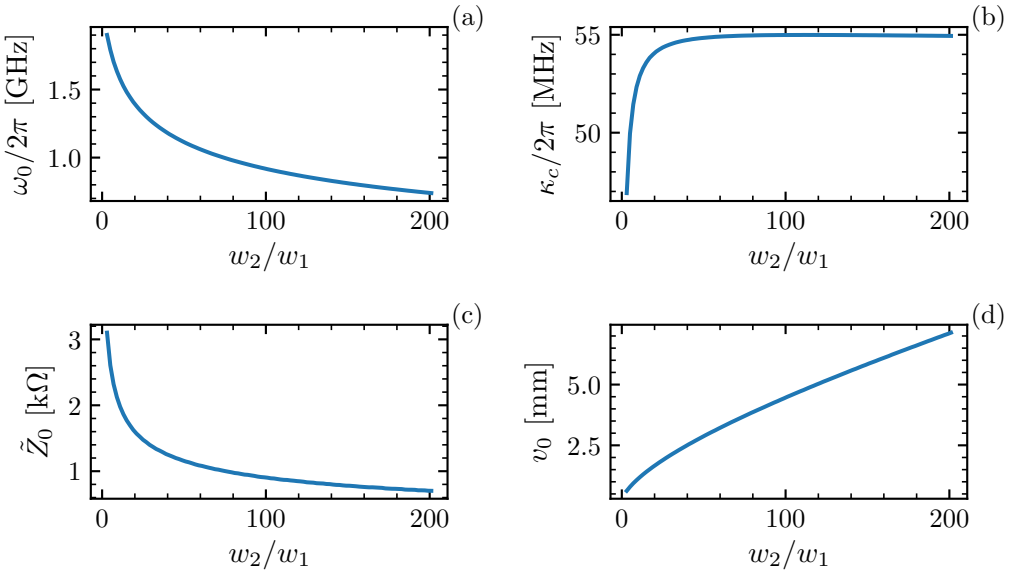

Figure 1.8: DBR design I: (a) Resonance frequency, (b) coupling rate, (c) characteristic mode impedance and (d) mode volume for the first resonant mode as function of the width mismatch between the layers.

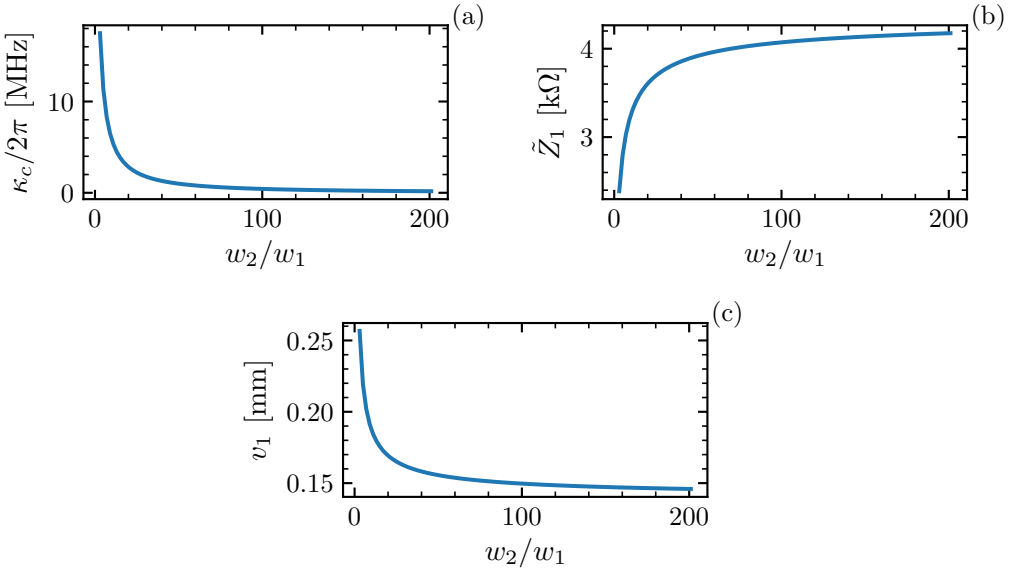

Figure 1.9: DBR design I: (a) Coupling rate, (b) characteristic mode impedance and (c) mode volume for the second resonant mode as function of the width mismatch between the layers. All the parameters are evaluated at the resonant frequency of the mode that remains constant and equal to $2\pi \times 6\,\mathrm{GHz}$

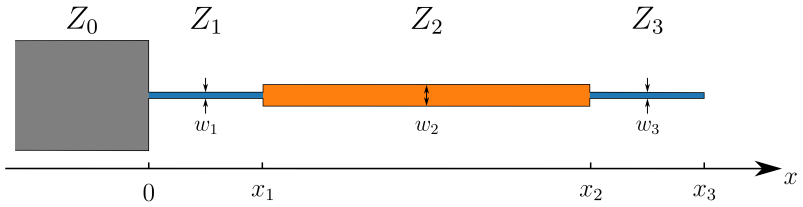

Figure 1.10: Scheme of the second DBR design. The first and the last layer are realized using an high impedance superconductor and have the same geometry. The second layer, instead, is a low impedance one. For the transfer matrix calculation the two ports are placed again on the two ends of the circuit.

we study the properties of the DBR as function of the width ratio w_2/w_1. We consider again an high impedance transmission line with $L_k = 1\,\mathrm{nH}/\square$ and a fixed width of $1\,\mu\mathrm{m}$ for the first and third layer, while we change the width of the second one, whose electromagnetic inductance is evaluated using [37]:

$$L_l = \frac{60}{c} \ln\left(\frac{8h}{w} + \frac{w}{4h}\right). \tag{1.33}$$

In figure 1.11 we show the properties of the low frequency $n = 0$ mode while in figure 1.12 we plot the same for the $n = 1$ mode.

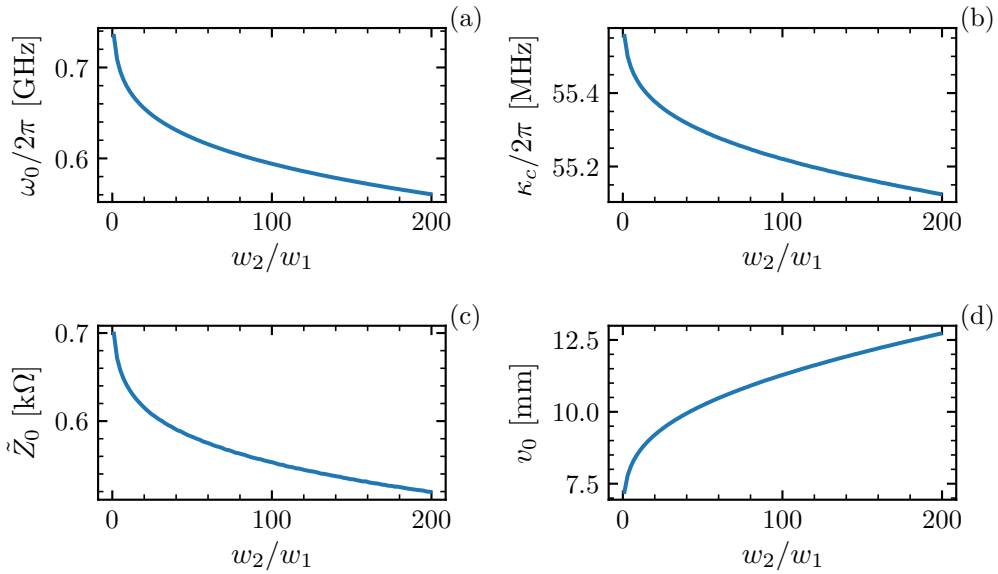

Figure 1.11: DBR design II: (a) Resonance frequency, (b) coupling rate, (c) characteristic mode impedance and (d) mode volume for the first resonant mode as function of the width mismatch between the layers.

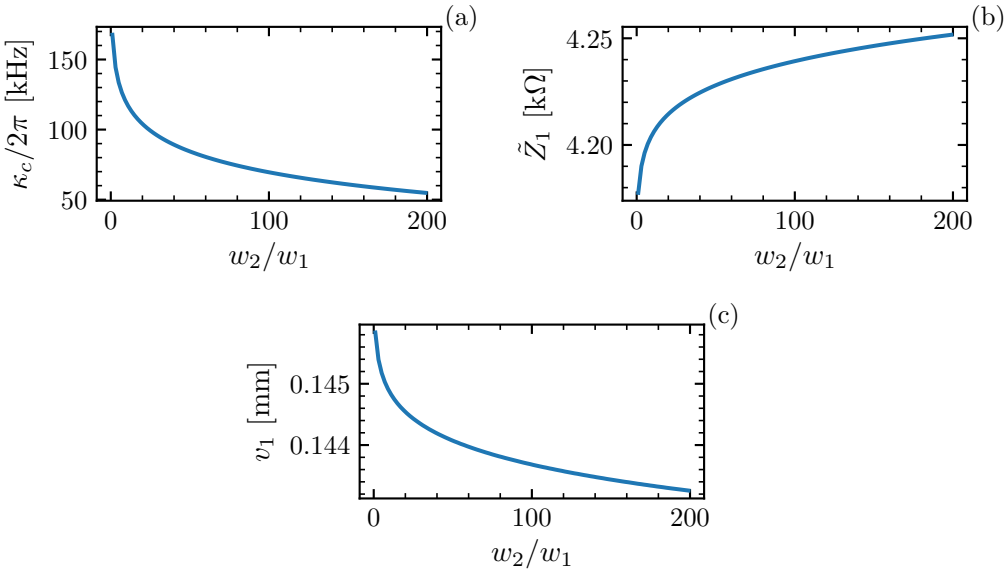

Figure 1.12: DBR design II: (a) Coupling rate, (b) characteristic mode impedance and (c) mode volume for the second resonant mode as function of the width mismatch between the layers. All the parameters are evaluated at the resonant frequency of the mode that remains constant and equal to $2\pi \times 6\,\mathrm{GHz}$

What the two modes have in common is that their properties depend much less on the geometrical width mismatch. The reason for this is that, in this design, the impedance mismatch is mainly coming from the difference of inductance between the layers, while the difference in capacitance contributes only in a small part. It is interesting to notice that even for very high mismatches, the $n = 0$ mode has a characteristic impedance higher than $500\,\Omega$. Regarding the $n = 1$ mode, the coupling rate κ_c reaches a minimum of $2\pi \times 50\,\mathrm{kHz}$ for high width ratio while the effective mode impedance is $4.25\,\mathrm{k}\Omega$, very close to the $\lambda/4$ cavity case of $4.3\,\mathrm{k}\Omega$.

For this geometry, we are also interested in studying how the properties of the circuit change if l_2 is different from $\lambda_2/4$. We do so by studying the first two modes as a function of the length l_2, and with a width mismatch $w_2/w_1 = 20$. We plot the results in figure 1.13 and 1.14. Both the resonant frequency and the impedance of the $n = 0$ mode decrease as l_2 increases, while the change in the coupling rate κ_c is almost negligible. For the $n = 1$ mode, as $\lambda/8 < l_b < 3\lambda/8$ the resonance frequency is close to the expected value of $2\pi \times 6\,\mathrm{GHz}$ and the mode impedance is 5 % smaller than the value of $4.3\,\mathrm{k}\Omega$. The coupling rate is minimum, as expected, when $l_2 = \lambda_2/4$ and gets bigger as l_s moves away from that value. It is interesting to notice that we can reach low κ_c even when l_2 is far from the Bragg condition. At the same time the impedance of the mode changes only by 20 % when $l_2 = \lambda_2/40$. This can be useful if one wishes to reduce κ_c without decreasing too much the mode impedance. It is also important to underline is that when changing l_2, the spectrum of the low impedance modes also changes.

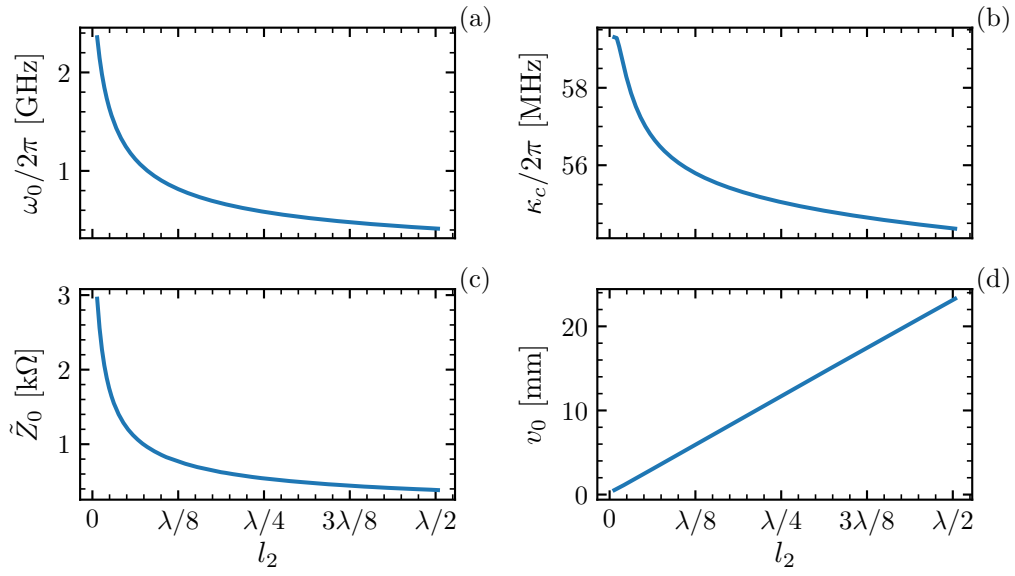

Figure 1.13: DBR design II: (a) Resonance frequency, (b) coupling rate, (c) characteristic mode impedance and (d) mode volume for the first resonant mode as function of the length of the second layer.

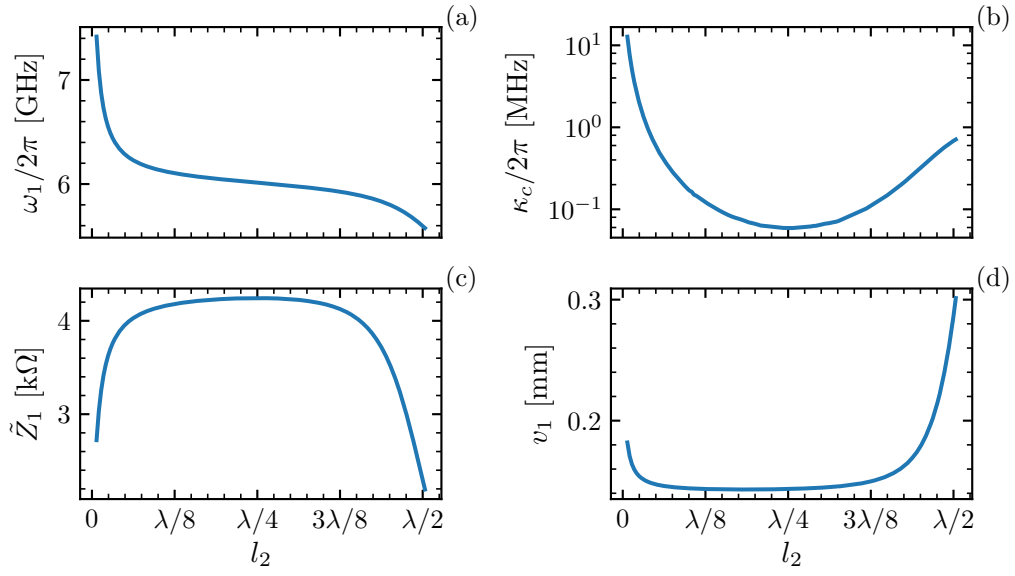

Figure 1.14: DBR design II: (a) Resonance frequency, (b) coupling rate, (c) characteristic mode impedance and (d) mode volume for the second resonant mode as function of the length of the second layer.

1.3 Sonnet simulations

The results obtained up to this point rely on the fact that the resonator is a 1D transmission line where the transversal component of voltage and current are negligible. This may not be the case when the design involves lines of different geometrical widths such as in the DBR. Using Sonnet, a high frequency electromagnetic simulation software, we compute the properties of the circuits previously discussed and we compare them to the ones obtained with the transfer matrix method. We show that the 1D model correctly predicts the mode resonance frequencies and impedance but underestimate the coupling rates κ_c.

To extract the parameters of the modes from Sonnet, we follow a similar procedure to the one described for the 1D model. We place a co-calibrated port at the position of the junction (at the end of the cavity) and a standard port on the 50 Ω line (fig. 1.15a). Sonnet allow us to directly get the admittance matrix of the circuit $y(\omega)$ from which we compute the admittance seen by the junction $Y(\omega)$ by eliminating the second port with equation 1.30. The resonant frequency of the modes is again given by the solution of $\mathrm{Im}[Y(\omega)] = 0$ while their impedance can be computed with eq. 1.23. Because the Sonnet simulation is not 1D, our definition of mode "volume" (eq. 1.17) does not hold anymore and we compute the coupling Λ_n using 1.15. The coupling rate κ_c is obtained from the reflection spectrum S_{11} computed placing a single port on the 50 Ω line (fig. 1.15b).

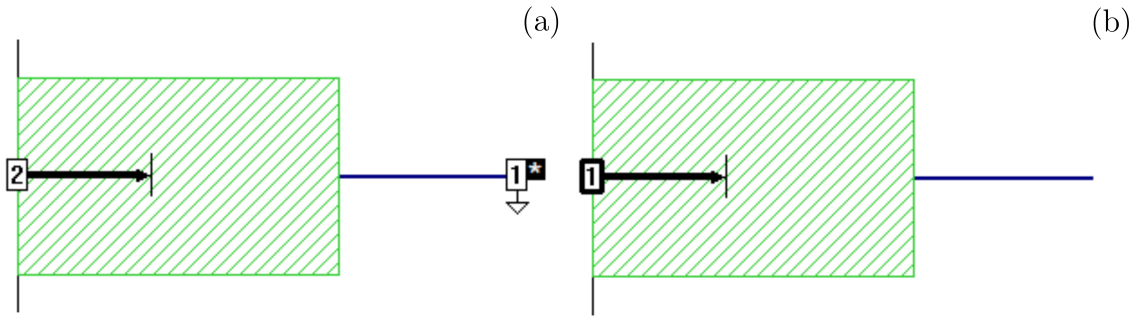

Figure 1.15: Image of the Sonnet board used for simulating the quarter wavelength cavity discussed in 1.3.1. (a) The impedance seen by the junction is simulated by placing a first co-calibrated port at the position of the junction (end of the high impedance line in dark blue) and a second standard port on the 50 Ω line (in green). (b) To simulate the spectrum of the cavity, and calculate the coupling rate, we use only a single standard port on the 50 Ω line.

1.3.1 Quarter wavelength cavity

A high impedance quarter wavelength cavity has typically a geometrical width of few µm while a 50 Ω transmission line in microstrip geometry, when realized on silicon substrate, has a width around 200 µm. Since we are interested in studying the effect of this width mismatch, we consider a circuit composed by a 1 µm wide cavity, with kinetic inductance per square equal to 1 nH/□, which is directly coupled to a 50 Ω line 220 µm wide. In order

to compare the results of the transfer matrix method and the one obtained from Sonnet we use, for the cavity, the impedance Z_1 and the phase velocity v_{p_1} derived directly from the latter. We get $Z_1 = 4.7\,\mathrm{k\Omega}$ and $v_{p_1} = 4.96 \times 10^6\,\mathrm{m\,s^{-1}}$. Using the results obtained in 1.2 we compute the admittance seen by the junction (figure 1.16a) and the spectrum of the cavity (figure 1.16b). We get, for a 200 µm long cavity, a first mode resonance frequency $\omega_0 = 2\pi \times 6.2\,\mathrm{GHz}$, impedance $\tilde{Z}_0 = 5.9\,\mathrm{k\Omega}$ and a coupling rate $\kappa_c = 2\pi \times 85\,\mathrm{MHz}$. The results obtained simulating the same circuit on Sonnet agree within 5 % with the one of the 1D model except for the coupling rate κ_c. This discrepancy is due to the width mismatch that causes the reflection coefficient at the interface between the two lines to increase. This effect is even bigger for a DBR resonator as shown in the next section.

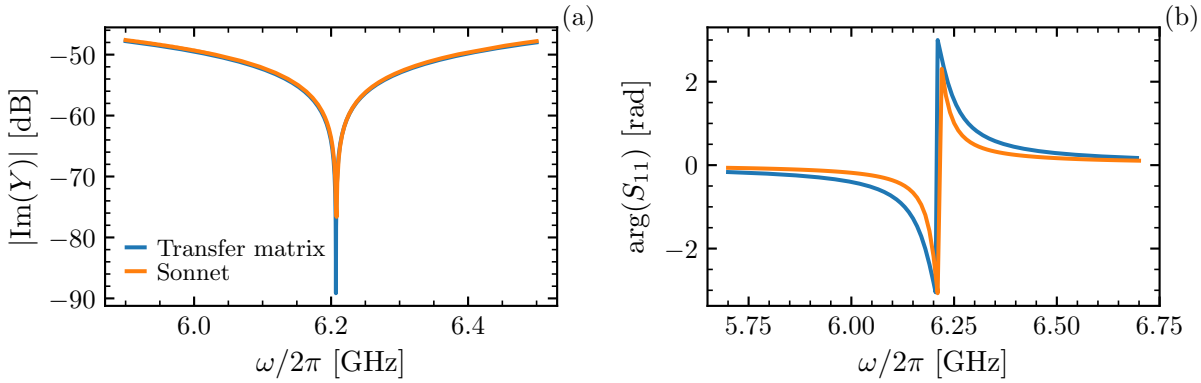

Figure 1.16: (a) Admittance seen by the junction and (b) spectrum of the cavity computed simulating the circuit with the transfer matrix method and Sonnet.

	ω_0	$\tilde{Z}_0$	κ_c
Transfer matrix	$2\pi \times 6.2\,\mathrm{GHz}$	$5.9\,\mathrm{k\Omega}$	$2\pi \times 85\,\mathrm{MHz}$
Sonnet	$2\pi \times 6.2\,\mathrm{GHz}$	$5.7\,\mathrm{k\Omega}$	$2\pi \times 40\,\mathrm{MHz}$

1.3.2 DBR simulations

Here we focus on the Sonnet simulation of the two DBR designs described in section 1.2.2. Again we compare the results with the one of the 1D model in order to underline the main differences between the two.

DBR design I

For the simulation of the first design we fix again $L_K = 1\,\mathrm{nH/\square}$ and we choose $w_1 = w_3 = 1\,\mu\mathrm{m}$ and $w_2 = 20\,\mu\mathrm{m}$. According to Sonnet $Z_1 = 4.7\,\mathrm{k\Omega}$ and $v_{p_1} = 4.96 \times 10^6\,\mathrm{m\,s^{-1}}$, while $Z_2 = 755\,\Omega$ and $v_{p_2} = 1.51 \times 10^7\,\mathrm{m\,s^{-1}}$. l_1 and l_3 are chosen to be equal to 200 µm with an expected resonant frequency for the first cavity mode of $2\pi \times 6.2\,\mathrm{GHz}$. For the second layer the length l_2 is chosen by maximizing the coupling quality factor $Q_c = \omega_1/\kappa_c$. We find that when $l_2 = 580\,\mu\mathrm{m}$, Q_c is maximum and equal to 2.7×10^4. This length does not perfectly match the condition $l_2 = \lambda_2/4$ meaning that the reflection coefficient at each interface is not

purely real and that a phase shift at each reflection might be present. In the next table we report the comparison of the properties of the $n = 1$ mode obtained with the two different simulations.

	ω_1	$\tilde{Z}_1$	κ_c
Transfer matrix	$2\pi \times 6.2\,\mathrm{GHz}$	$5\,\mathrm{k\Omega}$	$2\pi \times 2\,\mathrm{MHz}$
Sonnet	$2\pi \times 6\,\mathrm{GHz}$	$4.9\,\mathrm{k\Omega}$	$2\pi \times 0.3\,\mathrm{MHz}$

DBR design II

The same kind of analysis can be performed for the second design. We keep the geometry the same with the exception of the second layer that is replaced with a low impedance material. From Sonnet we get $Z_2 = 107\,\Omega$ and $v_{p_2} = 1.12 \times 10^8\,\mathrm{m\,s^{-1}}$. The highest Q_c is reached when $l_2 = 4.7\,\mathrm{mm}$ and it is equal to 1.6×10^6. From the simulations of the design we get for the first cavity mode:

	ω_0	$\tilde{Z}_0$	κ_c
Transfer matrix	$2\pi \times 6.2\,\mathrm{GHz}$	$5.8\,\mathrm{k\Omega}$	$2\pi \times 50\,\mathrm{kHz}$
Sonnet	$2\pi \times 6\,\mathrm{GHz}$	$5.6\,\mathrm{k\Omega}$	$2\pi \times 3\,\mathrm{kHz}$

Once again we get that, while the resonant frequency and impedance of the $n = 1$ mode obtained from the two simulations, are quite similar, the coupling rate derived from the transfer matrix method is much higher than the Sonnet's one. In designing the final sample we used the 1D model to get a general understanding of the properties of the circuits while we adjusted the design and fine tuned all the parameters using Sonnet.

1.4 Design final sample

In this final section, we discuss the geometry we chose for the sample and we analyze its electromagnetic properties. The main requirement for the design was that the fundamental cavity mode ($n = 1$) had the highest Λ_1 possible and that its resonant frequency was between $4\,\mathrm{GHz}$ and $8\,\mathrm{GHz}$, which is the bandwidth of the setup we used for the measurement. At the same time, we wanted a coupling quality factor close to 1×10^4. The design was also influenced by the steps of fabrication processes regarding in particular the realization of a dissipationless contact between the cavity and the junction. A detailed description of the fabrication process can be found in chapter 2, here we just want to mention the main steps and how they affected the geometry of the circuit.

After having tested two different high impedance superconductors (NbSi and granular Aluminum), we decided to realize the cavity using grAl since it has a lower intrinsic loss rate and it can be fabricated using the lift-off technique, easier to implement in the facilities of our laboratory. To have a sufficiently high impedance, we deposit $10\,\mathrm{nm}$ of metal. If, on one hand, this choice allow us to reach higher resistivity and therefore higher kinetic inductance, on the other, it makes it harder to realize a dissipationless contact between the cavity and the junction. The junction, that we place at the end of the cavity to maximize the coupling, is fabricated separately from the rest of the circuit. We connect it to the cavity using an Ar gun, to remove the native oxide from the surface of the metals, followed by a deposition of a layer of Al, that put in contact the two circuits. The oxide etching process can be challenging

if performed on such a thin film and therefore we decide to realize a thick Al pad placed at the end of the cavity and deposited before the grAl is exposed to atmospheric pressure. To prevent this Al layer from completely covering the high impedance metal, we deposit it with angle evaporation and we exploit the high aspect ratio between the thickness of the resist mask and the width of the wire to be sure that only the regions whose total width exceed 1.3 µm would have been covered.

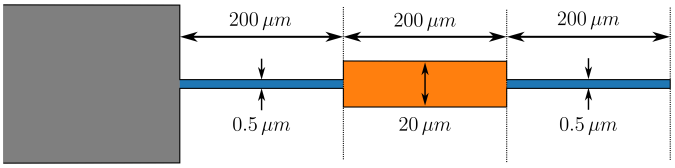

Figure 1.17: Geometry of the final sample. The cavity and the first DBR layer have a width of 0.5 µm and a length of 200 µm (chosen to have ω_1 close to $2\pi \times 6$ GHz). The second layer is realized with a low impedance material and has $w_2 = 20$ µm and $l_2 = 200$ µm. The length l_2 does not fulfill the Bragg resonance condition and this has been chosen in order to reduce the coupling rate of the $n = 1$ mode. At the end of the cavity a small low impedance pad (not reported in the drawing) is present.

To summarize, the main requirements for the design are that the cavity and the first DBR layer have a width smaller than 1.3 µm and that the second layer is realized in a low impedance material, since its width is bigger than 1.3 µm. As we have seen in section 1.3.2, a DBR realized with a low impedance superconductor can easily reach coupling quality factor of 1×10^6 which are far above the desired value for the sample. To decrease its value, we reduced the length of the second layer until reaching the wanted coupling rate. A scheme with the final design and all its dimension is shown in figure 1.17. In the drawing we do not show the 2.5 µm × 2.5 µm Al pad placed at the end of the cavity to which we connect the junction. Its main effect is to increase the capacitance to the ground at the end of the cavity and we incorporate it in the capacitance of the junction. The expected kinetic inductance of the grAl is 650 pH/□ which gives, according to Sonnet simulations, an impedance and a phase velocity for the first and last layer equal to 5.8 kΩ and 4.7×10^6 m s^{-1}. The second layer instead has an impedance of 105 Ω and a phase velocity of 110×10^6 m s^{-1}.

1.4.1 Spatial dependence of the modes

Using the transfer matrix method we compute the resonant frequency, the mode volume and the spatial dependence of the first six modes (figure 1.18). The results are reported in table 1.2. The $n = 0$ mode is strongly coupled and it spreads across the whole DBR structure. For the higher order modes we have an odd-even effect with the odd modes being strongly coupled, because mainly confined in the cavity layer, and the even ones being weakly coupled, due to their confinement in the first layer, far from the junction.

	$\omega_n/2\pi$ [GHz]	v_n [mm]	$\Lambda_{n,\mathrm{cp}}$
n = 0	1.87	1.2	1.55
n = 1	6.69	0.23	1.87
n = 2	11.68	12.14	0.19
n = 3	17.96	0.20	1.22
n = 4	22.65	39.3	0.08
n = 5	29.60	0.20	0.95

Table 1.2: Properties of the first six modes of the final sample, obtained with the transfer matrix method.

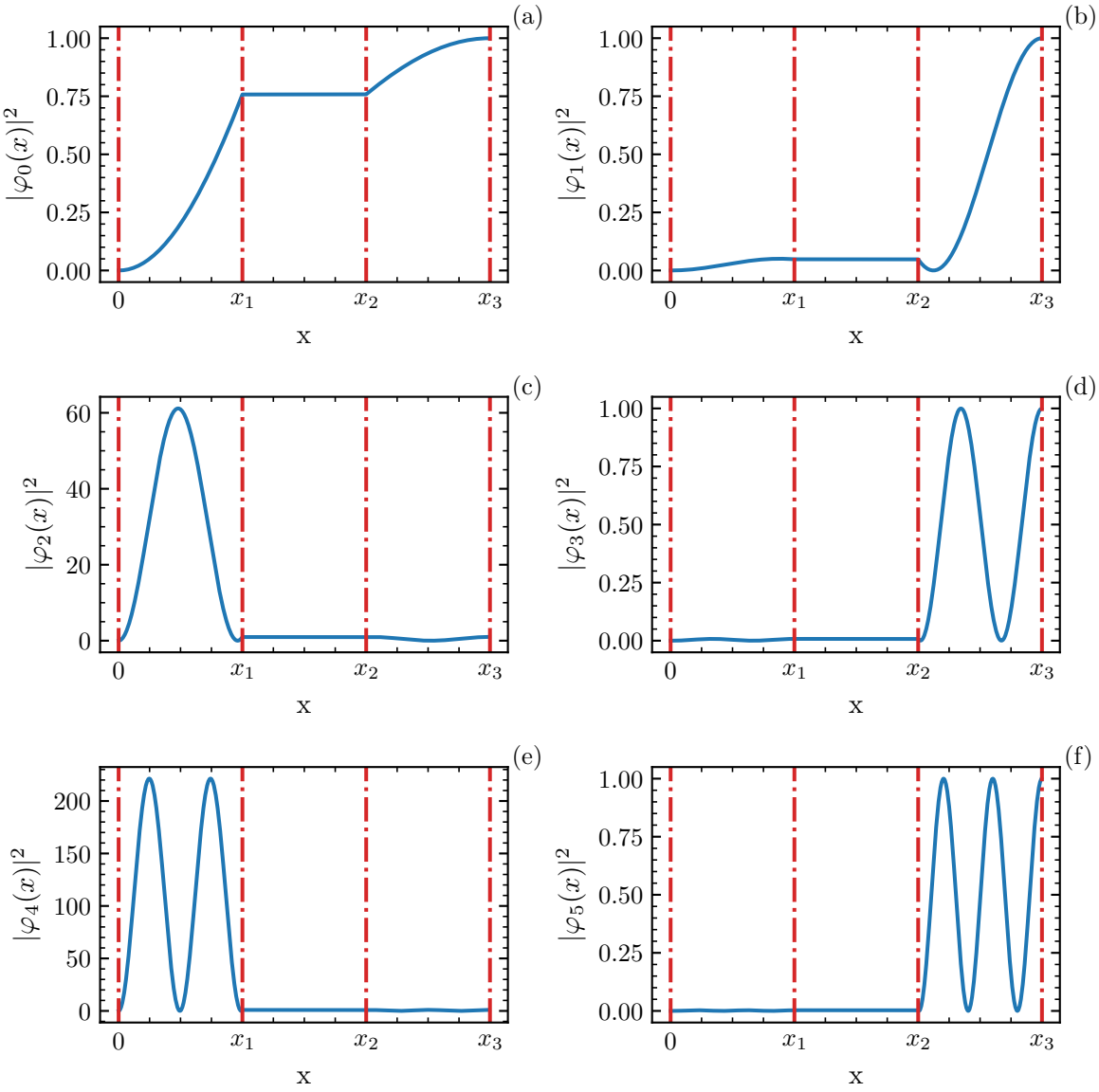

Figure 1.18: Spatial dependence $\varphi_n(x)$ of the first six modes of the final sample.

1.4.2 Sonnet simulation of the sample

From the Sonnet simulation of the sample we derive the resonant frequency, the coupling rate and the mode impedance of the first six modes (table 1.3).

	$\omega_n/2\pi$ [GHz]	κ_c [MHz]	$\tilde{Z}_n$ [kΩ]	$\Lambda_{n,\mathrm{cp}}$
n = 0	1.85	25	3.67	1.35
n = 1	6.52	0.25	5.72	1.67
n = 2	11.33	11.5	0.02	0.1
n = 3	17.1	0.1	2.14	1.02
n = 4	21.46	8	0.002	0.03
n = 5	27.7	0.05	1.27	0.78

Table 1.3: Properties of the first six modes of the final sample, obtained using Sonnet.

1.4.3 Effect of the junction on the modes

So far we have assumed that the junction acts as an open circuit, meaning that the reflection coefficient between the cavity and the junction is equal to one. In this section we discuss the validity of this approximation and we consider how the modes of the cavity may be affected by the presence of the junction. We do so by replacing the junction with a grounded capacitance connected at the end of the DBR and we study how the properties of the modes change when C_J is changed. We take into account the effect of this extra circuit element by adding its admittance to the admittance seen by the junction. The total admittance of the circuit is therefore given by $Y(\omega) + Y_J(\omega)$, with $Y(\omega)$ admittance of the cavity with DBR extracted from Sonnet simulations and $Y_J(\omega)$ admittance of the junction given by:

$$Y_J(\omega) = i\omega C_J. \tag{1.34}$$

C_J can be estimated to be equal to $C_J = \epsilon_0 \epsilon_r A/d$ with ϵ_r relative permittivity of the junction insulator, d thickness of the insulator and A surface area of the junction. Typical values of thickness and permittivity for the insulator are $d = 1\,\mathrm{nm}$ and $\epsilon_r = 9.5$, which give a capacitance C_J around $85\,\mathrm{fF}\,\mu\mathrm{m}^{-2}$.

To get a simplified analytical expression for the variation of resonant frequency and impedance of the modes we model the cavity as a series of lumped LC resonator, each of them associated to a different mode of the circuit. Their inductance L_{r_n} and capacitance C_{r_n} can be extracted from the admittance $Y(\omega)$ when $\omega \approx \omega_n$ and are reported in table 1.4. In this way, we can write the variation of ω_n and $\tilde{Z}_n$, at the second order in C_J, as:

$$\frac{\delta\omega_n}{\omega_n} = \frac{\delta\tilde{Z}_n}{\tilde{Z}_n} = -\frac{1}{2}\frac{C_J}{C_{r_n}} + \frac{3}{8}\left(\frac{C_J}{C_{r_n}}\right)^2. \tag{1.35}$$

In figure 1.19 we report the relative variation of resonant frequency and effective impedance as function of the capacitance C_J, for the first three modes.

As C_J increases, the resonant frequency and the impedance of the strongly coupled modes decreases, while the ones of the weakly coupled modes remain unchanged. It is interesting to notice that, because all the high impedance (odd) modes have a similar lumped capacitance

	L_{r_n} [nH]	C_{r_n} [fF]
n = 0	322.8	23.7
n = 1	139.7	4.2
n = 2	0.26	752
n = 3	20	4.3
n = 4	0.014	3932
n = 5	7.35	4.5

Table 1.4: Values of inductance and capacitance of the lumped element resonator associated to each cavity mode.

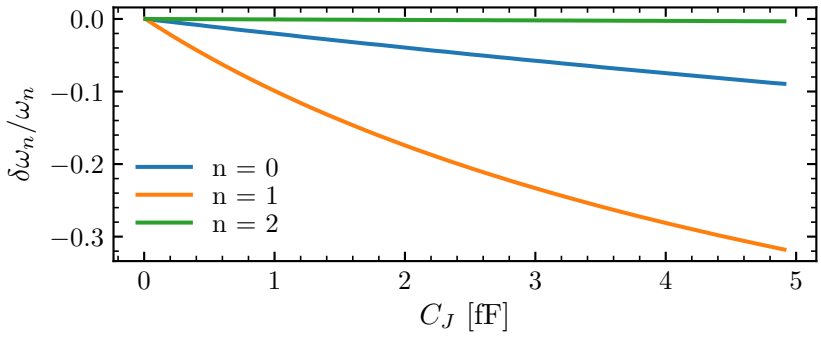

Figure 1.19: Relative variation of resonant frequency $\delta\omega_n/\omega_n$ (and mode impedance $\delta\tilde{Z}_n/\tilde{Z}_n$) of the first three modes, as function of C_J. As the capacitance of the junction increases ω_n and $\tilde{Z}_n$ decrease.

C_{r_n}, the relative variation of ω_n and $\tilde{Z}_n$ is the same. In order to keep the mode impedance as high as possible a junction with small capacitance is needed. Experimentally this condition can be satisfied by reducing the surface area of the junction. When this happens, we can neglect the effect of the junction on the frequency and on the impedance of the modes and use the open circuit approximation. Since typical values of junction size are between 100 nm × 100 nm and 200 nm × 200 nm we expect C_J to be around 2 fF. When this happen the frequency and the characteristic impedance of the odd modes are reduced of approximately 15 % as shown in table 1.5 where we report the resonant frequencies and the mode impedance calculated with $C_J = 2$ fF.

	$\omega_n/2\pi$ [GHz]	$\tilde{Z}_n$ [kΩ]	$\Lambda_{n,\mathrm{cp}}$
n = 0	1.73	3.54	1.31
n = 1	5.27	4.72	1.51
n = 2	11.33	0.02	0.1
n = 3	14.03	1.77	0.92
n = 4	21.46	0.002	0.03
n = 5	23.68	1.06	0.72

Table 1.5: Properties of the first six modes of the sample assuming a junction capacitance of 2 fF.

Conclusions

We have shown that in a distributed cavity the coupling Λ_n depends on the position of the junction and on the cavity's mode volume that quantifies the confinement of the mode. We showed how the mode volume is directly linked to the effective mode impedance, that can be calculated using the admittance seen by the junction, and how it can be used to design a cavity with the highest coupling possible.

Using a transfer matrix 1D simulation we have analyzed the properties of different DBR designs and we have seen that it is possible to reduce the coupling rate κ_c of several orders of magnitude without reducing Λ by more than a few per cent. we compared the results obtained with the transfer matrix model to simulations realized using Sonnet. While the 1D model manages to give good predictions regarding the frequency and the impedance of the modes, it overestimates the coupling rate. This is due to the geometrical width mismatch, between the several lines that composes the circuit. The reflection coefficient at each interface depends not only on the mismatch of impedance but also on the width mismatch.

In conclusion we discussed the design of the DBR to which we couple the junction and the expected properties of its modes. We have shown that the two most coupled modes are the $n = 0$ mode, with $\Lambda_{0,\mathrm{cp}} = 1.35$, and the $n = 1$ mode, with $\Lambda_{1,\mathrm{cp}} = 1.67$. We also discussed the effect of the junction on the cavity modes and we have shown that junction of small size reduce the impedance of the strongly coupled modes of approximately 15 %.

Chapter 2

Experimental Methods

Contents

For the realization of high impedance cavities we tested two superconductors with high kinetic inductance: Niobium-silicon (NbSi) and granular Aluminum (grAl). The first is obtained through a coevaporation of Nb and Si while the latter is realized by the deposition of Al in a controlled oxygen atmosphere. In both cases it is possible to control the superconducting critical temperature T_c and the normal resistivity ρ_N by changing the thickness of the metallic film or the amount of silicon or oxygen in the material. For both materials, we tested different cavities with different geometries and in this chapter we present some of the results obtained measuring them.

In the first section we focus on two samples realized using NbSi: a $\lambda/2$ cavity connected to two $50\,\Omega$ lines and a $\lambda/4$ cavity coupled to a DBR. For each design we first introduce the fabrication techniques used to realize the samples and we later discuss the microwave characterization of the resonators. In the second section we present the grAl cavity to which we couple the Josephson junction and whose design we introduced in section 1.4. Once again we start from the fabrication process, including the steps involving the connection between the cavity and the junction, and we then show the results obtained performing spectroscopy measurement on the cavity alone. We conclude the chapter discussing both the microwave and DC setup that we use for the measurement of cavity microwave field.

2.1 NbSi cavities: fabrication and characterization

NbSi is a high impedance superconductor obtained by the codeposition of niobium and silicon [15, 38]. Like for all superconductors, its electrodynamics properties, in the microwave regime, are described by Mattis-Bardeen theory (appendix A) and depend on the superconducting critical temperature T_c and the normal resistivity ρ_N. Both these parameters can be tuned by choosing the niobium concentration, the thickness of the film and its annealing temperature.

In order to verify that we are able to predict and understand the behavior of high impedance cavities, we designed and fabricated a low quality factor resonator and we measured its field as function of temperature and DC current. We also test a design of a DBR realized entirely using NbSi and we verify that its measured properties are compatible with the ones expected from simulations.

2.1.1 $\lambda/2$ cavity

The sample consists in a cavity of length l and impedance Z_1 embedded between two $Z_0 = 50\,\Omega$ transmission lines. A schematic representation of the design is shown in figure 2.1. Because of the boundary conditions, the modes of this cavity have a frequency $\omega_n = (n+1)v_p\pi/l$, meaning that the length of the cavity is $l = (n+1)\lambda/2$ with λ the wavelength at resonance. To have the fundamental cavity mode $\omega_0 \simeq 2\pi \times 6\,\mathrm{GHz}$ and because the expected phase velocity v_p is close to $4.7 \times 10^6\,\mathrm{m\,s^{-1}}$, the length of the cavity is fixed to $400\,\mu\mathrm{m}$. The coupling rate to the measurement line depends on the impedance mismatch between the lines ($\kappa_c = 4\omega_0 Z_0/[\pi(Z_1+Z_0)]$) and, as in the case of the DBR, is enhanced by the width mismatch.

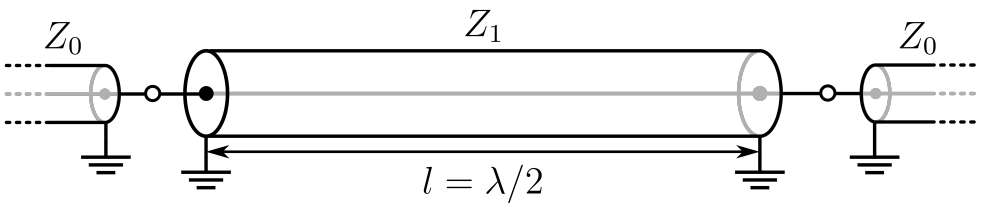

Figure 2.1: Schematic representation of the circuit. A high impedance line is embedded between two $Z_0 = 50\,\Omega$ transmission lines. The total length of the cavity sets the resonance condition with l being equal to $\lambda/2$ for the fundamental mode.

Fabrication

The NbSi samples we studied have a niobium concentration of 25 %, a film thickness of 50 Å and were annealed at 140 °C with an expected critical temperature $T_c \approx 1\,\mathrm{K}$ and resistivity $\rho_N \approx 6\,\mu\Omega\,\mathrm{m}$.

All the circuits are realized on a 300 µm thick, thermally oxided, silicon substrate. First, the wafers are cleaned in hot (65 °C) acetone and in an IPA sonic bath followed by an oxygen plasma. The metal deposition is done through electron beam evaporation in different evaporators using two complementary mechanical masks: the first one allow us to deposit metal only at the edge of the wafer, while the second one only in the central part, with an overlapping between the two regions of about 500 µm on both sides. In the first evaporation, we deposit 50 nm of niobium necessary for the realization of the 50 Ω lines. The niobium is covered by 5 nm of iridium in order to prevent oxidation between the different steps of the fabrication process. The distance between the planes on the two sides of the wafer is 500 µm. In the second evaporation, we deposit 5 nm of NbSi through a coevaporation of Nb and Si at a rate, controlled by piezo-electric quartz, of $1\,\text{Å}\,\mathrm{s}^{-1}$. The NbSi is covered by 10 nm of silicon oxide to again prevent oxidation. The use of mechanical masks grants a smooth height profile which in turn ensures a good contact between the metals. All evaporations are realized in ultra high vacuum chamber (10^{-8} mbar) and the thickness and composition of the deposited metals are checked after by Rutherford backscattering spectroscopy which confirms the values expected.

The 50 Ω lines and the resonator structures are patterned using a 30 keV electronic microscope. For the low impedance parts we realize a 200 µm wide stripline separated by 100 µm from the ground plane in order to get a transmission line with a characteristic impedance Z_0 close to 50 Ω. We spin coat the sample with approximately 800 nm of PMMA 950 A3 resist and expose the part covering the metallic surface to etch, with a dose of $320\,\mu\mathrm{C}\,\mathrm{cm}^{-2}$. We develop the sample 40 seconds in a solution of MIBK and IPA. The etching is done using a plasma made by a mixture of CF4 (20 sccm) and Argon (10 sccm), with a pressure of 50 µbar and an RF power for the plasma of 50 W. The end of the process, that lasts approximately 5 minutes, is determined by an optical setup. With a second lithography we pattern the resonator structure that is designed to be a 400 µm long and 2 µm wide wire, that at the end of the process resulted to be narrower giving us a final width of 1.85 µm. The resist used for this lithography is again PMMA A3 but with a thinner thickness (400 nm) while the RIE process is the same (except for the total time that is around 1 minute). Because

the total length of the NbSi region, fixed by the mechanical mask, is bigger than the desired resonator length, at the end of each side of the wire a 200 µm wide NbSi pad is present. The asymmetry in length of these pads is due to a misalignment during the lithography process. All the sizes are confirmed with an SEM observation and are reported in fig. 2.2. At the end of the process a 30 nm Nb back plane is deposited.

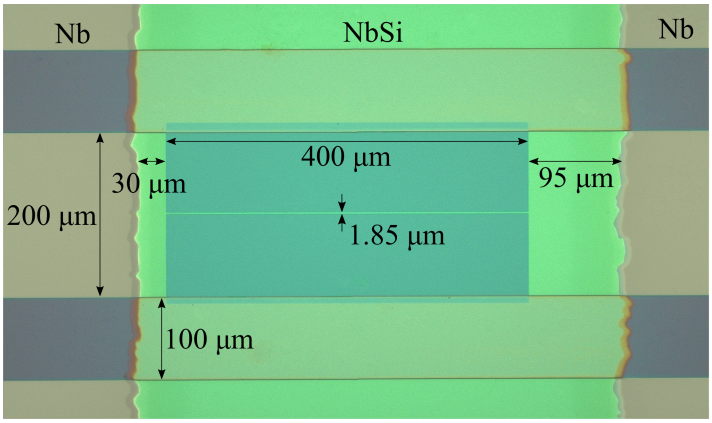

Figure 2.2: Optical image of the sample. The resonator is made by a 400 µm long and 1.85 µm wide wire that is directly coupled to Nb line. At each extremity of the wire a NbSi pad is present.

Characterization of temperature dependence

The resistance of the sample at $T \sim 4T_c \simeq 4\,\mathrm{K}$ is 249 kΩ which gives us a resistivity of 5.74 µΩ m. The critical temperature is 1 K and hence the superconducting gap at zero temperature is around 150 µeV. From these parameters we estimate $\lambda_L = \sqrt{\hbar\rho/(\mu_0\pi\Delta_0)} \approx 3\,\mu\mathrm{m}$. Since λ_L is much larger than the thickness of the superconducting wire, the thin film approximation is valid and we can use equations A.6 and A.7 for the calculation of the square resistance and of the kinetic inductance. At a temperature of 10 mK and for frequencies of the order of 6 GHz we expect a completely negligible resistance per square and kinetic inductance $L_k = 1.58\,\mathrm{nH/\square}$ which, given the geometry of the sample, corresponds to an inductance per unit length of $8.5 \times 10^{-4}\,\mathrm{H\,m^{-1}}$. Using the numerical simulation software Sonnet we estimate the geometrical capacitance and inductance, obtaining the following values: $C_l = 5.2 \times 10^{-11}\,\mathrm{F\,m^{-1}}$, $L_e = 1.3 \times 10^{-6}\,\mathrm{H\,m^{-1}}$. As expected, the electromagnetic inductance is negligible compared to the kinetic one and hence $L_l = L_k + L_e \approx L_k$. We therefore predict a resonator with characteristic impedance $Z_1 = 4.05\,\mathrm{k\Omega}$ and phase velocity $v_p = 4.75 \times 10^6\,\mathrm{m\,s^{-1}}$. By simulating the whole structure on Sonnet we obtain an expected first mode resonant frequency $\omega_0 \approx 2\pi \times 5.93\,\mathrm{GHz}$ and an expected coupling rate $\kappa_c \approx 2\pi \times 50\,\mathrm{MHz}$.

We measured the spectrum obtained at 10 mK, with an injected power of -135 dBm. The transmission at resonance is close to −2 dB and since its value saturates when the temperature goes down we assume that the resonator is over-coupled at low T and that $\kappa_c > \kappa_i$ with κ_i quantifying the intrinsic loss rate of the cavity. We used this amplitude to normalize all the

other spectra acquired at higher temperature as shown in fig. 2.3a. We fit the transmission S_{21} using the function:

$$S_{21} = \frac{-\kappa_c}{\kappa + 2i\delta}, \tag{2.1}$$

with $\kappa = \kappa_i + \kappa_c$ total linewidth of the cavity and $\delta = \omega - \omega_0$ frequency detuning. We extract, at $T = 10\,\text{mK}$, $\omega_0 = 2\pi \times 6.07\,\text{GHz}$, $\kappa_i = 2\pi \times 6\,\text{MHz}$ and $\kappa_c = 2\pi \times 30\,\text{MHz}$.

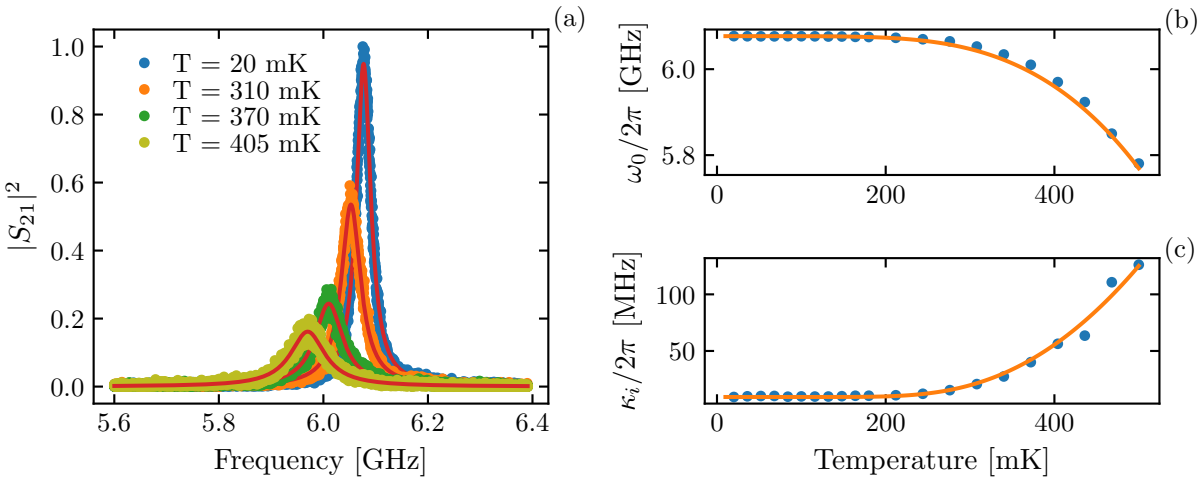

Figure 2.3: (a) Normalized cavity's transmission spectra $|S_{21}|^2$ measured at different temperatures. Variation of (b) resonant frequency and (c) intrinsic losses, with their predicted Mattis-Bardeen behavior, as function of the temperature.

Figure 2.3 shows also the variation of resonant frequency ω_0 and intrinsic losses κ_i as a function of temperature. As expected,the resonance frequency decreases as the temperature increases as predicted by Mattis-Bardeen theory. This variation can be derived from equation A.7 and it is equal to:

$$\omega_0(T) = -\frac{1}{2}\frac{\sigma_2(T) - \sigma_2(T_0)}{\sigma_2(T)}\omega_0(T_0) + \omega_0(T_0). \tag{2.2}$$

At the same time, the linewidth of the cavity increases because of the change in σ_1. The dependence of κ_i on the temperature can be written as:

$$\kappa_i(T) = \omega_0(T)\frac{\sigma_1(T)}{\sigma_2(T)} + \kappa_i(T_0), \tag{2.3}$$

Here, $\omega_0(T_0)$ and $\kappa_i(T_0)$ refer to the value of ω_0 and κ_i measured at $T_0 = 10\,\text{mK}$. In both cases the expected Mattis-Bardeen theory behavior matches well the experimental data.

Characterization of DC current dependence

We now look at how the properties of the cavity change as a function of the DC bias current. Again, as before, we normalize the amplitude of the transmitted signal in absence of current to 1 and we record its variation, together with the variation of the resonance frequency

and quality factor (fig. 2.4). From the variation of ω_0, using the gap dependence on the current (appendix A), we are able to extract the theoretical value of the critical current of the resonator. For every current we compute the reduced superconducting gap Δ, by solving equations A.8 and A.9, from which we calculate the variation of the imaginary part of the conductivity σ_2 (eq. A.2). This allows us, in the end, to fit the variation of ω_0 (eq. 2.2), as shown in fig. 2.4b. We use as only fit parameter the critical current I_c present in equation A.9 which in the end resulted to be equal to: $I_c = 6.15\,\mu$A. We can compare this result with the measured switching current which is $I_s = (3.3 \pm 0.2)\,\mu$A. This measurement and its uncertainty are the mean value and the standard deviation obtained from measuring 100 switching events. This value is two times smaller than the one obtained from the fit of the variation of ω_0 and this is probably due to the possible presence of resistive defects in the resonator that dissipate and cause a switching before the critical current is reached. This hypothesis is supported by the variation of quality factor shown in fig. 2.4c. Q remains almost constant up to the point where the DC current reaches the value of the switching current I_s. At this point the intrinsic loss of the cavity explodes and the quality factor drops to zero. This behavior is not compatible with the theory described in A which predicts a smooth increment of resistance per square of the superconductor and therefore a smooth drop of quality factor.

It is also worth noticing that the model used to fit these data is derived at zero temperature and this can also cause a small deviation between the measured and expected values. In any case, the DC current at which the properties of the cavity start to change is order of magnitude higher than the junction critical current and therefore we can neglect its effect on the cavity when biasing the junction.

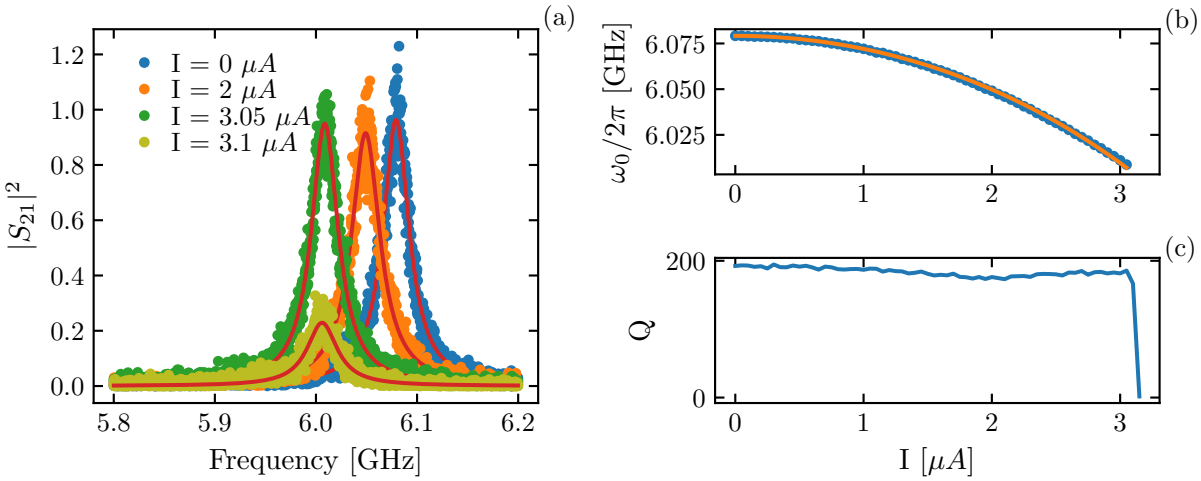

Figure 2.4: (a) Normalized spectra for different bias current. (b) Variation of resonant frequency and (c) quality factor as function of the current. The orange curve in panel b is the fit of the variation of ω_0 performed using equation A.8.

2.1.2 $\lambda/4$ cavity with DBR

To test the DBR design discussed in chapter 1 we realized a quarter wavelength cavity coupled to a 50 Ω line through a DBR made by two NbSi lines with different characteristic impedance. In this case, as explained in 1.2.2, to achieve impedance mismatch between the layers we use lines with different geometrical width. The resonator is made of a 240 µm long and and 3 µm wide wire. The first layer of the Bragg is an exact replica of the resonator while the second one is a 590 µm long and 40 µm wide wire and its length is chosen such that it matches the Bragg resonance condition.

Fabrication

The circuit is realized using a similar process to the one previously explained (section 2.1.1), with the only difference that all the structures are defined using optical lithography. The Nb part and the NbSi part are defined separately using the same process. We spin coat the sample with 500 nm of optical resist S1805 and expose all the undesired metallic region with a dose of 80 mJ cm^{-2}. The development is done in MF319 for one minute. The excess metal is removed with RIE. Once again, at the end of the process, we deposit a Nb back plane in order to ensure a well defined ground plane. A picture of the complete sample is reported in figure 2.5.

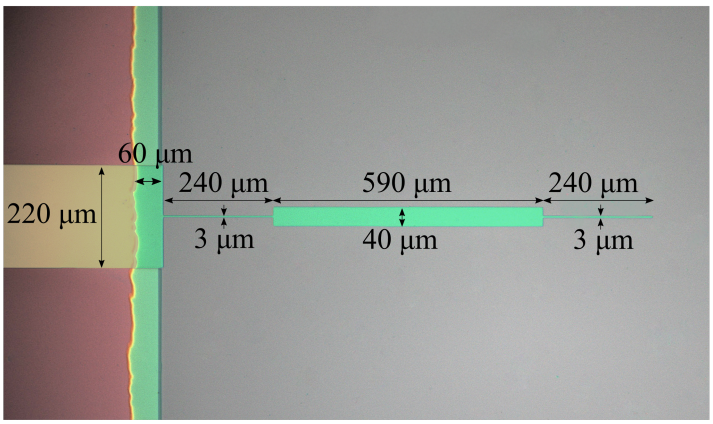

Figure 2.5: Optical image of the sample. A 3 µm wide and 240 µm long resonator is coupled to a 220 µm wide stripline through a distributed Bragg reflector made of two NbSi stacks.

Experimental characterization

For this device we do not have a direct measurement of the NbSi resistance before the superconducting transition, so for the simulations we used the same value of kinetic inductance and phase velocity derived before ($L_k = 1.58\,\mathrm{nH/\square}$ and $v_p = 4.75 \times 10^6\,\mathrm{m\,s^{-1}}$). From Sonnet, we expect a line with impedance $Z \approx 3\,\mathrm{k\Omega}$, a resonance frequency of the first cavity mode $\omega_1 = 2\pi \times 5.5\,\mathrm{GHz}$ and a coupling rate $\kappa_c = 2\pi \times 0.95\,\mathrm{MHz}$.

We start by measuring the reflection spectrum of the cavity, in the bandwidth between 4 GHz and 8 GHz, at $T = 10\,\mathrm{mK}$ with an injected microwave power of −135 dBm. The result

is shown in fig 2.6 together with the fit of the data using the following equation:

$$S_{11} = 1 - \kappa_c \frac{\kappa/2 - i\delta}{(\kappa/2)^2 + \delta^2} \tag{2.4}$$

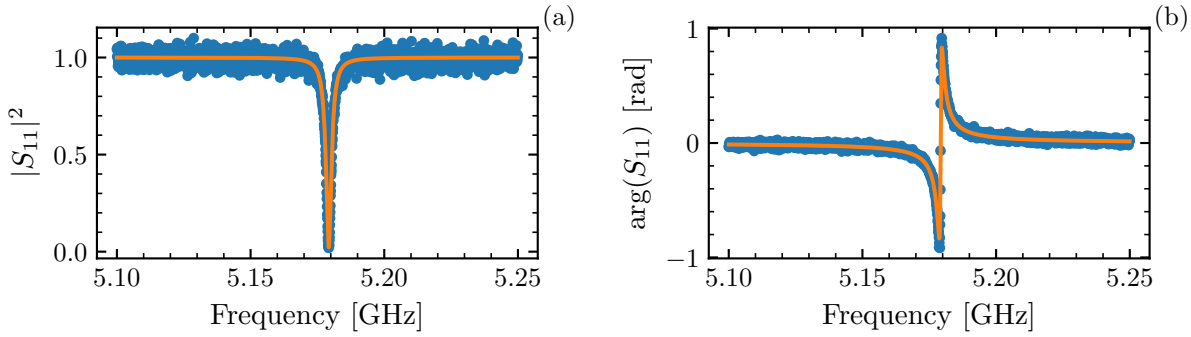

Figure 2.6: (a) Absolute value and (b) phase of the reflection spectrum of the DBR I cavity measured at $T = 10\,\text{mK}$ with $P = -135\text{dBm}$

The baseline has been normalized with a trace acquired at a temperature close to T_c that did not show any resonance. From fitting simultaneously the module and the phase of the spectrum, we extracted a resonance frequency $\omega_0 = 2\pi \times 5.18\,\text{GHz}$, an intrinsic loss rate $\kappa_i = 2\pi \times 1.38\,\text{MHz}$ and a coupling rate $\kappa_c = 2\pi \times 1.02\,\text{MHz}$. We also notice that, as we increase the injected power, κ_i decreases and reaches a minimum value of $2\pi \times 0.98\,\text{MHz}$ for $P = -105$ dBm.

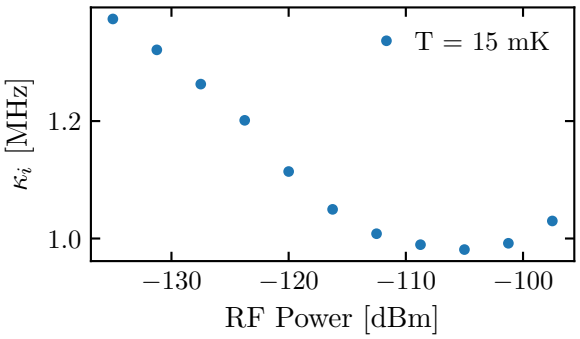

Figure 2.7: Variation of the intrinsic losses as a function of the injected rf power.

This behavior can be addressed to the presence of two level system (TLS) in the substrate [39], even though a more detailed analysis of the loss mechanism would be required to definitively confirm this hypothesis.

2.2 grAl cavity coupled to a junction

In this section we discuss the grAl cavity that we use for the realization of the experiment. All the details about the design of the circuits are discussed in chapter 1.4. Here we focus on the fabrication process and on the measurement of the cavity with the DBR without any junction coupled to it.

2.2.1 Fabrication

The grAl cavity is made of a 0.5 µm wide and 200 µm long grAl wire and it is coupled to a 220 µm wide Al stripline through a DBR made of two layers: the first one is a replica of the resonator while the second one is a 20 µm wide and 200 µm long Al wire. In a first step we realize the resonator and the Bragg through an angle evaporation process done using a triple resist layer. After having cleaned the silicon substrate we spin coat it with 300 nm of PMMA 495 A6 and two layers of PMMA 950 A6, each of them 500 nm thick. The resist mask is patterned using a 30 keV electronic microscope with a dose of 600 µC cm^{-2} and it is developed for one minute in MIBK and IPA solution at 25 °C. At the two ends of the structure we pattern a 2.5 µm × 2.5 µm and 220 µm × 220 µm square necessary to contact the resonator to the junction and to the 50 Ω line. The grAl is realized by depositing 10 nm of aluminum at 0° angle (fig. 2.9a), in a controlled oxygen atmosphere with a pressure of 1.1×10^{-5} mbar and at a controlled rate of 1.5 Å s^{-1}. In a following evaporation, without exposing the sample to air, we deposit 30 nm of pure Al with an angle of 45° in the direction perpendicular to the one of the wires (fig. 2.9b). Because of the total thickness of the resist and of the angle of the evaporation, only the regions whose total width exceeds 1.3 µm are deposited. In this way we manage to have pure Al only on the second layer of the Bragg and on the squares at the two ends, leaving the resonator and the first layer of the Bragg in grAl. The lift off is done in DMSO at a temperature of 80 °C for approximately two hours.

In a second step we realize the 50 Ω stripline and the ground plane for the junction (fig. 2.9c). This is done through lift off with optical lithography. The sample is spin coated with AZ514 resist that was pre-baked at 110 °C for one minute. An inverted copy of the pattern is exposed at 5 mJ cm^{-2}. The sample, after being post baked at 120 °C for 2 minutes, is exposed to UV light for 40 seconds and is developed in MF319 for two minutes. The alignment between the stripline and the resonator is done optically and the pattern is designed to overlap with the 220 µm × 220 µm Al square previously deposited. Before the metal deposition, we etch the native aluminum oxide with an argon gun for two minutes. The Ar plasma is accelerated with a 400 V voltage and the ion beam current is of 22 mA. This is followed by a deposition of 60 nm of pure Al. The lift off is done again in DMSO at 80 °C. At the end of the process a 30 nm layer of Nb is deposited at the back of the sample for the ground plane.

Coupling the resonator to a junction

The Al/AlOx/Al junction is realized with angle evaporation using a PMMA bilayer resist without any suspended bridge ('Manhattan style' [40]). We designed a cross-type structure with wires wide 100 nm and by exploiting the aspect ratio of the patterned resist, we are able to selectively deposit metal in only one of the two directions. We first evaporate Pd marks needed to align the pattern of the junction to the preexisting resonator. The marks are patterned using optical lithography and their position is checked using the camera of the

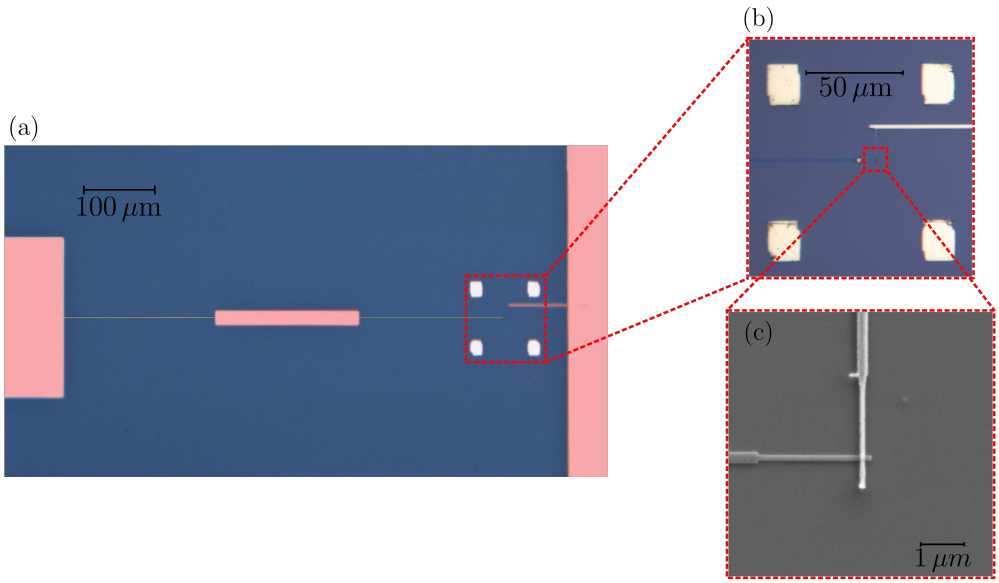

Figure 2.8: (a) False colored optical picture of the cavity with the DBR. In red we color the Al parts i.e. the 50 Ω line on the left, the second layer of the Bragg and the ground plane on the right. The parts in yellow are the grAl parts: the first layer of the Bragg and the $\lambda/4$ cavity. (b) Zoom of the first panel at the position of the junction. (c) SEM picture of a typical junction realized under the same condition.

optical writer. This kind of alignment has a precision of roughly 1 µm since it is limited by the resolution of the camera and by the possible presence of small offset between the optical path of the visible light and the one of the UV laser. In any case, for this kind of structure, this limitation did not constitute a problem.

The sample is spin coated first with a layer of 300 nm of PMMA 495 A6 resist and then with 150 nm of PMMA 950 A3 resist. The junction is patterned with a dose of 650 µC cm^{-2} and the development is done in a solution of MIBK and IPA for one minute at a controlled temperature of 25 °C. The design of the junction is made such that one of the two arms of the cross overlapped with the 2.5 µm × 2.5 µm Al square previously made, while the other one with the ground plane. The first evaporation is done at an angle of 45° in the direction perpendicular to the resonator. We deposit 20 nm of Al at a rate of 9 Å s^{-1}. The layer is exposed to oxygen at a static pressure of 10 mbar for 20 minutes. The second layer, of 60 nm of Al, is deposited, with the same rate, with an angle of 45° in a direction perpendicular to the one the first evaporation. The lift off is done in DMSO at 80 °C (fig. 2.9d).

In a final step we ensured a good dc contact between the junction and both the resonator and the ground plane. By aligning again on the Pd marks, with optical lithography we expose the small surface of metal where the junction overlapped with the resonator and the ground plane. With the Ar gun we removed the native oxide layer and we deposited 80 nm of Al (fig. 2.9e).

The final result is shown in figure 2.8 with the first two panels showing a false colored optical picture and the last one an SEM image of a typical junction realized under the same condition.

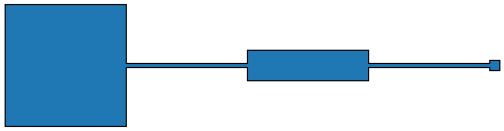

(a) The first step involves the deposition of 10 nm of grAl at 0° angle in a controlled oxygen atmosphere with a pressure of 1.1×10^{-5} mbar.

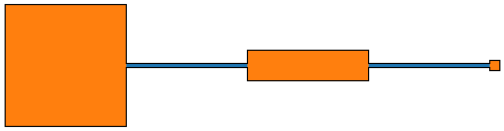

(b) Without exposing the sample to air, we deposit 30 nm of pure Al with an angle of 45° in the direction perpendicular to the one of the wires. Because of the total thickness of the resist and of the angle of the evaporation, only the second layer of the DBR and the two squares placed at the structure are covered

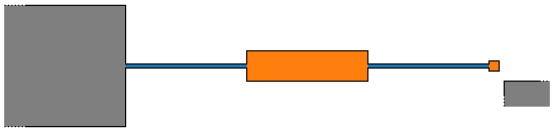

(c) In a different step we realize the 50 Ω line and the ground plane to which we couple the junction. Before the metal deposition, we etch the native aluminum oxide with an argon gun

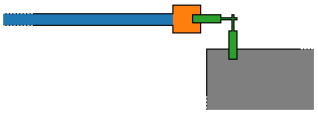

(d) We realize an Al/AlOx/Al junction placed at the end of the cavity.

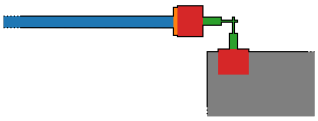

(e) Using the Ar gun we remove the oxide from the pad at the end of the cavity and from the ground and we evaporate 80 nm of Al to connect all the elements of the circuit

Figure 2.9: Main steps of the fabrication process for the realization of the cavity coupled to an SIS junction

2.2.2 Cavity characterization

The expected kinetic inductance of the grAl is 650 pH/□. Keeping into account the width of the line, the inductance per unit length is $L_l = 1.3 \times 10^{-3}\,\mathrm{H\,m^{-1}}$ while the capacitance extracted from Sonnet is $C_l = 3.5 \times 10^{-11}\,\mathrm{F\,m^{-1}}$. These parameters give us a line with impedance $Z = 6.1\,\mathrm{k\Omega}$ and velocity $v_p = 4.68 \times 10^{6}\,\mathrm{m\,s^{-1}}$. We simulate the spectrum of the circuit in a region between 4 GHz and 8 GHz and we obtain a cavity mode resonance frequency of $\omega_1 = 2\pi \times 6.22\,\mathrm{GHz}$ and a coupling rate $\kappa_c = 2\pi \times 250\,\mathrm{kHz}$. We verified this predictions by measuring the spectrum at $T = 10\,\mathrm{mK}$ and with $P = -138$ dBm, that we fit using equation 2.4. The first cavity resonance frequency is found to be at $\omega_1 = 2\pi \times 5.78\,\mathrm{GHz}$ with $\kappa_i = 2\pi \times 700\,\mathrm{kHz}$ and $\kappa_c = 2\pi \times 270\,\mathrm{kHz}$.

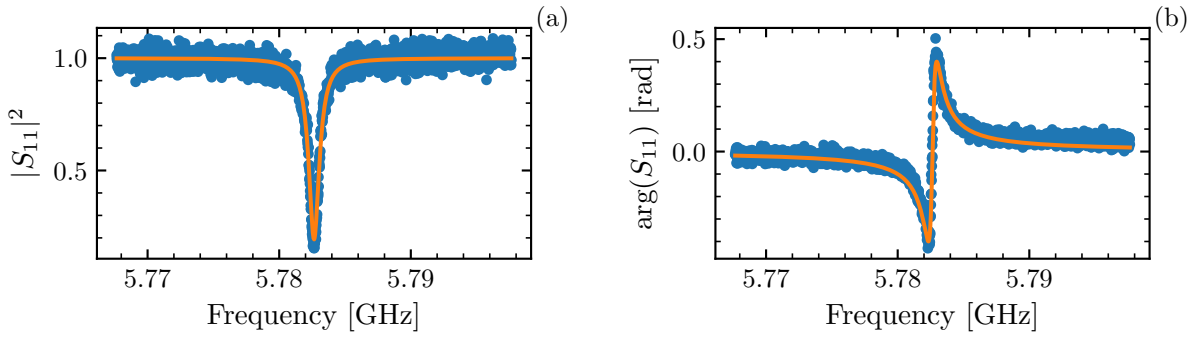

Figure 2.10: (a) Absolute value and (b) phase of the reflection spectrum of the cavity measured at $T = 10\,\mathrm{mK}$ and $P = -138\mathrm{dBm}$.

The small difference between the simulated values and the measured ones is probably linked to a small variation of kinetic inductance respect to the expected one.

Once again, as the rf power injected in the cavity increases, κ_i decreases (fig. 2.11) reaching a minimum value of $\kappa_i = 2\pi \times 235\,\mathrm{kHz}$ for $P = -113\mathrm{dBm}$.

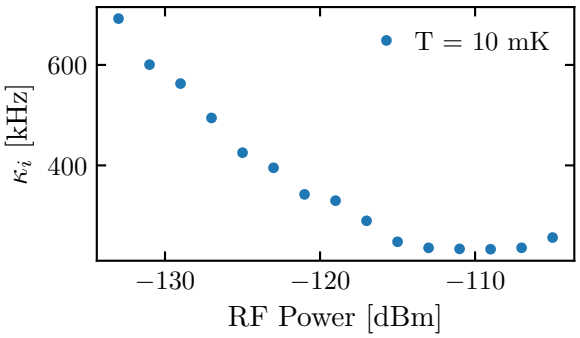

Figure 2.11: Variation of the intrinsic losses as a function of the injected RF power.

2.3 Experimental setup

In this paragraph we describe the experimental setup we used for the measurements.
In the first part we discuss the microwave setup, both cryogenic and at room temperature, that we use for the measurement of the spectrum and of the state of the cavity, while in the second part we focus on the description of the DC biasing lines.

2.3.1 Preparation of the sample

In order to be able to probe the sample we glue it on a gold-plated copper sample holder and connect it, through Al bonding wires, to a printed circuit board (PCB). The PCB consists in a via to the ground and in a 50 Ω microstrip that terminates in an SMA connector (fig. 2.12). The sample holder is shielded using an absorptive epoxy material, to block high frequency radiation, and fixed on the 10 mK stage of a Cryoconcept dilution refrigerator.

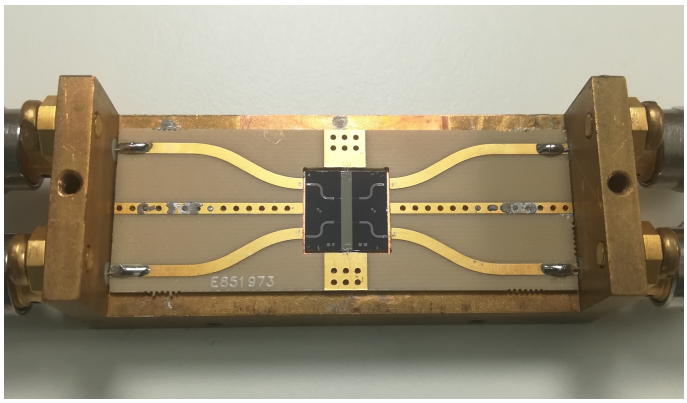

Figure 2.12: Picture of the sample holder and of the PCB to which the sample is bonded.

2.3.2 Microwave setup

Cryogenic cabling

A scheme of the cryogenic microwave lines is shown in figure 2.13. Both for the injection and for the detection lines we use 50 Ω coaxial cable with SMA connectors. Between the 300 K and 4 K stage we use stainless steel cable while for the lower temperature stages we use superconducting niobium-titanium cables thermalized at 1 K and 100 mK. To reduce thermal noise, the injection line is attenuated at different stages with a total attenuation of −80 dB. Since we perform reflection measurement we use a Quinstar circulator to separate the pump from the reflected signal and, to be able to DC voltage bias the junction while probing the cavity with microwave signal, we use an Anritsu bias tee placed before the sample. The reflected signal is amplified with an HEMT Low-Noise cryogenic amplifier with a gain of 40 dB and a noise temperature of 2 K. To protect the cavity from noise propagating back from the amplifier we use two circulators with a 4 GHz - 8 GHz bandwidth and an isolation of respectively 18 and 27 dB. For the signal with frequency out of the bandwidth of the circulators, we use a 8 GHz low pass filter and a 4 GHz high pass filter. All the connections

on the 10 mK stage are done using flexible copper cables. Given the total attenuation present

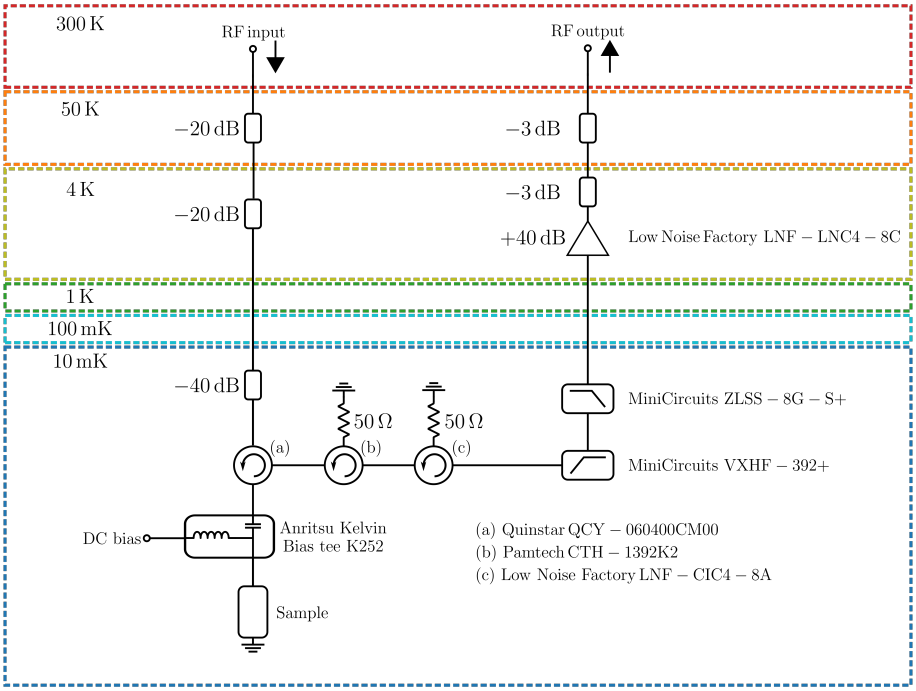

Figure 2.13: Cryogenic microwave setup used for the measurement of the sample

on the two lines we can compute the expected number of thermal photons in the cavity at frequencies close to the ones of the three highest coupled mode ($2\pi \times 2\,\mathrm{GHz}$, $2\pi \times 6\,\mathrm{GHz}$ and $2\pi \times 16\,\mathrm{GHz}$). The number of thermal photons at each stage of the line is given by the number of photons at the previous stage, attenuated by a factor D, plus the photons emitted by a black body at temperature T weighted with a factor $1 - D$ [41]:

$$n_{\mathrm{th},i+1} = D n_{\mathrm{th},i+1} + (1 - D) n_{\mathrm{BE}}(\omega, T). \tag{2.5}$$

D is the attenuation in power of the attenuator, and $n_{\mathrm{BE}}(\omega, T)$ is the thermal population given by a Bose-Einstein distribution at temperature T and frequency ω. For the injection line, the number of thermal photons at each thermal stage is reported in the following table:

	300 K	50 K	4 K	10 mK
$2\pi \times 2\,\mathrm{GHz}$	3120	550	45	4.5×10^{-3}
$2\pi \times 6\,\mathrm{GHz}$	1040	180	15	1.5×10^{-3}
$2\pi \times 16\,\mathrm{GHz}$	390	70	5	5×10^{-4}

For the detection line we consider the amplifier as a black body at 2 K and the attenuation is given by the circulators for the $2\pi \times 6\,\mathrm{GHz}$ mode and by the filters for the high and low frequency modes. The results for the thermal number of photons are:

	2 K	10 mK
$2\pi \times 2\,\mathrm{GHz}$	20	0.1
$2\pi \times 6\,\mathrm{GHz}$	6	1×10^{-4}
$2\pi \times 16\,\mathrm{GHz}$	2	2×10^{-8}

In the calculation of n_{th} for the $2\pi \times 2\,\text{GHz}$ and $2\pi \times 16\,\text{GHz}$ mode, we assumed that the isolation of the two circulators at these frequency is 0 dB. This is clearly an overestimation and therefore we expect the actual number of thermal photons to be smaller than the one we calculated.

Room temperature electronics

For the measurement of the spectra we use a Rohde&Schwarz ZND VNA, while to perform two tone spectroscopy, we use as a second pump an Agilent E8257D microwave source that we inject in the line using a Krytar directional coupler.

To characterize the quantum state of the cavity we evaluate the statistical moments of the field operator $\langle (\hat{a}^\dagger)^n \hat{a}^m \rangle$ from the measurement of the moments of the two quadratures of the cavity field [42]. To measure them we use the setup shown in figure 2.14.

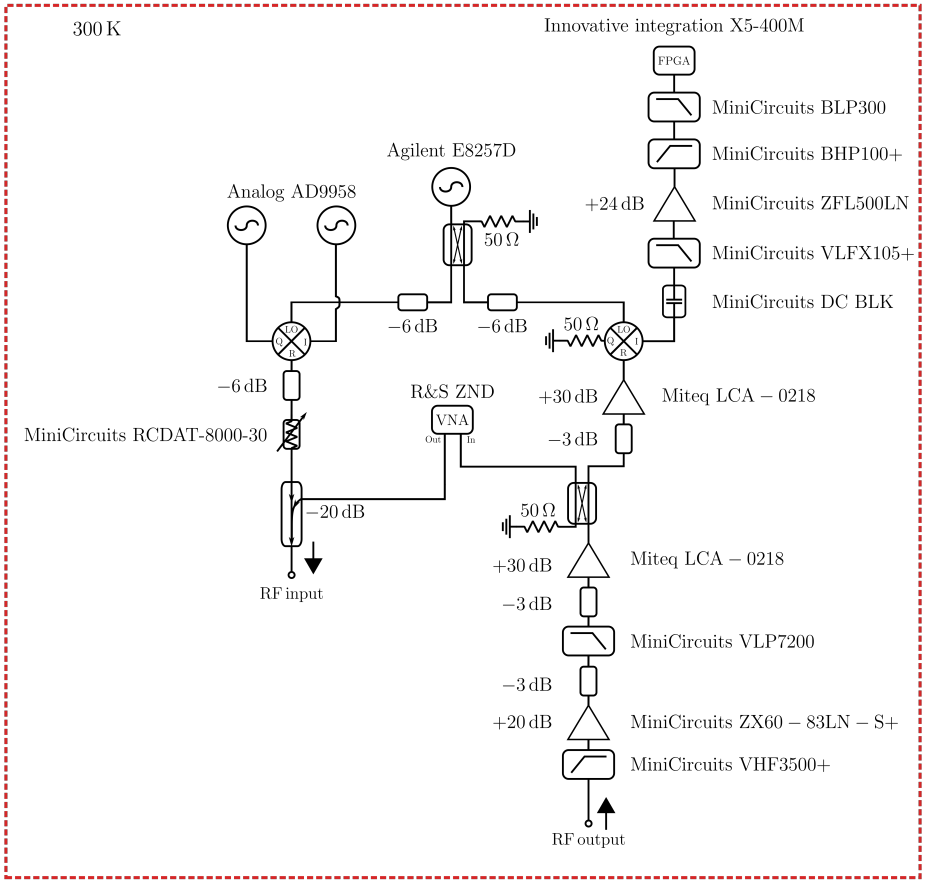

Figure 2.14: Room temperature setup used for the measurement of the two quadratures of the cavity field.

To excite the cavity we use a single side band modulation scheme. Using a DAC we generate a signal of frequency $\omega_{\text{IQ}} = 2\pi \times 100\,\text{MHz}$ that we upconvert through an IQ mixer to the frequency of the cavity mode. For the local oscillator we use the Agilent microwave source with a frequency ω_{LO} chosen such $\omega_{\text{LO}} = \omega_1 - \omega_{\text{IQ}}$. The output of the IQ mixer $S(t)$ are the carrier with frequency ω_{LO} (due to some unwanted leakage) and two side bands with

frequency $\omega_{\mathrm{LO}} \pm \omega_{\mathrm{IQ}}$:

$$S(t) = I(t)\sin(\omega_{LO}t) + Q(t)\cos(\omega_{LO}t), \tag{2.6}$$

with $I(t)$ and $Q(t)$ being equal to:

$$I(t) = I_0\sin(\omega_{IQ}t + \phi_I) \qquad Q(t) = Q_0\sin(\omega_{IQ}t + \phi_Q). \tag{2.7}$$

By properly tuning the relative phase and amplitude of the $I(t)$ and $Q(t)$ signal we are able to suppress the lower side band and local oscillator pump and have as injected signal only the one at frequency $\omega_1 = \omega_{\mathrm{LO}} + \omega_{\mathrm{IQ}}$. In particular, when $I_0 = Q_0$ and $\phi_I - \phi_Q = \pi/2$ we get:

$$S(t) = A\sin\left((\omega_{\mathrm{LO}} + \omega_{\mathrm{IQ}})t\right). \tag{2.8}$$

In our case the carrier with frequency ω_{LO} had an input power 21 dB smaller than the higher side band, while the lower side band was 43 dB smaller. The signal is then attenuated and connected to the input line of the fridge. To be able to quickly measure the spectrum of the cavity and to precisely adjust the frequency of the local oscillator we also connect the VNA through a directional coupler. The detected signal is filtered and amplified, with a chain containing two filters and two low noise amplifier, before being split by an hybrid coupler. Half of the signal is sent to the VNA for the measurement of the spectrum while the other half, after being amplified again, is downcoverted by another IQ mixer. As local oscillator, we use the same signal used for the up conversion process. We collect one of the two quadratures that we send to a data acquisition FPGA, equipped with an ADC, that samples the incoming signal at a rate of $400\,\mathrm{MS\,s^{-1}}$.

To prevent the saturation of one of the amplifier or of the mixer we add attenuation to limit the amplitude of the collected signal. Moreover, to verify that the added noise is dominated by the cryogenic amplifier, we measure the integrated power of the noise at each stage of amplification with the low temperature amplifier turned off and on. We always get that, with the cryogenic amplifier turned on, the integrated noise is 9 dB higher. In figure 2.15 we report an histogram of the time trace of the noise acquired with the FPGA card.

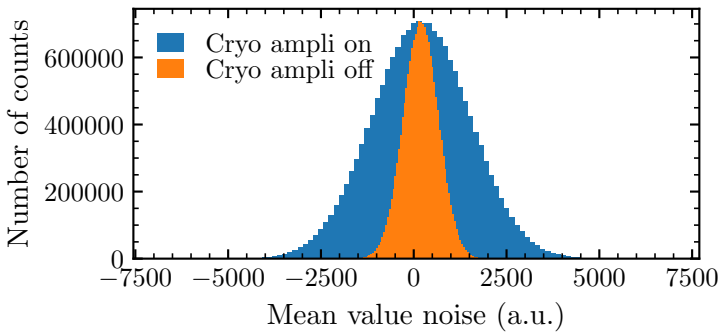

Figure 2.15: Histogram of the time trace of the noise measured using the FPGA card with the cryogenic amplifier on and off. The width of the gaussian is broader when the low temperature amplifier is on, meaning that the added noise is mainly coming from that stage of amplification.

2.3.3 DC bias setup

To DC bias the junction we use two different setups, shown in figure 2.16. The first one (setup A) allows us only to voltage bias the junction while the second one (setup B) also to measure the current flowing through it. In both cases, to connect the 300 K setup to the cold stage, we use Bluefors thermocoax lines, with a room temperature resistance of 150 Ω and a cutoff frequency of 3 MHz. As DC bias source we use a Yokogawa 7651 together with a voltage divider used to suppress the voltage noise injected in the line. The divider is composed of a 1 MΩ resistor placed at room temperature and of a 110 Ω resistor connected to the ground on the 10 mK stage. To filter the noise we use a 100 nF grounded capacitor that, together with the 110 Ω resistor, realizes an *RC* filter with an expected cutoff frequency of 15 kHz. In the setup B we also place a 10 kΩ resistor in series with the sample, that we use to measure the current flowing through the junction.

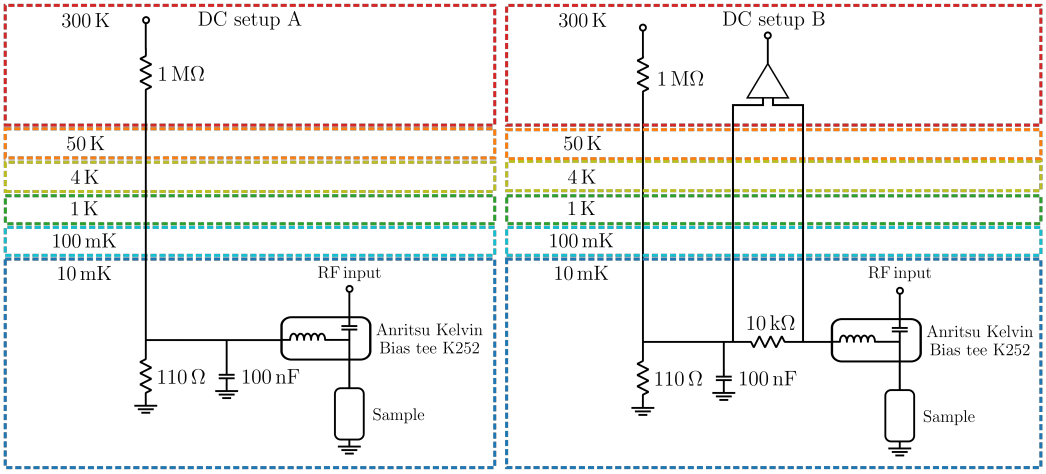

Figure 2.16: DC setup we use to bias the junction. The setup B allows us also the measure the current.

We can estimate the amplitude of the thermal voltage noise $\delta V^2_{\mathrm{RMS}}$ shined on the sample, by the resistors present in the circuit, using [14]:

$$\delta V^2_{\mathrm{RMS}} = 4k_B T R \Delta f, \tag{2.9}$$

where Δf is the bandwidth of the circuit. Because the voltage fluctuations due to the room temperature resistor are reduced by the voltage divider, we only consider the noise contribution coming only from the 110 Ω. Since the bandwidth of the circuit is given by the *RC* filter, the thermal voltage noise is equal to:

$$\delta V^2_{\mathrm{RMS}} = 4k_B T R \frac{1}{2\pi} \int_0^\infty \frac{1}{1 + R^2 C^2 \omega^2} d\omega = \frac{k_B T}{C}, \tag{2.10}$$

from which we get $\delta V_{\mathrm{RMS}} = 1.2\,\mathrm{nV}$.

Conclusions

In this chapter we discussed the experimental realization and characterization of high impedance cavities focusing in particular on two NbSi resonators and one made in grAl one to which we couple the SIS junction. To characterize the behavior of disordered superconductors we measured the cavities as a function of temperature, DC bias current and microwave power. We have seen that the behavior of the samples with temperature can be explained with Mattis-Bardeen theory and that the effect of the DC current on the cavity can be neglected if the current is on the order of the junction's critical current. We proved that we are able, starting from the room temperature resistance and the superconducting critical temperature, to correctly predict the properties of a cavity with a DBR. We concluded the chapter discussing in detail the experimental setup used for the measurement of the cavity's field.

Chapter 3

Effect of quasiparticle tunneling on the cavity dynamics

Contents

The interaction between a microwave resonator and the quasiparticle degree of freedom of a Josephson junction has been previously studied in several works [43, 44]. It has been shown that the variation of the quantum admittance of the junction, at voltages near the superconducting gap, causes a change of resonant frequency and of intrinsic loss rate of the resonator. In those works, the resonators had a low impedance and a low quality factor and were mainly used as a tool to probe the admittance of the junction at microwave frequencies. In a more recent paper [27], Silveri and coworkers, using a high finesse cavity weakly coupled to an SIN tunnel junction, managed to better describe and characterize the frequency shift of the energy levels of the resonator. Here, we extend this work to the case of the strong coupling regime and we study how the interaction between the cavity and the junction affects the dynamics of the cavity itself. We show that the evolution of the properties of the resonator cannot be described by a model where the junction is portrait only as a tunable admittance. It is necessary to consider it as an environment to which the resonator, described as an open quantum system, is coupled.

We start by showing the measured evolution of the cavity mode frequency and loss factor as a function of the dc bias voltage through the junction. We compare these results to the classical theory describing the junction as an admittance and show that all the features observed experimentally are not captured by this model. To better understand our data, we consider the theory presented in [31], where the junction is treated as an environment and the resonator as a quantum open system. In this work, Estève and coworkers show that the two main effects arising from the cavity-junction coupling are a shift of the energy levels of the resonator, called Lamb Shift, and an energy exchange between the resonator and the bath in terms of quantum jumps. In the strong coupling regime, these two effects result to be state dependent, which means that different Fock states of the resonator experience a different Lamb shift and a different exchange rate of photons with the junction. Using this model, we are able to explain the shift of the energy levels (section 3.4) and the behavior of the loss rate (section 3.5). In particular, we demonstrate how it is possible to confine the dynamics of the cavity mode to the first two energy levels, creating an effective two-level system (section 3.6).

3.1 Frequency shift and loss rate change: experimental results

In this section, we show the reflected spectrum S_{11} of the $n = 1$ mode of the cavity and we discuss its main features as function of the junction dc voltage bias and the injected microwave power. We show that, as the bias voltage approaches $2\Delta/e - \hbar\omega_1/e$, the resonance experiences a negative shift of its frequency and a broadening of its linewidth before completely disappearing at higher voltages. We also discuss the appearance of more resonances when the injected microwave power is sufficiently high and we investigate their behavior performing a two tone spectroscopy measurement. We will later compare the results presented in this section to the two theoretical models mentioned above.

The setup used for the measurement of the spectra is discussed in detail in chapter 2.3 and shown in a simplified version in figure 3.1. The DC bias setup used is the setup A (2.3.3). The spectra have been measured at a constant temperature of 10 mK and the indicated injected microwave power is calculated taking into account the power of the microwave source and the

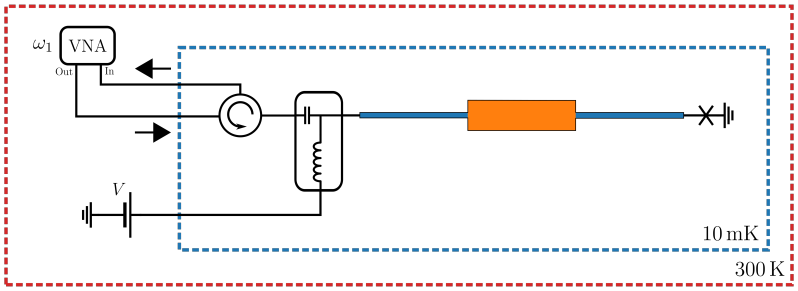

Figure 3.1: Using a VNA spectrum analyzer we measure the reflection spectrum of the cavity at different junction bias voltage.

attenuators present in the injection line. The dissipation due to the cables is not included, thus the quoted power overestimate the actual one by a few dB.

3.1.1 Single tone spectroscopy

In figure 3.2, we show an image of $|S_{11}|^2$, measured at voltages smaller than $2\Delta/e$ ($\Delta \approx 200\,\mu\text{eV}$). As the value of the bias voltage approaches $2\Delta/e - \hbar\omega_1/e$ (red dashed line), with $\omega_1 \approx 2\pi \times 5.91\,\text{GHz}$ and $\hbar\omega_1 \approx 24\,\mu\text{eV}$, the resonant frequency of the cavity experiences a negative shift of approximately $2\pi \times 100\,\text{MHz}$. At higher voltages, the resonance is not visible any more and we use the spectrum measured at $V = 460\,\mu\text{V}$ to normalize the spectra measured at lower voltages.

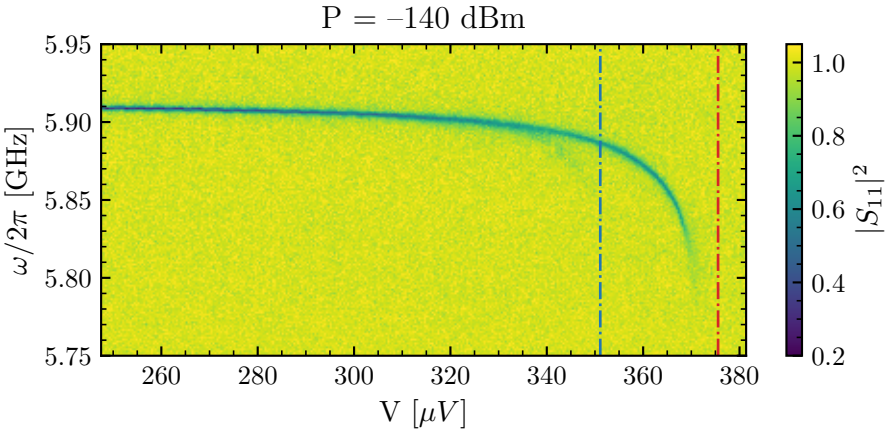

Figure 3.2: $|S_{11}|^2$ measured at voltages below $2\Delta/e$. The resonant frequency of the cavity decrease as the voltage gets closer to $2\Delta/e - \hbar\omega_1/e$ (red dashed line). A second resonance is visible at voltages just below $2\Delta/e - 2\hbar\omega_1/e$ as indicated by the blue line.

When the bias voltage is higher than $eV > 2\Delta - \hbar\omega_1$, photo-assisted quasiparticle tunneling can happen and the junction absorbs photons from the cavity. This increases the intrinsic loss rate κ_i, which becomes much larger than the coupling rate κ_c and causes the resonance to disappear ($|S_{11}| = 1$ if $\kappa_i \gg \kappa_c$). At the same time, causality relations (Kramers-Kronig

relations) impose a change of the resonant frequency of the cavity, and hence the measured shift. In order to quantify the frequency shift and the loss rate, we fit the absolute value and the phase of S_{11} as shown in fig. 3.3, using the following lorentzian linewidth:

$$S_{11} = 1 - \kappa_c \frac{\kappa/2 - i\delta}{(\kappa/2)^2 + \delta^2} \tag{3.1}$$

with δ being the frequency detuning $\delta = \omega - \omega_1$, and κ the linewidth of the cavity given by the sum of the intrinsic loss rate κ_i and the coupling rate κ_c.

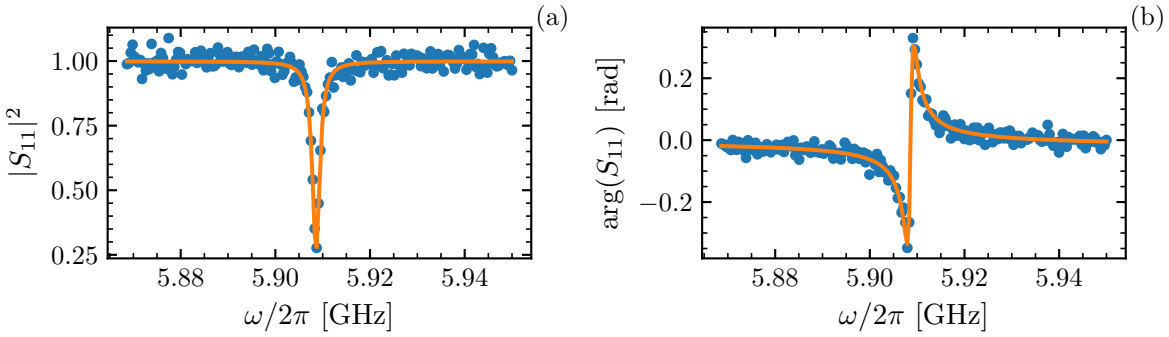

Figure 3.3: (a) Absolute value and (b) phase of S_{11} measured at $V = 250\,\mu\text{V}$ with $P = -140$ dBm. From the lorentzian fit (in orange), we get $\omega_1 = 2\pi \times 5.91\,\text{GHz}$ and $\kappa = 2\pi \times 1.5\,\text{MHz}$. The coupling κ_c is obtained by fitting simultaneously the curves at all voltages. It is equal to $2\pi \times 450\,\text{kHz}$.

By fitting all the measured spectra, we obtain the voltage dependence of the resonant frequency ω_1 and of the loss rate κ as shown in figure 3.4. The coupling rate κ_c is supposed to be constant and equal to $2\pi \times 450\,\text{kHz}$. It is obtained by fitting simultaneously all the measured curves using the same parameter.

The resonant frequency goes from $\omega_1 = 2\pi \times 5.91\,\text{GHz}$ at $250\,\mu\text{V}$ to $\omega_1 = 2\pi \times 5.81\,\text{GHz}$ at $370\,\mu\text{V}$ which is the highest voltage at which we are able to fit the peak. At the same time, the intrinsic loss rate increases from $\kappa = 2\pi \times 1.5\,\text{MHz}$ up to $\kappa = 2\pi \times 8.5\,\text{MHz}$ at $eV \approx 2\Delta - 2\hbar\omega_1$. After this voltage, κ remains almost constant, and then increases above $2\pi \times 30\,\text{MHz}$ when $eV = 2\Delta - \hbar\omega_1$. The small oscillations present both in ω_1 and in κ for voltages smaller than $300\,\mu\text{V}$, are linked to the interaction between the cavity and the Cooper pairs.

Anharmonicity

The larger linewidth measured close to $350\,\mu\text{V}$ is not linked to an increase of the intrinsic loss of the cavity, but is due to the anharmonicity of the spectrum. This is clearly seen in figure 3.2, where the spectrum shows the appearance of a faint resonance at voltages close to $2\Delta - 2\hbar\omega_1$ (blue dashed line). To better investigate this behavior, we measure, with a finer voltage sweep, the spectrum of the cavity around $340\,\mu\text{V}$ for different microwave powers. In figure 3.5, one sees that, when the microwave power increases, the resonance splits in two peaks.

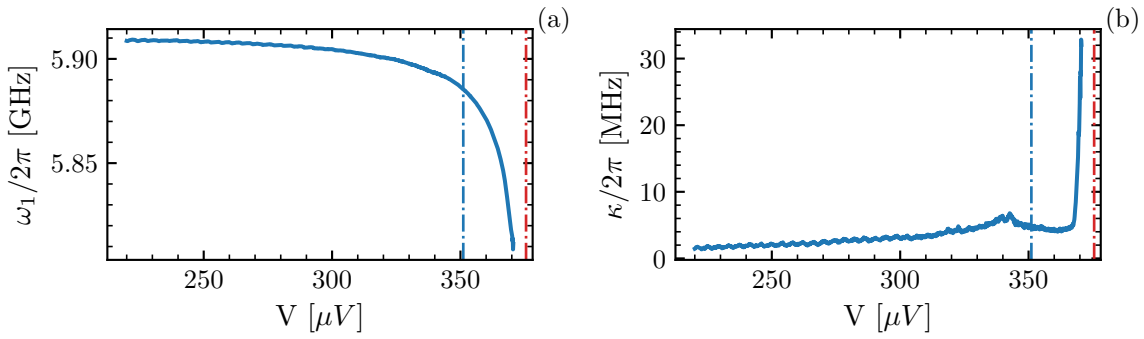

Figure 3.4: (a) ω_1 and (b) κ obtained from the fit of the spectra shown in 3.2, measured at different bias voltage.

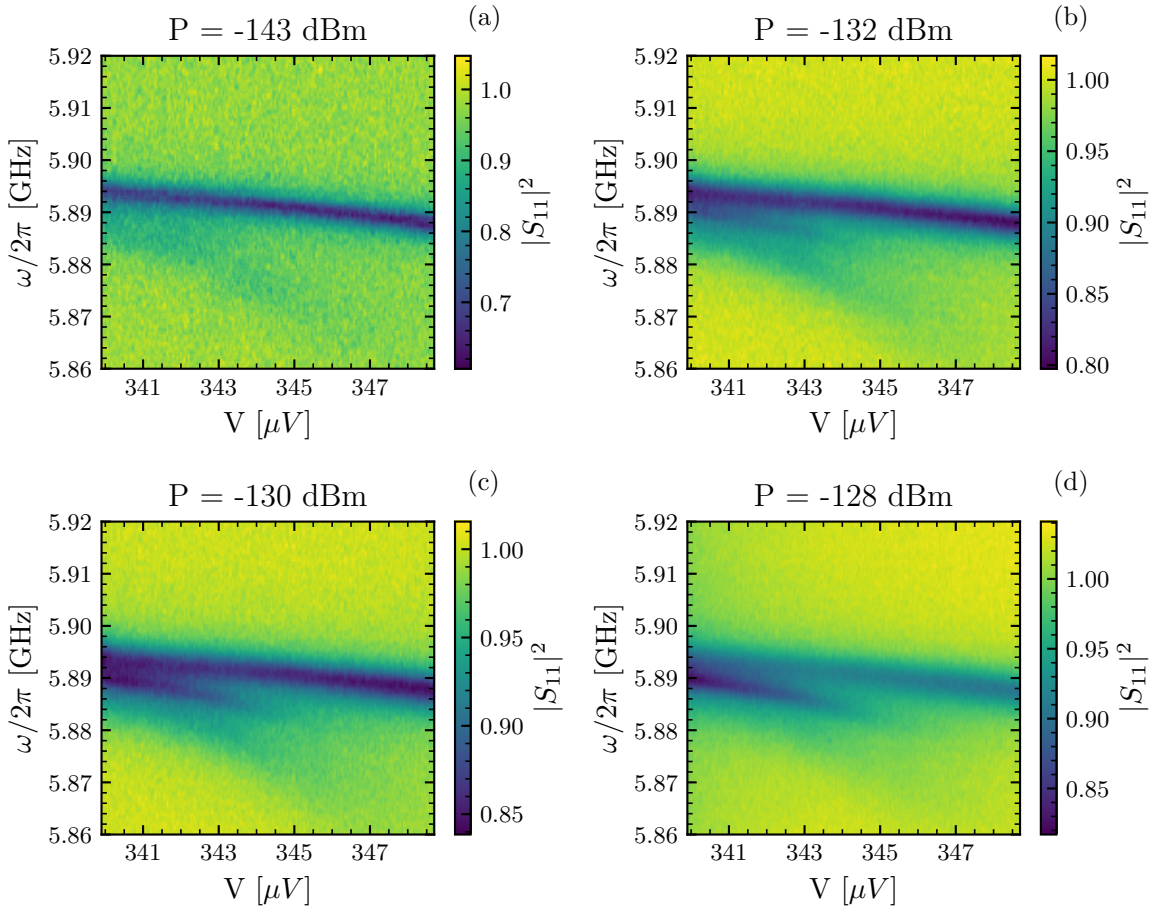

Figure 3.5: Finer voltage sweep of $|S_{11}|^2$ around 340 µV. The Different panels correspond to different microwave power: (a) $P = -143$ dBm, (b) $P = -132$ dBm, (c) $P = -130$ dBm, (d) $P = -128$ dBm.

This is typical of an anharmonic spectrum, where the $|0\rangle \rightarrow |1\rangle$ and the $|1\rangle \rightarrow |2\rangle$ transitions have different resonant frequencies (figure 3.6). When the microwave power is small, only the ω_1^{10} transition[1] is visible. At higher power, two photons process are more visible and hence two resonances are observed: one at ω_1^{10} and one at $\omega_1^{20}/2$.

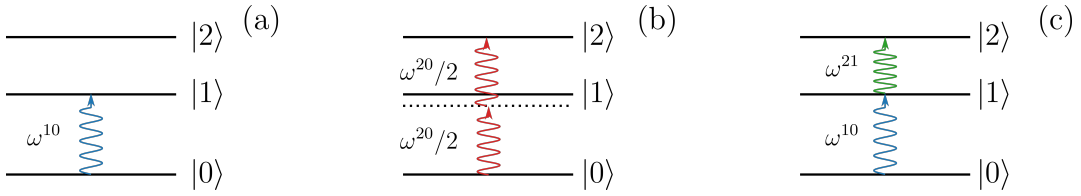

Figure 3.6: Different excitation process for the first three levels of an anharmonic spectrum. When only one tone is present, one can have either single photon processes (a) where the cavity is excited to the first energy level or two photon processes (b) where the cavity is excited to the second energy level. When two tones are present (c) the cavity can be excited to the second energy level due to the absorption of photons of different frequencies.

3.1.2 Two tone spectroscopy

To better probe the anharmonicity, we perform a two tone spectroscopy measurement. We expect that this measurement will probe the $|1\rangle \rightarrow |2\rangle$ transition and the loss rate of the $|2\rangle$ state. We tune the first tone at the transition frequency ω_1^{10} measured in the low power regime (figure 3.4a) and, using a second microwave tone, we measure S_{11} as shown in figure 3.7. The power of the two pumps are $P_1 = -128$ dBm and $P_2 = -135$ dBm. P_1 was chosen small enough to not populate the higher levels, as observed in the single tone measurement shown in fig. 3.5d, where the linewidth of the cavity is sufficiently small to allow us to resolve the two resonant peaks. This transition frequency follows the same trend of the ω_1^{10} with a negative frequency shift of $2\pi \times 40\,\text{MHz}$ when $eV \approx 2\Delta - 2\hbar\omega_1$ instead of $eV \approx 2\Delta - \hbar\omega_1$. The resonance disappears at voltages above $2\Delta/e - 2\hbar\omega_1/e$ (blue dashed line). Again this is due to the absorption of photons by the junction, for voltages higher than $2\Delta/e - 2\hbar\omega_1/e$, photo-assisted quasiparticle tunneling with two photon absorption is allowed. The spectrum also shows small dips at lower voltages which are a contribution of higher energy levels.

From the fit of the spectrum, we obtain ω_1^{21} and the linewidth of the second energy level κ_2. We plot them in figure 3.8 together with the transition frequency ω_1^{10} and the first energy level loss rate κ_1.

By comparing these two curves, one clearly sees how the interaction between the cavity and the junction is Fock state dependent. At low bias, the two frequencies are the same, meaning that far from 2Δ the spectrum of the cavity is harmonic for the first Fock states. As eV approaches $2\Delta - 2\hbar\omega_1$ the frequency ω_1^{21} starts to shift, showing a similar behavior to ω_1^{10} when $eV \approx 2\Delta - \hbar\omega_1$. The amplitude of the shift, however, is not the same for the two frequencies. The loss rate of the first two energy levels are identical at small bias and increase with voltage. The rate κ_2 increases drastically at a voltage close to $2\Delta - 2\hbar\omega_1$ while κ_1 experiences the same effect at $2\Delta - \hbar\omega_1$.

[1] With ω_n^{ij} we indicate the transition frequency between the $|i\rangle$ and $|j\rangle$ energy levels of the n-th mode of the cavity.

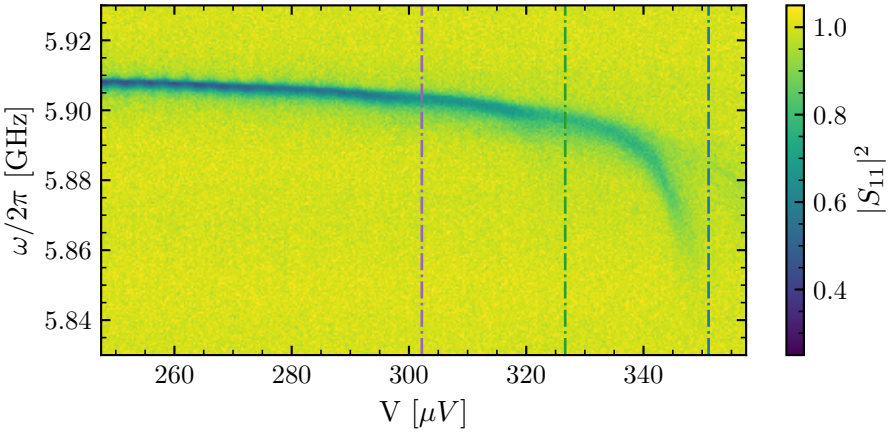

Figure 3.7: $|S_{11}|^2$ measured with two tone spectroscopy. The first pump is tuned with the first energy level transition frequency and has an injection power $P_1 = -118$ dBm. With a second pump, whose microwave power is $P_2 = -135$ dBm, we acquire the spectrum of the cavity. The colored dashed lines indicate the voltage points where $eV = 2\Delta - m\hbar\omega_1$, with $m = 2, 3, 4$.

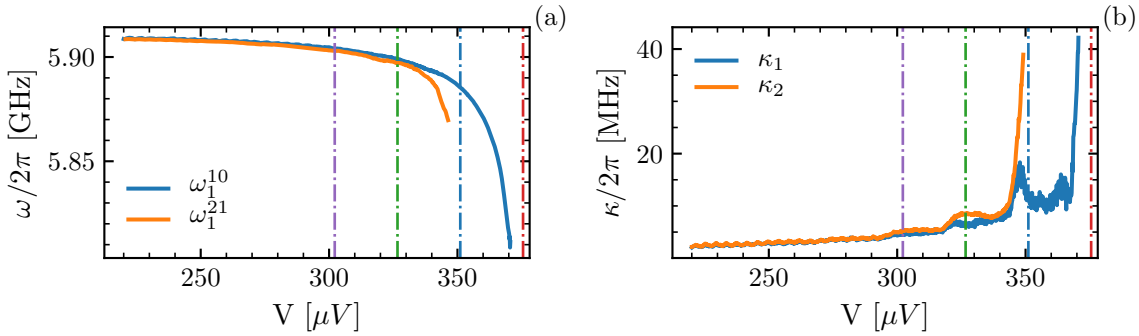

Figure 3.8: (a) Transition frequency and (b) loss rate for the Fock states $|1\rangle$ and $|2\rangle$. Each state experiences a different voltage dependent frequency shift and loss rate. The colored dashed lines indicate the voltage points where $eV = 2\Delta - m\hbar\omega_1$, with $m = 1, 2, 3, 4$.

3.2 Junction as a tunable admittance

In this section, we compare our data to a simple model where the junction is described as a voltage and power dependent admittance. Using this model, we are able to explain the negative shift of the resonant frequency of the cavity and the increase of loss rate for voltages close to $2\Delta - \hbar\omega_1$. However, we are not able to properly fit the experimental data for the frequency shift. Moreover, the value of the impedance of the mode that we obtain from the fit is very far from the expected one. And by construction, this model cannot reproduce the observed anharmonic spectrum.

3.2.1 Theoretical study of the cavity-junction interaction

The voltage dependent admittance of a junction $Y_J(V,\omega)$, irradiated with a microwave signal of frequency ω and amplitude V_{RF} is equal to [25, 45]:

$$\mathrm{Re}[Y_J(V,\omega)] = \frac{1}{V_{\mathrm{RF}}} \sum_{n=-\infty}^{\infty} J_n(\alpha)\left[J_{n+1}(\alpha) - J_{n-1}(\alpha)\right] I_{\mathrm{QP}}\left(V + n\frac{\hbar\omega}{e}\right), \tag{3.2}$$

$$\mathrm{Im}[Y_J(V,\omega)] = \frac{1}{V_{\mathrm{RF}}} \sum_{n=-\infty}^{\infty} J_n(\alpha)\left[J_{n-1}(\alpha) - J_{n+1}(\alpha)\right] I_{\mathrm{KK}}\left(V + n\frac{\hbar\omega}{e}\right), \tag{3.3}$$

with $\alpha = eV_{\mathrm{RF}}/\hbar\omega$ and J_n being the Bessel function of order n. $I_{\mathrm{QP}}(V)$ is the dc current-voltage characteristic of the junction given by:

$$I_{\mathrm{QP}}(V) = \frac{1}{eR_N}\int_{-\infty}^{\infty} dE\, n_R(E) n_L(E+eV)[f(E) - f(E+eV)], \tag{3.4}$$

with R_N being the normal resistance of the junction, $f(E)$ the Fermi-Dirac distribution function and $n_{R,L}(E)$ the density of states on the right and left electrodes of the junction. $I_{\mathrm{KK}}(V)$ is the Kramers-Kroenig transform of $I_{\mathrm{QP}}(V)$ and is defined as:

$$I_{KK}(V) = \mathcal{P}\int_{-\infty}^{\infty} \frac{dV'}{\pi} \frac{I_{\mathrm{QP}}(V') - V'/R_N}{V' - V}, \tag{3.5}$$

with $\mathcal{P}$ indicating the Cauchy principal value.

In the weak pumping limit, meaning when $\alpha \ll 1$, equations 3.2 and 3.3 can be simplified as:

$$\mathrm{Re}[Y_J(V,\omega)] \approx \frac{e}{2\hbar\omega}\left[I_{\mathrm{QP}}(V + \hbar\omega/e) - I_{\mathrm{QP}}(V - \hbar\omega/e)\right], \tag{3.6}$$

$$\mathrm{Im}[Y_J(V,\omega)] \approx \frac{e}{2\hbar\omega}\left[I_{\mathrm{KK}}(V + \hbar\omega/e) + I_{\mathrm{KK}}(V - \hbar\omega/e) - 2I_{KK}(V)\right]. \tag{3.7}$$

In figure 3.9a we show a plot of $I_{\mathrm{QP}}(V)$ and $I_{\mathrm{KK}}(V)$ for voltages near $2\Delta/e$, while in figure 3.9b, we report the real and imaginary part of the admittance $Y_J(V,\omega)$ calculated using equations 3.6 and 3.7.

In order to understand how the junction admittance affects the property of a resonator coupled to it, we consider the simple case of a lumped LC circuit, with resonant frequency $\omega_0 = 1/\sqrt{LC}$ and characteristic impedance $Z_c = \sqrt{L/C}$ connected to an admittance $Y_J(V,\omega)$. The resonant frequency of this circuit can be obtained by solving the equation $\mathrm{Im}[Y(V,\omega)] =$

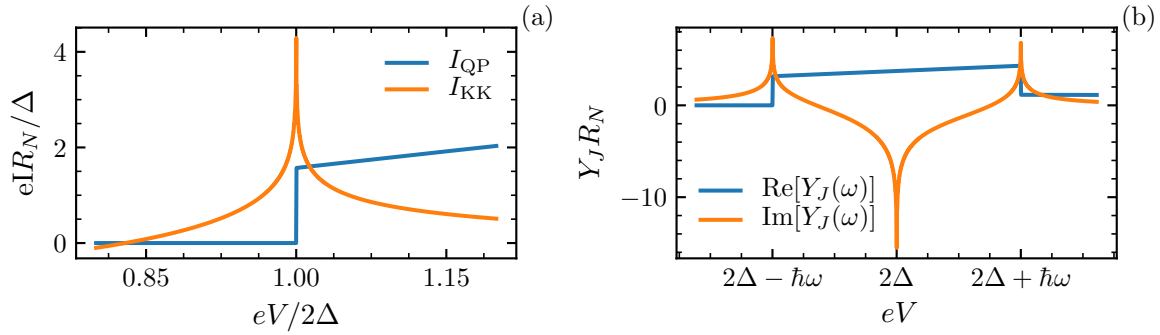

Figure 3.9: (a) Quasiparticle current $I_{\mathrm{QP}}(V)$ and its Kramers-Kroening transform $I_{\mathrm{KK}}(V)$ evaluated at voltages near the superconducting gap. (b) Real and imaginary part of the junction admittance $Y_J(V,\omega)$. $\mathrm{Re}[Y_J(V,\omega)]$ is zero for voltages $eV < 2\Delta - \hbar\omega$ and approaches $1/R_N$ when $eV > 2\Delta + \hbar\omega$. In between these two points it reaches values bigger than $1/R_N$ and increases linearly with the voltage. $\mathrm{Im}[Y_J(V,\omega)]$, instead, shows two peaks when $eV = 2\Delta \pm \hbar\omega$ and a dip at $eV = 2\Delta$.

0, with $Y(V,\omega)$ referring to the total admittance of the circuit. For frequencies close to ω_0 ($\omega = \omega_0 + \delta\omega$), $\mathrm{Im}[Y(V,\omega)]$ can be written, at first order in $\delta\omega$, as:

$$\mathrm{Im}[Y(V,\omega)] = \delta\omega + \frac{1}{2}\omega_0 Z_c \mathrm{Im}[Y_J(V,\omega_0)]. \tag{3.8}$$

Solving the equation $\mathrm{Im}[Y(V,\omega)] = 0$ and replacing $\mathrm{Im}[Y_J(V,\omega_0)]$ with the expression of equation 3.7, we obtain the resonant frequency shift induced by the junction:

$$\delta\omega(V) = -\frac{1}{4}\frac{e}{\hbar} Z_c \left[I_{\mathrm{KK}}(V + \hbar\omega_0/e) + I_{\mathrm{KK}}(V - \hbar\omega_0/e) - 2I_{KK}(V) \right]. \tag{3.9}$$

In figure 3.10 we plot the normalized frequency shift $\delta\omega/\omega_0$ as a function of voltage.

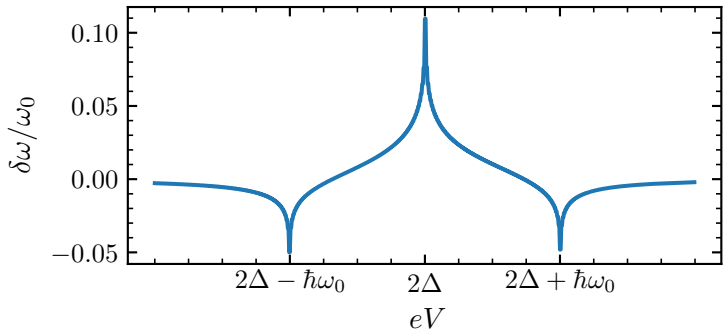

Figure 3.10: Resonant frequency shift as function of the bias voltage for $Z_c = 1\,\mathrm{k}\Omega$ and $R_N = 150\,\mathrm{k}\Omega$. For voltages far from 2Δ, $\delta\omega = 0$. As the bias voltage approaches $2\Delta/e \pm \hbar\omega_0/e$, ω_0 drops, reaching its minimum value.

The loss rate of the resonator is also affected by the admittance of the junction. The non zero $\mathrm{Re}[Y_J(V,\omega_0)]$, for $eV > 2\Delta - \hbar\omega_0$, introduces losses in the resonator, limiting its intrinsic quality factor to $1/(Z_c\mathrm{Re}[Y_J(V,\omega_0)])$, which gives a loss rate equal to:

$$\kappa_i = \omega_0 Z_c \mathrm{Re}[Y_J(V,\omega_0)]. \tag{3.10}$$

This simple derivation can be easily extended to the case of a multi-mode cavity by treating each mode independently. Equations 3.9 and 3.10 are equivalent to the ones found in [27] where it is shown that they perfectly describe the behavior of a cavity in the weak coupling regime.

3.2.2 Comparison with experimental results

We now compare the model to the experimental data presented in section 3.1. Because this model does not predict different transition frequency shift, we only apply it to the data obtained in the low power regime, with a single tone. We fit the ω_1^{10} frequency shift using equation 3.9 and leave as free parameters of the fit the impedance of the mode Z_c and the superconducting gap energy Δ. The value of normal resistance used for the calculation of I_{KK} is the one measured experimentally and equal to 220 kΩ (see appendix B). The values obtained from the fit, that we show in figure 3.11 together with the experimental data, are $Z_c = 2\,\mathrm{k\Omega}$ and $2\Delta = 396\,\mu\mathrm{eV}$. While the value of the gap energy is close to the one we expect, the impedance of the mode is much smaller than the one obtained from electromagnetic simulations of the circuit which is close 5 kΩ, assuming a junction capacitance $C_J = 2\,\mathrm{fF}$. One could try to explain this big difference between the fit and the simulation with an underestimation of C_J. However, if this was the case, we would need a capacitance bigger than 10 fF. This value is not compatible with the junction size nor with the measured resonance frequencies (see section 1.4.3). We will show in the next section how, using a more refined model, we are able to fit better the data and to extract more accurate values for the mode impedance.

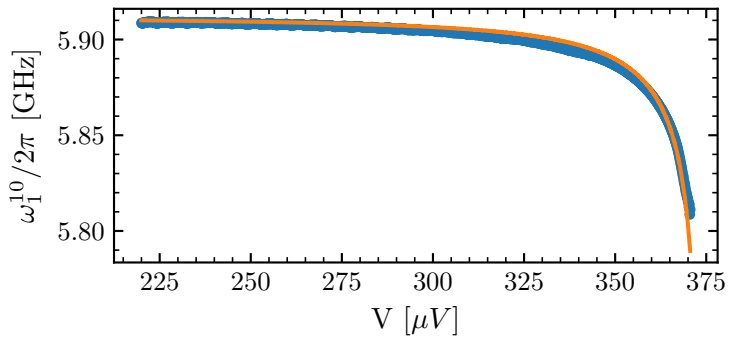

Figure 3.11: ω_1^{10} frequency together with the fit done considering the junction only as an admittance. The value of impedance of the mode obtained from the fit is 2 kΩ and it is not compatible with the expected value obtained from electromagnetic simulations.

3.3 Junction as a tunable environment coupled to a quantum resonator

In this section, we study the effect of the interaction of the quasiparticle degree of freedom of the junction and the cavity, by treating the junction as a bath and by deriving the master equation, in the Lindblad form, for the cavity density matrix ρ. We follow the derivation presented in [31] that we extend to the case of a multi-mode cavity. We then focus in studying the two main properties arising from the cavity-junction coupling: the energy level Lamb shift and the exchange of photons between the cavity and the junction.

3.3.1 Quantum jump operators

We have seen, in the introduction, that the interaction hamiltonian between the cavity and the quasiparticles of the junction is [21]:

$$\hat{H}_I = T \sum_{k,q} \hat{c}^\dagger_{R,k} \hat{c}_{L,q} e^{i\frac{e}{\hbar}\hat{\Phi}_J} + \text{h.c.}, \tag{3.11}$$

where $\hat{\Phi}_J$ is the electromagnetic flux across the junction. This can be rewritten in term of the dc voltage bias V and of the cavity's mode zero point fluctuations $\Phi_{\text{ZPF},n}$ as: $\hat{\Phi}_J = Vt - \sum_n \Phi_{\text{ZPF},n}(\hat{a} + \hat{a}^\dagger)$, with n indexing the cavity mode. We have also shown in section 1.1 that the mode's zero point fluctuations are equal to $\sqrt{\hbar\tilde{Z}_n/2}$, with $\tilde{Z}_n$ being the effective impedance of the mode that depends on its mode volume v_n and on the cavity's capacitance per unit length. Substituting this definition into hamiltonian 3.11 leads to:

$$\hat{H}_I(t) = T \sum_{k,q} \hat{c}^\dagger_{R,k} \hat{c}_{L,q} e^{-i\omega_b t} e^{i\sum_n \Lambda_{n,\text{qp}}(\hat{a}_n + \hat{a}^\dagger_n)} + \text{h.c.}, \tag{3.12}$$

with ω_b being the bias frequency $\omega_b = eV/\hbar$ and $\Lambda_{n,\text{qp}} = \sqrt{\pi\tilde{Z}_n/R_K}$.

In order to write the master equation for the resonator density matrix ρ, in the Lindblad form, we expand the displacement operator in the Fock state basis:

$$e^{i\sum_n \Lambda_{n,\text{qp}}(\hat{a}_n + \hat{a}^\dagger_n)} = \prod_n e^{i\Lambda_{n,\text{qp}}(\hat{a}_n + \hat{a}^\dagger_n)} = \prod_n \sum_{l_n=-\infty}^{\infty} \hat{A}^{(n)}_{l_n} = \sum_{l_0,\ldots,l_n=-\infty}^{\infty} \hat{A}_{l_0,\ldots,l_n}, \tag{3.13}$$

with $\hat{A}_{l_0,\ldots,l_n} = \prod_n \hat{A}^{(n)}_{l_n}$. For a given mode, the $\hat{A}_l$ operators are quantum jump operators that depend on the coupling of the mode Λ_{qp} and are defined, for positives l, as:

$$\hat{A}_{l>0} = \sum_{m=0}^{\infty} |m+l\rangle \langle m+l| \, e^{i\Lambda_{\text{qp}}(\hat{a}+\hat{a}^\dagger)} \, |m\rangle \langle m| \,. \tag{3.14}$$

The operators with $l < 0$ can be obtained using the property: $\hat{A}_{-l} = (-1)^l \hat{A}^\dagger_l$. Their effect is to create l photons in the mode of the cavity when $l > 0$ and destroy $-l$ photons in the same mode when $l < 0$:

$$\hat{A}_l \, |m\rangle = w_{m,l}(\Lambda_{\text{qp}}) \, |m+l\rangle \,, \quad l \geq 0, \tag{3.15}$$

$$\hat{A}_{-l}\,|m\rangle = (-1)^l w_{m-l,l}(\Lambda_{\rm qp})\,|m-l\rangle\,, \quad l \geq 0. \tag{3.16}$$

Here $w_{m,l}(\Lambda_{\rm qp})$ indicates the matrix element of the operator that can be calculated using generalized Laguerre polynomials $L_m^{(l)}$ as [46, 47]:

$$w_{m,l}(\Lambda_{\rm qp}) = \langle m+l|\, e^{i\Lambda_{\rm qp}(\hat{a}+\hat{a}^\dagger)}\,|m\rangle = \sqrt{\frac{m!}{(m+l)!}} e^{-\Lambda_{\rm qp}^2/2} (i\Lambda_{\rm qp})^l L_m^{(l)}(\Lambda_{\rm qp}^2), \tag{3.17}$$

The variation of the matrix elements with low m and l is shown in fig. 3.12 as function of the squared coupling amplitude $\Lambda_{\rm qp}^2$.

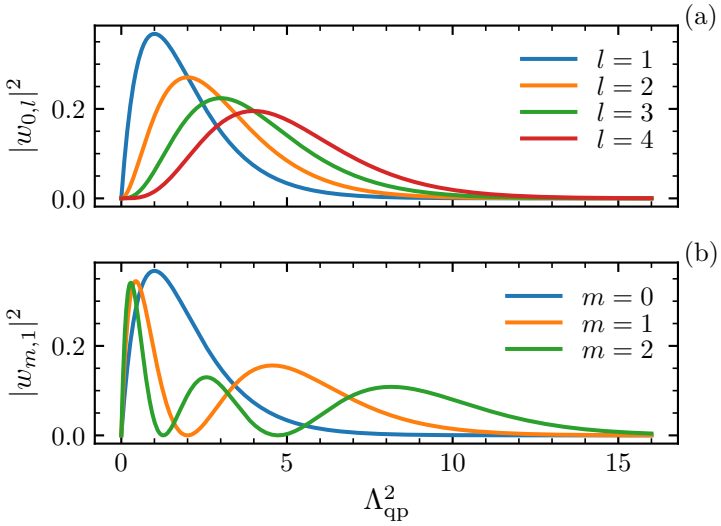

Figure 3.12: Matrix element $w_{m,l}$ as function of the squared coupling $\Lambda_{\rm qp}^2$. In the strong coupling regime ($\Lambda_{\rm qp} \approx 1$) the high order element that couples non adjacent Fock states cannot be neglected and the single photon process depends on the initial and final state. The matrix elements also exhibit zeros for some values of $\Lambda_{\rm qp}$.

For weak coupling, $\Lambda_{\rm qp} \ll 1$, the exponential can be expanded as $1 - i\Lambda_{\rm qp}(\hat{a}+\hat{a}^\dagger)$ and thus only adjacent Fock states are coupled. For strong coupling ($\Lambda_{\rm qp} \approx 1$), higher order elements in the expansion cannot be neglected and hence transitions between $|m\rangle$ and $|m+l\rangle$ states, with $l > 1$, are allowed. Moreover the amplitude of the one photon process becomes dependent on the initial and final state as shown in figure 3.12b.

3.3.2 Cavity-junction master equation

Using the expansion 3.13 and following the standard quantum optics approach based on the Born-Markov and on the secular approximation, we can write the master equation for the resonator density matrix ρ:

$$\frac{d\rho(t)}{dt} = \sum_{l_0,\ldots,l_n=-\infty}^{\infty} -i\epsilon_{l_0,\ldots,l_n}\left[\hat{A}_{l_0,\ldots,l_n}\hat{A}^\dagger_{l_0,\ldots,l_n}, \rho\right] + \gamma_{l_0,\ldots,l_n}\mathcal{L}_{l_0,\ldots,l_n}(\rho), \tag{3.18}$$

with $\mathcal{L}_{l_0,\dots,l_n}(\rho)$ being the Lindblad superoperator:

$$\mathcal{L}_{l_0,\dots,l_n}(\rho) = \hat{A}^{\dagger}_{l_0,\dots,l_n}\rho\hat{A}_{l_0,\dots,l_n} - \frac{1}{2}\Big\{\hat{A}_{l_0,\dots,l_n}\hat{A}^{\dagger}_{l_0,\dots,l_n}, \rho\Big\}. \tag{3.19}$$

From this equation, we see the two main effects arising from the cavity-junction coupling: the first term describes a shift of the energy levels while the second term corresponds to an energy exchange between the cavity and the bath in the form of quantum jumps.

These two effects are function of the frequency shift parameter $\epsilon_{l_0,\dots,l_n}$ and on the jump rate $\gamma_{l_0,\dots,l_n}$ that depend on the dc bias voltage V and are proportional to the imaginary and real part of the one sided Fourier transform of the bath memory function. These are equal to:

$$\epsilon_{l_0,\dots,l_n} = \epsilon\left(\sum_{n=0}^{\infty} l_n\omega_n + \frac{eV}{\hbar}\right) + \epsilon\left(\sum_{n=0}^{\infty} l_n\omega_n - \frac{eV}{\hbar}\right), \tag{3.20}$$

$$\gamma_{l_0,\dots,l_n} = \gamma\left(\sum_{n=0}^{\infty} l_n\omega_n + \frac{eV}{\hbar}\right) + \gamma\left(\sum_{n=0}^{\infty} l_n\omega_n - \frac{eV}{\hbar}\right), \tag{3.21}$$

with ϵ and γ defined as:

$$\epsilon(\omega) = \gamma_0\mathcal{P}\int \frac{n_R(\omega')n_L(\omega'')f(\omega')(1-f(\omega''))}{\omega-\omega'+\omega''}d\omega'd\omega'', \tag{3.22}$$

$$\gamma(\omega) = \pi\gamma_0\int n_R(\omega')n_L(\omega+\omega')f(\omega')(1-f(\omega+\omega'))d\omega'. \tag{3.23}$$

$n_{R,L}(\omega)$ are the density of states on the right and left side of the junctions, $f(\omega)$ is the Fermi Dirac distribution and γ_0 is the coupling between the cavity and the bath, that is defined as $\gamma_0 = (R_K/R_N)/(2\pi)^2$.
The integral that appears in the definition of $\gamma(\omega)$ is equivalent to the one of the dc current-voltage characteristic of equation 3.4 while the shift rate $\epsilon(\omega)$ is proportional to $-I_{KK}(V)$ defined in equation 3.5. In figure 3.13 we show their behavior for different frequencies ω.

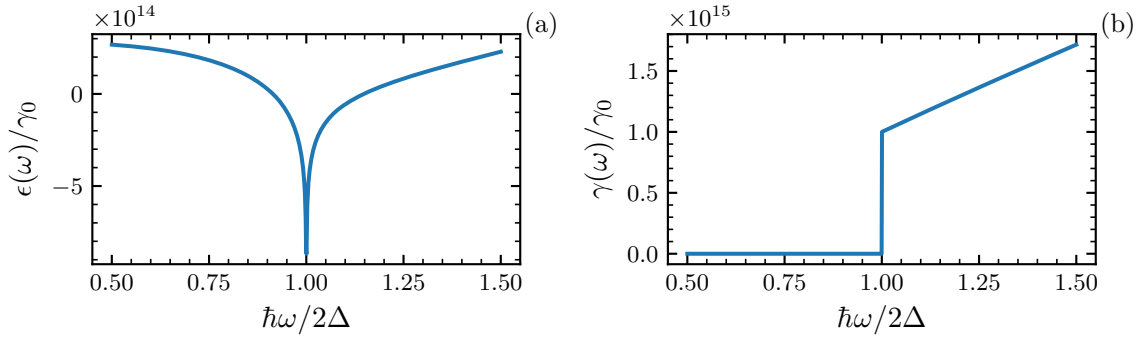

Figure 3.13: (a) Imaginary part $\epsilon(\omega)$ and (b) real part $\gamma(\omega)$ of the Fourier transform of the bath memory function. $\gamma(\omega)$ is linked to the dc current voltage characteristic of the junction while $\epsilon(\omega)$ is proportional to its Kramers-Kronig transform.

The master equation 3.18 is valid when the Born-Markov approximation holds. This happens when the system-bath interaction is sufficiently weak such that the state of the bath

is not affected by the coupling to the cavity, and when the bath correlations function decays quickly compared to the dynamics of the cavity. Moreover, since we treat the bath as a perturbation and we use the secular approximation to neglect the rapidly varying term in the master equation, we require that the coupling to the bath is sufficiently small $\gamma_0 \ll 1$. These conditions are experimentally verified when the transmission of the junction is small enough to keep the two contacts at equilibrium meaning when $R_N \gg R_K$.

3.3.3 Lamb Shift of the energy levels

In this section, we study the properties of the Lamb shift operator and we see how it affects the spectrum of the cavity. We first present the case of a single mode resonator and then discuss how the shift of the levels depends on the bias voltage, on the coupling between the cavity and the junction Λ_{qp} and on the bath coupling term γ_0. In the second part, we generalize the discussion to the case of a multi-mode cavity, mainly focusing on how the presence of the other modes changes the properties of the shift.

Single-mode resonator case

We start by considering the case of a single-mode resonator, with resonant frequency ω_0 and coupling $\Lambda_{0,\text{qp}}$, whose Lamb shift operator is:

$$\hat{H}_{LS} = \sum_{l_0=-\infty}^{\infty} \hbar\epsilon_{l_0} \hat{A}_{l_0}^{(0)} \hat{A}_{l_0}^{(0)\dagger}. \tag{3.24}$$

$\hat{H}_{LS}$ is diagonal in the Fock state basis and causes a variation of the m-th energy levels $\delta\omega_0^m$ that is equal to:

$$\delta\omega_0^m = \sum_{l_0=-\infty}^{\infty} \epsilon_{l_0} \langle m| \hat{A}_{l_0}^{(0)} \hat{A}_{l_0}^{(0)\dagger} |m\rangle = \sum_{l_0=1}^{\infty} \epsilon_{-l_0} |w_{m,l_0}(\Lambda_{0,\text{qp}})|^2 + \sum_{l_0=0}^{m} \epsilon_{l_0} |w_{m-l_0,l_0}(\Lambda_{0,\text{qp}})|^2. \tag{3.25}$$

The eigenfrequencies of the cavity, $\omega_0^m = m\omega_0 + \delta\omega_0^m$, depend therefore on the coupling between the cavity and the junction $\Lambda_{0,\text{qp}}$, through the jump operators $\hat{A}_{l_0}^{(0)}$, and on both the bath coupling term γ_0 and the voltage bias V through the shift rates ϵ_{l_0}.
In the weak coupling regime, we can expand $\delta\omega_0^m$ in powers of $\Lambda_{0,\text{qp}}$ and we get that, at first order, the variation of the transition frequency $\delta\omega_0^{m+1} - \delta\omega_0^m$ is equal to:

$$\delta\omega_0^{m+1} - \delta\omega_0^m = \gamma_0 \Lambda_{0,\text{qp}}^2 (\epsilon_1 + \epsilon_{-1} - 2\epsilon_0) + O(\Lambda_{0,\text{qp}}^2) \tag{3.26}$$

This equation corresponds to a global shift of the frequency of the cavity, since it doesn't depend on the energy level m and it is equivalent to the one obtained with the classical model from equation 3.9. This confirms that, in the weak coupling regime, quantum effects are negligible and we can explain the frequency shift considering only the admittance of the junction. For larger values of $\Lambda_{0,\text{qp}}$, one has to consider higher terms in the expansion:

$$\begin{aligned}\delta\omega_0^{m+1} - \delta\omega_0^m = {} & \gamma_0 \Lambda_{0,\text{qp}}^2 (\epsilon_1 + \epsilon_{-1} - 2\epsilon_0) + \\ & + \gamma_0 \frac{\Lambda_{0,\text{qp}}^4}{4} [(m\epsilon_2 + (m+2)\epsilon_{-2} - (4m+2)\epsilon_1 + (6m+6)\epsilon_0] + O(\Lambda_{0,\text{qp}}^4)\end{aligned} \tag{3.27}$$

With the second term, we see that different states shift differently. The spectrum becomes nonlinear and the anharmonicity depends on V through the voltage dependence of ϵ_l. For $\Lambda_{0,\mathrm{qp}} \approx 1$, the first two terms of the series are not sufficient to describe the energy level shift and we compute equation 3.25 numerically. In figure 3.14 we report the normalized variation of the transition frequencies ($\omega_0^{m+1,m} = \omega_0^{m+1} - \omega_0^m = \omega_0 + \delta\omega_0^{m+1} - \delta\omega_0^m$) for the first three energy levels of the cavity as function of the voltage bias, for $\Lambda_{0,\mathrm{qp}} = 1$ and $\gamma_0 = 3 \times 10^{-3}$ For this calculation, the sum of 3.25 is truncated after the first 40 terms.

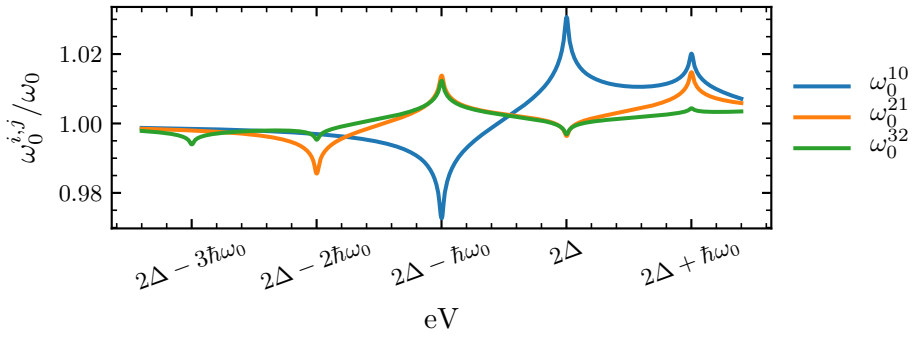

Figure 3.14: Transition frequencies for the first four energy levels of the cavity as a function of the bias voltage V with $\Lambda_{0,\mathrm{qp}} = 1$ and the bath coupling rate $\gamma_0 = 3 \times 10^{-3}$.

We recover that the transition rate, $\omega_0^{m+1,m}$ are strongly shifted, presenting a dip or a peak, when the bias voltage is $eV = 2\Delta \pm l_0\hbar\omega_0$. The amplitude of the shift is different for every energy level, depending on the values of $\Lambda_{0,\mathrm{qp}}$ and γ_0. In fig. 3.15a we show the transition frequency ω_0^{10} at different voltage bias V for several values of $\Lambda_{0,\mathrm{qp}}$ with $\gamma_0 = 3 \times 10^{-3}$. Figure 3.15b instead shows the amplitude of the dip of the transition ω_0^{10}, calculated at $eV = 2\Delta - \hbar\omega_0$, for different values of $\Lambda_{0,\mathrm{qp}}$ and γ_0.

Multi-mode cavity case

We now generalize the previous discussion to a multi-mode cavity and we study how the presence of extra modes affects the Lamb shift of the energy levels of a single mode. The Lamb shift operator, in this case, has the form:

$$\hat{H}_{LS} = \sum_{l_0,\ldots,l_n=-\infty}^{\infty} \hbar\epsilon_{l_0,\ldots,l_n} \hat{A}_{l_0,\ldots,l_n} \hat{A}^\dagger_{l_0,\ldots,l_n} \tag{3.28}$$

In order to compute the variation of the spectrum for a single mode, here the first, we make the assumption that the cavity density matrix ρ can be written as tensor product of density matrices:

$$\rho(t) = \rho^{(0)}(t) \otimes \rho^{(1)}(t) \otimes \cdots \otimes \rho^{(n)}(t), \tag{3.29}$$

where $\rho^{(n)}(t)$ refers to the n-th mode density matrix. Since in the experiment, we are interested in studying the dynamics of the $n = 1$ mode, we compute the spectrum by taking the partial trace, over the other modes. This gives:

$$\mathrm{Tr}\left(\hat{A}_{l_0,\ldots,l_n} \hat{A}^\dagger_{l_0,\ldots,l_n} \rho\right) = \hat{A}^{(1)}_{l_1} \hat{A}^{(1)\dagger}_{l_1} \rho^{(1)} \mathrm{Tr}\left(\hat{A}_{l_0,l_2,\ldots,l_n} \hat{A}^\dagger_{l_0,l_2,\ldots,l_n} \rho^{(0,2\ldots,n)}\right). \tag{3.30}$$

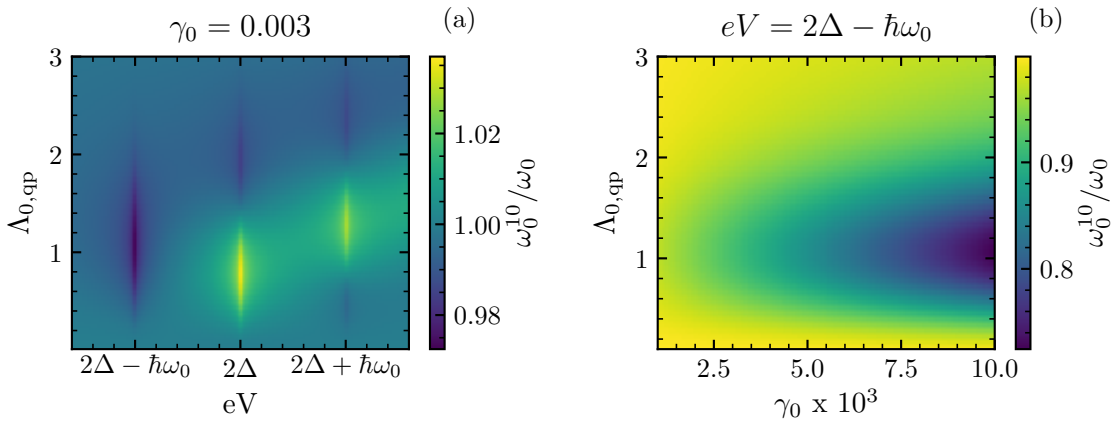

Figure 3.15: Amplitude of the transition frequency ω_0^{10} for different V, $\Lambda_{0,\mathrm{qp}}$ and γ_0. Figure (a) shows the variation of ω_0^{10} for $\gamma_0 = 3 \times 10^{-3}$ for different voltages and coupling. The position of the dips and of the peaks remains unchanged ($eV = 2\Delta \pm l_0\hbar\omega_0$) but their amplitude depends on the matrix elements $\langle m| \hat{A}_{l_0}^{(0)} \hat{A}_{l_0}^{(0)\dagger} |m\rangle$ (with $m = 1, 0$), that is a function of $\Lambda_{0,\mathrm{qp}}$. Figure (b) shows the same transition amplitude at $eV = 2\Delta - l_0\hbar\omega_0$ for different $\Lambda_{0,\mathrm{qp}}$ and γ_0.

At this point, we can make some assumption about the population of the spectator modes and see how the energy levels shift depends on that. In particular, we focus on two cases: when the spectator modes are all vacuum and when they are thermally populated.

Spectator modes in vacuum

If we assume that all the spectator modes are in vacuum, we can rewrite the right hand side of equation 3.30 as:

$$\mathrm{Tr}\left(\hat{A}_{l_0,l_2,\ldots,l_n} \hat{A}^{\dagger}_{l_0,l_2,\ldots,l_n} \rho^{(0,2\ldots,n)}\right) = \prod_{n\neq 1} \mathrm{Tr}\left[\hat{A}_{l_n}^{(n)} \hat{A}_{l_n}^{(n)\dagger} |0\rangle \langle 0|\right] = \prod_{n\neq 1} W_{l_n}^{(n)}, \tag{3.31}$$

with:

$$W_{l_n}^{(n)} = \langle 0| \hat{A}_{l_n}^{(n)} \hat{A}_{l_n}^{(n)\dagger} |0\rangle = \begin{cases} 0 & \text{if } l_n > 0 \\ |w_{0,l_n}(\Lambda_{n,\mathrm{qp}})|^2 & \text{if } l_n \leq 0 \end{cases} \tag{3.32}$$

$\hat{H}_{LS}$ can, thus, be rewritten as:

$$\hat{H}_{LS} = \sum_{l_0,\ldots,l_n=-\infty}^{\infty} \hbar\epsilon_{l_0,\ldots,l_n} W_{l_0}^{(0)} W_{l_2}^{(2)} \ldots W_{l_n}^{(n)} \hat{A}_{l_1}^{(1)} \hat{A}_{l_1}^{(1)\dagger} \tag{3.33}$$

Since the $W_{l_n}^{(n)}$ contribute to the sum only when $l_n \leq 0$ we can rewrite the previous equation as:

$$\hat{H}_{LS} = \sum_{l_1=-\infty}^{\infty} \left(\hbar\tilde{\epsilon}_{l_1} + \sum_{l_0,l_2,\ldots,l_n=-\infty}^{-1} \hbar\epsilon_{l_0,l_2\ldots,l_n} W_{l_0}^{(0)} W_{l_2}^{(2)} \ldots W_{l_n}^{(n)} \right) \hat{A}_{l_1}^{(1)} \hat{A}_{l_1}^{(1)\dagger} \tag{3.34}$$

The first term of the equation corresponds to an effective shift rate given by:

$$\tilde{\epsilon}_{l_1} = \epsilon_{l_1} W_0^{(0)} W_0^{(2)} \dots W_0^{(n)} = \epsilon_{l_1} \prod_{n \neq 1} e^{-\Lambda^2_{n,\mathrm{qp}}}, \tag{3.35}$$

while the second term causes the appearance of more dips and peaks. Since these are located at voltages $V > 2\Delta/e - m\hbar\omega_0/e$, which is the voltage region where the intrinsic losses of the m-th level increase, we are not able to measure them.

Using the hamiltonian of equation 3.34 we can compute the transition frequencies of the mode $n = 1$ as:

$$\omega_1^{m+1,m} = \omega_1 + \delta\omega_1^{m+1} - \delta\omega_1^m = \omega_1 + \langle m+1| \hat{H}_{LS} |m+1\rangle - \langle m| \hat{H}_{LS} |m\rangle . \tag{3.36}$$

In figure 3.16 we show the variation of the first two energy levels, in the case of a two modes cavity with the mode $n = 1$ assumed to be in vacuum (in this simulation $\omega_0 > \omega_1$). The parameters used for the simulation are: $\Lambda_{0,\mathrm{qp}} = 0.5$, $\Lambda_{1,\mathrm{qp}} = 1$ and $\gamma_0 = 0.3$. We compare the results to the case of a resonator where only the mode $n = 0$ is present.

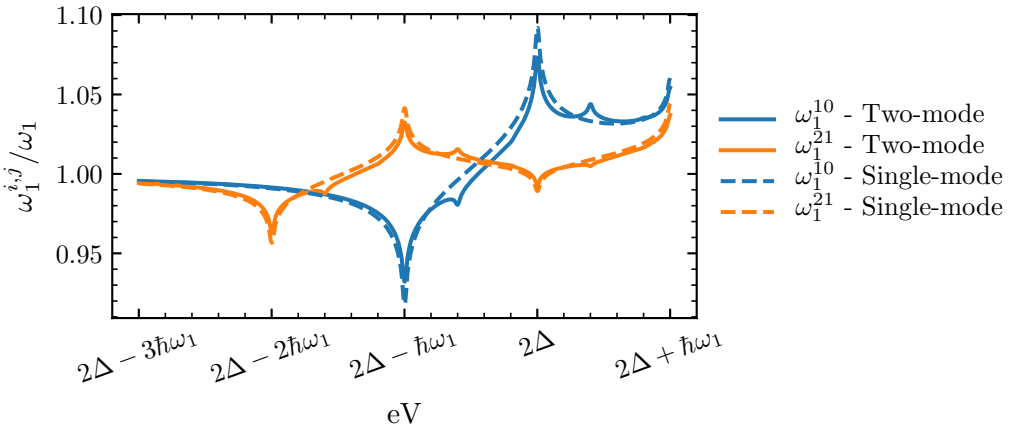

Figure 3.16: Simulation of the Lamb shift of the first two energy levels of the $n = 1$ mode for a two mode cavity, with $\Lambda_{0,\mathrm{qp}} = 0.5$, $\Lambda_{1,\mathrm{qp}} = 1$ and $\gamma_0 = 0.3$. The first is assumed to be in vacuum. For comparison we also plot the results obtained for a resonator where only the mode $n = 1$ is present.

Spectator modes thermally populated

In this section we assume that there is only one spectator mode and that is thermally populated and we study how this affects the Lamb shift of the cavity energy levels. We consider the case of a two mode cavity and we use the same parameters as before for the calculation of the transition frequencies. If we assume that the population of the $n = 0$ mode is given by $\rho_{\mathrm{th}}^{(0)}$, the Lamb Shift operator becomes:

$$\hat{H}_{LS} = \sum_{l_0, l_1 = -\infty}^{\infty} \hbar\epsilon_{l_0,l_1} \hat{A}_{l_1}^{(1)} \hat{A}_{l_1}^{(1)\dagger} \mathrm{Tr}\left[\hat{A}_{l_0}^{(0)} \hat{A}_{l_0}^{(0)\dagger} \rho_{\mathrm{th}}^{(0)}\right]. \tag{3.37}$$

Plugging this hamiltonian into eq. 3.36 we can compute the frequency ω_1^{10} that we show in figure 3.17 for different number of thermal photons in the $n = 0$ mode.

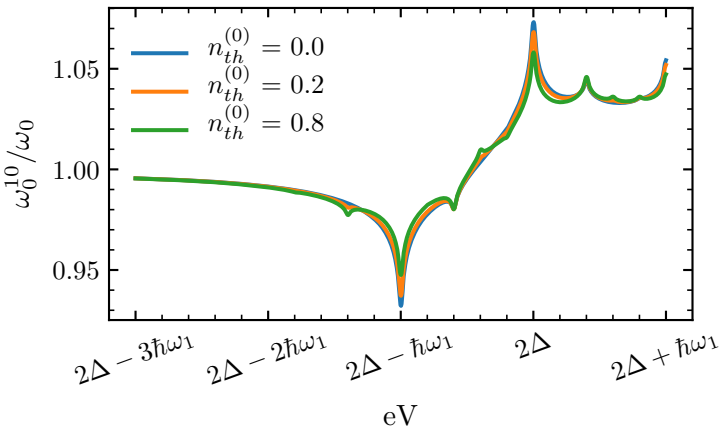

Figure 3.17: Lamb shift of the transition frequency ω_1^{10} for different thermal population of the $n = 0$ mode. As the number of thermal photons increases more dips located $2\Delta/e - \hbar\omega_1 \pm l\hbar\omega_0$ start to appear

As the number of thermal photons increases, the amplitude of the dip located at $2\Delta/e - \hbar\omega_1$ decreases and more dips located at $2\Delta/e - \hbar\omega_1 \pm l\hbar\omega_0$, with l positive integer, appear. Since we do not measure any of these extra dips in our experiment, we assume that the number of thermal photons in the spectator mode is negligible.

3.3.4 Photon exchange between the cavity and the junction

We have seen from the master equation 3.18 that the cavity experiences an irreversible exchange of photons with the junction itself. Since the matrix elements of the jump operators, $w_{m,l}(\Lambda)$, are Fock state dependent, the rate at which photons are exchanged depends on the Fock state of the cavity. This rate is also a function of the jump rate $\gamma_{l_0,\dots,l_n}$, which we have seen to be equal to zero if $V < \sum_{n=0}^{\infty} l_n\hbar\omega_n/e$ and different from zero for higher voltages.

In figure 3.18 we plot the photon loss rate $\gamma_{l_0}|w_{0,l_0}|^2$ as a function of the voltage, for a single mode cavity with $\Lambda_{0,\mathrm{qp}} = 1$ and $\gamma_0 = 3 \times 10^{-3}$. These are the processes that couple the excited states of the cavity to the ground state. For voltages below the superconducting gap, only processes where photons are absorbed by the junction are allowed. At the same time, when $eV > 2\Delta$, opposite processes are allowed and the junction emits photons in the cavity.

Multi-mode cavity

The presence of the spectator modes also affects the rate at which photons are exchanged with the junction. We perform the same calculation as before and compute the partial trace over the spectator modes that appear in the Lindblad superoperator $\mathcal{L}_{l_0,\dots,l_n}(\rho)$. In the case the mode under study is the $n = 1$, this becomes:

$$\mathrm{Tr}\left(\hat{A}^{\dagger}_{l_0,\dots,l_n}\rho\hat{A}_{l_0,\dots,l_n}\right) = \hat{A}^{(1)\dagger}_{l_1}\rho^{(1)}\hat{A}^{(1)}_{l_1}\mathrm{Tr}\left(\hat{A}^{\dagger}_{l_0,l_2,\dots,l_n}\rho^{(0,2,\dots,n)}\hat{A}_{l_0,l_2,\dots,l_n}\right). \tag{3.38}$$

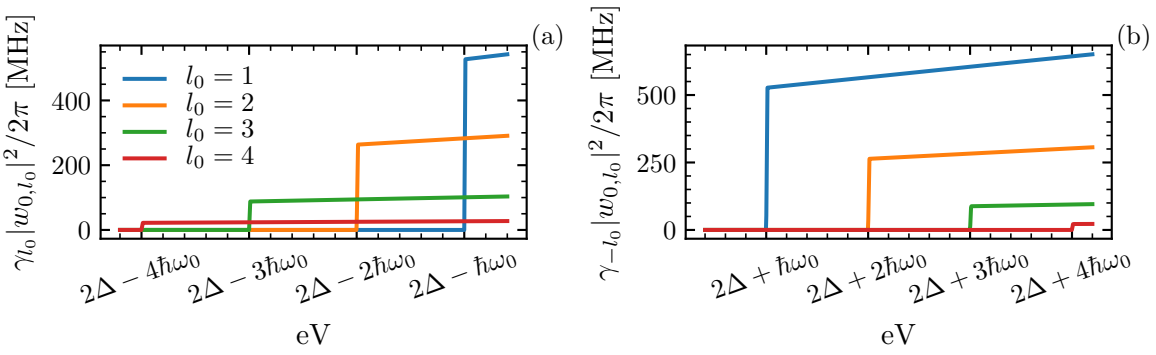

Figure 3.18: Photon exchange rate between the cavity and the junction. (a) Processes allowed for positive l_0 that corresponds to the annihilation of photons in the cavity, absorbed by the junction. (b) Processes with negative l_0 instead refer to creation of photons in the cavity and are allowed only for voltages above the gap.

If we assume that the spectator modes are in vacuum the right hand side term of equation 3.38 becomes equal to

$$\mathrm{Tr}\left(\hat{A}^{\dagger}_{l_0,l_2,\ldots,l_n}\rho^{(0,2,\ldots,n)}\hat{A}_{l_0,l_2\ldots,l_n}\right) = \prod_{n=1} W^{(n)}_{l_n}, \tag{3.39}$$

with the $W^{(n)}_{l_n}$ defined in equation 3.32. The Lindblad superoperator can be rewritten as:

$$\mathcal{L}_{l_0,\ldots,l_n}(\rho) = \sum_{l_1=-\infty}^{\infty}\left(\tilde{\gamma}_{l_1} + \sum_{l_0,l_2,\ldots l_n=-\infty}^{-1}\gamma_{l_0,l_2\ldots,l_n}W^{(0)}_{l_0}W^{(2)}_{l_2}\ldots W^{(n)}_{l_n}\right)\mathcal{L}^{(1)}_{l_1}(\rho), \tag{3.40}$$

with:

$$\mathcal{L}^{(1)}_{l_1}(\rho) = \hat{A}^{(1)\dagger}_{l_1}\rho\hat{A}^{(1)}_{l_1} - \frac{1}{2}\left\{\hat{A}^{(1)}_{l_1}\hat{A}^{(1)\dagger}_{l_1},\rho\right\}, \tag{3.41}$$

and:

$$\tilde{\gamma}_{l_1} = \gamma_{l_1}W^{(1)}_1\ldots W^{(n)}_1 = \gamma_{l_1}\prod_{n\neq 1}e^{-\Lambda^2_{n,\mathrm{qp}}}, \tag{3.42}$$

Again we recover that the jump rate is reduced by an exponential factor that depends on the coupling $\Lambda_{n,\mathrm{qp}}$ of the spectator modes in vacuum.

3.4 Cavity mode spectroscopy and Lamb shift results

In this paragraph, we compare the model discussed in the previous section with the Lamb shift data obtained from the cavity spectroscopy. We start discussing the validity of the single-mode and two-mode cavity approximation, which consists in using the Lamb shift calculated for a single-mode resonator or for a two-mode cavity with the second mode in vacuum. We show that $\Lambda_{n,\mathrm{qp}}$ and 2Δ can be reliably estimated from our data. We discuss the effect of voltage noise on the biasing line and we show that it can lead to a reduction of the coupling $\Lambda_{n,\mathrm{qp}}$ up to 5 %. In the final part we measure the photo-assisted current at different voltages and for frequencies up to $2\pi \times 25$ GHz. This allows us to precisely measure

the resonant frequencies of the first five modes and reconstruct the spectrum of the cavity. We use these results to adjust the electromagnetic simulations of the sample and to estimate the capacitance of the junction.

3.4.1 Single-mode and two-mode cavity approximation

In the previous section, we have shown that the Lamb shift of the energy levels depends not only on the cavity-junction coupling $\Lambda_{n,\mathrm{qp}}$ of the mode in analysis but also on the ones of the spectator modes. Equation 3.34 shows that in the multi-mode case (with the assumption that the spectator modes are in vacuum) the frequency shift is given by the sum of the re-normalized single mode rate $\epsilon_{l_0} \prod_n e^{-\Lambda^2_{n,\mathrm{qp}}}$ and of the matrix element products $W^{(1)}_{l_1} \dots W^{(n)}_{l_n}$. Because we cannot have a direct measurement of $\Lambda_{n,\mathrm{qp}}$ and we cannot calculate the total shift rate, it is useful to evaluate the error we do, in the estimation of $\Lambda_{1,\mathrm{qp}}$, when we approximate the Lamb shift given by a multi-mode cavity with the one obtained from a single-mode or two-mode cavity. We do so by simulating ω_1^{10} and $\omega_1^{20}/2$ in the case of a multi-mode cavity (equation 3.34), assuming all the spectator modes in vacuum, and by fitting the results using equation 3.25, that applies in the case of a single-mode cavity, and with equation 3.34, but assuming the presence of only one spectator mode ($n = 0$) in vacuum. This estimation slightly depends on the voltage range that we consider for the fit. In this case, we use the same as in the experiment with the voltage for ω_1^{10} being between 300 µV and 370 µV (figure 3.4) and the one for $\omega_1^{20}/2$ between 340 µV and 344 µV (figure 3.5).

The parameters used for the simulation are reported in the table 3.1 and are the ones obtained from Sonnet, with an expected $C_J = 2\,\mathrm{fF}$, as discussed in chapter 1.3. The only exception is the ω_1 frequency that has been replaced with the measured one. The measured normal resistance of the junction is 220 kΩ (appendix B), leading to $\gamma_0 = 2.9 \times 10^{-3}$ while $2\Delta = 400\,\mu\mathrm{eV}$.

	$\omega_n/2\pi$ [GHz]	$\Lambda_{n,\mathrm{qp}}$
n = 0	1.73	0.65
n = 1	5.91	0.75
n = 3	14.03	0.46
n = 5	23.68	0.36
n = 7	31.88	0.30

Table 3.1: Parameters used for the simulation of the transition frequencies shift. The values are the ones obtained from Sonnet simulations, assuming $C_J = 2\,\mathrm{fF}$, with the exception of the ω_1 frequency that has been replaced with the measured value.

For the single-mode approximation, the fit is performed leaving $\Lambda_{1,\mathrm{qp}}$, γ_0 and Δ as free parameters while in the two-modes case, $\Lambda_{0,\mathrm{qp}}$ is a fit parameter too. Since the amplitude of the shifts depends both on $\Lambda_{n,\mathrm{qp}}$ and γ_0 we fit ω_1^{10} and $\omega_1^{20}/2$ simultaneously. A plot of the simulated values, together with the two fits, is shown in figure 3.19. In both cases the fit agrees quite well with the simulated data.

From the single-mode approximation, we get $\Lambda_{1,\mathrm{qp}} = 0.77$, $2\Delta = 403\,\mu\mathrm{eV}$ and $\gamma_0 = 2.15 \times 10^{-3}$. The values of $\Lambda_{1,\mathrm{qp}}$ and 2Δ, obtained from the fit, differ only of few percent from the values used in the simulation, while, as expected, the value γ_0, that gives the frequency shift rate, is different from the expected one. It is interesting to note that this

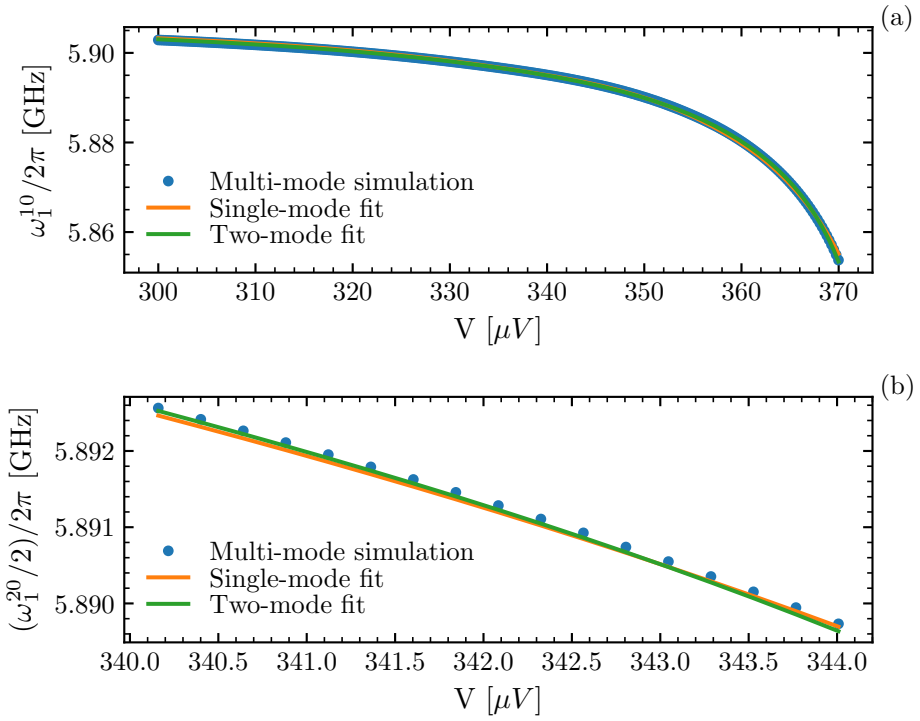

Figure 3.19: Comparison between the simulated Lamb shift of the first two energy level for the multi-mode cavity case and the single-mode and two-mode fit.

difference is not only due to the re-normalization factor $\prod_n e^{-\Lambda^2_{n,\mathrm{qp}}}$ but also to the second term of equation 3.34 that cannot be neglected.

From the two-mode fit,, we get $\Lambda_{1,\mathrm{qp}} = 0.75$, $\Lambda_{0,\mathrm{qp}} = 1.23$, $2\Delta = 398\,\mu\mathrm{eV}$ and $\gamma_0 = 2.4 \times 10^{-3}$. The coupling $\Lambda_{1,\mathrm{qp}}$ corresponds to the one used in the simulation while the one of the spectator mode $\Lambda_{0,\mathrm{qp}}$ is completely different. Once again, γ_0 is smaller than expected.

In conclusion, by using a single-mode and a two-mode cavity approximation we can get quite precisely the value of the coupling of the mode under study and the energy of the superconducting gap. However the estimation of γ_0 and of the coupling of the spectator mode (in the two-mode approximation) is not reliable.

3.4.2 Fit of the Lamb shift - single tone spectroscopy

In this paragraph, we show the fit of the transition frequencies of the energy levels of the cavity that we measured with the single tone spectroscopy as discussed in section 3.1.

Single-mode approximation

We start by modeling the shift of the frequency using the single-mode cavity approximation. We use equation 3.36 with $\hat{H}_{LS}$ being the single-mode cavity hamiltonian 3.24 and ω_1 the resonant frequency of the cavity kept fixed and equal to $2\pi \times 5.912\,\mathrm{GHz}$ As done in the previous paragraph, to extract all the parameters of the system we fit simultaneously the transition frequencies ω_1^{10} and $\omega_1^{20}/2$. The first is the one reported in figure 3.4b, while the latter is extracted taking the frequency of the minimum of $|S_{11}|^2$ from the data shown in figure 3.5d. We also leave as a free parameter of the fit the gap energy Δ. A plot of the data together with their fit is shown in figure 3.20.

The results of the fit depend also on the value of the low temperature resistance in the voltage divider that we use to bias the junction. The voltage across the junction is given by the voltage set by the room temperature source multiplied by the ratio between the resistances of the voltage divider: $110\,\Omega/1\,\mathrm{M}\Omega$. As discussed in 2.3.3, the $1\,\mathrm{M}\Omega$ resistor is at room temperature while the $110\,\Omega$ is fixed on the 10 mK stage of the fridge. Since we cannot directly measure its value at 10 mK, we have to assume that its resistance may be different from the room temperature one. Measurements of the Josephson emission peaks (see section 4.1) show, however, that it remains very close to $110\,\Omega$ and therefore we assume that it is equal to $(110 \pm 1)\,\Omega$.

We repeat the fit of the Lamb shift for three values of resistance in that range (respectively $109\,\Omega$, $110\,\Omega$ and $111\,\Omega$) and we take as final results the mean value of the three results with an uncertainty given by the standard deviation of the values. The parameters obtained are the following: $\Lambda_{1,\mathrm{qp}} = 0.76 \pm 0.01$, $\gamma_0 = (2.28 \pm 0.04) \times 10^{-3}$ and $2\Delta = (398 \pm 3)\,\mu\mathrm{eV}$.

Two-mode approximation

We now use equation 3.36 with hamiltonian 3.34, and assume that the $n = 0$ mode, at frequency $2\pi \times 1.9\,\mathrm{GHz}$ is in vacuum. This value of frequency is obtained from the measurement of the photo-assisted current and will be better discussed in paragraph 3.4.6. We repeat the same procedure discussed before and add as free parameter the coupling $\Lambda_{0,\mathrm{qp}}$. The results of the fit, shown in figure 3.21, are: $\Lambda_{1,\mathrm{qp}} = 0.75 \pm 0.01$, $\Lambda_{0,\mathrm{qp}} = 0.350 \pm 0.003$, $\gamma_0 = (2.37 \pm 0.05) \times 10^{-3}$ and $2\Delta = (397 \pm 3)\,\mu\mathrm{V}$.

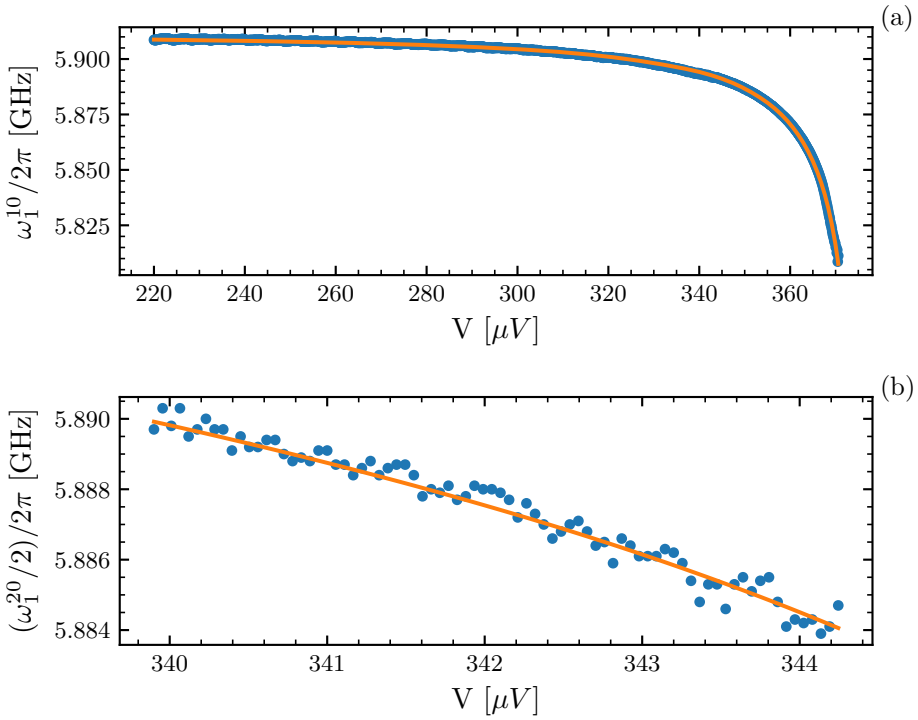

Figure 3.20: Fit of the transition frequencies (a) ω_1^{10} and (b) ω_1^{20} performed with a single-mode cavity approximation. The data were obtained performing a single tone spectroscopy and are discussed in section 3.1. In orange we show the curve obtained fitting the two sets of data of data simultaneously with the single-mode cavity approximation. The results of the fit are: $\Lambda_{1,\mathrm{qp}} = 0.76 \pm 0.01$, $\gamma_0 = (2.28 \pm 0.04) \times 10^{-3}$ and $2\Delta = (398 \pm 3)\,\mu\mathrm{V}$.

As expected from the simulations done in 3.4.1, the value of $\Lambda_{1,\mathrm{qp}}$ obtained with a two-mode model is very close to the one obtained with the single-mode model. The value of the coupling of the $n = 0$ mode is almost two times smaller than the one expected from the simulations of the sample. However, as shown in 3.4.1, we do not expect a reliable estimation from the fit. In both cases, γ_0 is smaller than the value given by the normal resistance.

3.4.3 Fit of the Lamb shift - two tone spectroscopy

Using the parameters derived from the fit of ω_1^{10} and ω_1^{20}, we can compare the expected transition frequency ω_1^{21} with the one obtained performing a two tone spectroscopy measurement that we discussed in section 3.1.2. In figure 3.22, we plot the expected curve obtained from equation 3.36, in the single-mode case, and the data measured with a two tone pump (figure 3.8a). There is a good agreement between the two curves with the exception of the points in the voltage range between 325 µV and 340 µV. We can explain this discrepancy by considering also the transition frequency $\omega_1^{20}/2$ also shown (in green) in the figure.

When the two frequencies are close ($V < 340\,\mu\mathrm{V}$) a two photon absorption process also probes the $\omega_1^{20}/2$ transition. As the difference between the two transitions becomes bigger than the linewidth of the cavity (which at this voltage is around $2\pi \times 5\,\mathrm{MHz}$), we are able to distinguish the two processes.

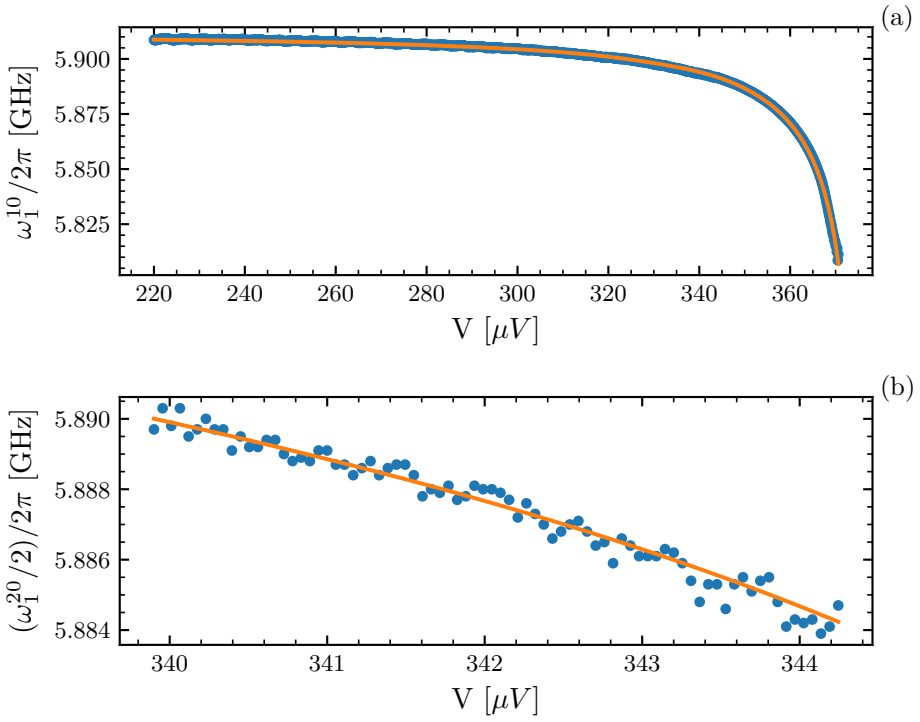

Figure 3.21: Fit of the transition frequencies (a) ω_1^{10} and (b) ω_1^{20}. The fit is performed assuming the presence of one spectator mode in vacuum. The results of the fit are: $\Lambda_{1,\mathrm{qp}} = 0.75 \pm 0.01$, $\Lambda_{0,\mathrm{qp}} = 0.350 \pm 0.003$, $\gamma_0 = (2.37 \pm 0.05) \times 10^{-3}$ and $2\Delta = (397 \pm 3)\,\mu\mathrm{V}$.

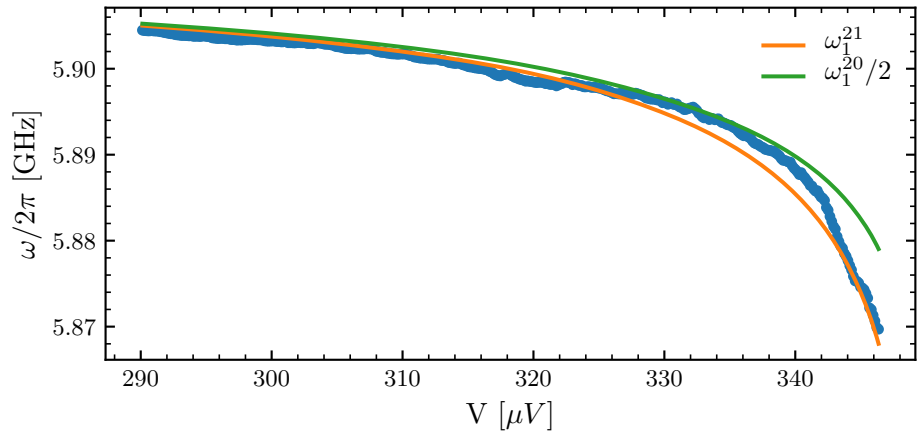

Figure 3.22: Comparison between the transition frequency measured with two tone spectroscopy and the ω_1^{21} and $\omega_1^{20}/2$ expected curve. When the two frequencies are close ($V < 340\,\mu\mathrm{V}$) the experimental data are better described by the green curve. For voltages bigger than $340\,\mu\mathrm{V}$, where the difference between the two transition frequencies is larger than the linewidth of the cavity, the data coincide with the expected ω_1^{21} curve.

3.4.4 Voltage noise effect

Up to this point, we have neglected the voltage noise present on the biasing line and its effect on the Lamb shift. We now take it into account by considering gaussian noise of different variance that we apply in the calculation of the transition frequencies. In figure 3.23 we plot ω_1^{10}, for different values of σ_V, in a bigger voltage range than the one of the measurement. We do so to underline that the biggest effect of the voltage fluctuations on the Lamb shift are visible when $eV = 2\Delta - l\hbar\omega_1$ with the dip of the shift that becomes smoother as σ_V increases. The parameters used for the simulations are the ones obtained from the fit of section 3.4.2.

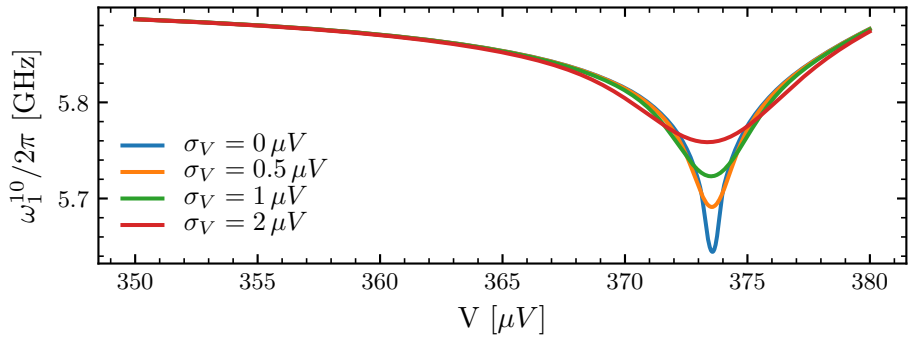

Figure 3.23: Transition frequency ω_1^{10} calculated with different standard deviation σ_V for the voltage noise fluctuations. The effect of the noise is to smooth the dip of the frequency shift.

To calculate the effect of the noise on the fit we assume different voltage fluctuations amplitude and we repeat the fit procedure described in 3.4.2, for the single-mode case. In figure 3.24 we show the variation of the parameters of the fit for different values of σ_V. From this measurement alone we cannot estimate the magnitude of the voltage noise but we can only get an upper boundary which is set from the convergence of the fit that is obtained only for values of $\sigma_V < 3\,\mu V$. From the measurement of the Josephson spectrum, however, we estimate σ_V to be around $0.8\,\mu V$ (section 4.2).

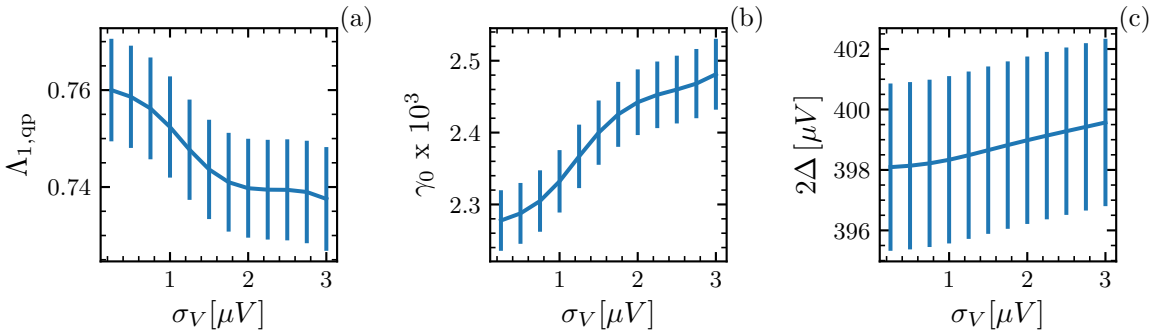

Figure 3.24: Variation of (a) $\Lambda_{1,qp}$, (b) γ_0 and (c) 2Δ for different values of σ_V. The parameters are extracted from the simultaneous fit of ω_1^{10} and ω_1^{20}.

3.4.5 Two-mode spectroscopy

In this section we show qualitatively how the Lamb shift depends on the population of the spectator modes. We have seen from equation 3.30 and equation 3.34 that the presence of spectator modes leads to a re-normalization of the frequency shift rate $\epsilon_{l_0,\ldots,l_n}$ that depends on the population of these modes. Here, we show the Lamb shift of the $n = 1$ mode obtained while pumping the mode at $2\pi \times 1.9\,\mathrm{GHz}$.

We start by performing a two tone measurement: we record the spectrum of the $n = 1$ mode, when the junction is biased at $358\,\mu\mathrm{V}$, while pumping the $n = 0$ mode with different amplitudes V_{RF}. Because the microwave setup we use is not optimized for low frequency measurement (the bandwidth of the circulators is 4 GHz - 8 GHz), we are not able to precisely estimate the microwave power injected in the 0-th mode. However, when the amplitude V_{RF} is sufficiently high, the resonant frequency of the $n = 1$ mode experiences a shift of approximately 10 MHz (figure 3.25). When V_{RF} is too high, the resonance of the $n = 1$ mode disappears.

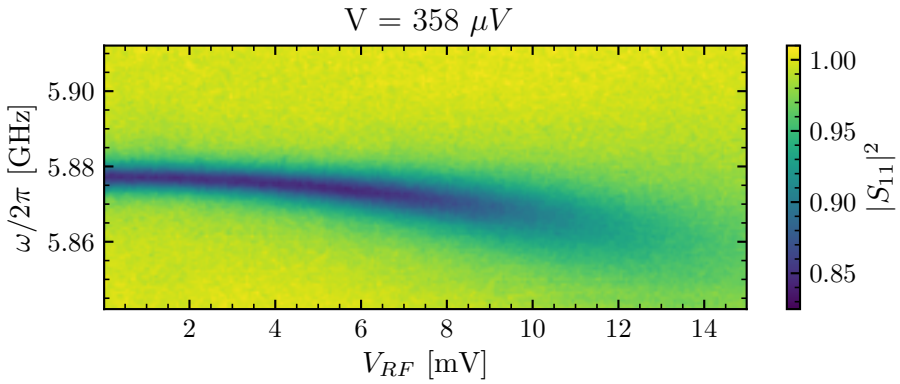

Figure 3.25: Variation of the resonant frequency of the $n = 1$ mode as function of the amplitude of the signal used to pump the $n = 0$ mode. Because of the change of the population the spectator mode, the frequency of the mode under study experiences a negative shift.

To quantify the variation of the frequency shift rate and hence of γ_0, we measure the Lamb shift of the $n = 1$ mode as function of the junction voltage bias, when $V_{RF} = 7\,\mathrm{mV}$. In figure 3.26a, we show the measured spectrum of the $n = 1$ mode while in figure 3.26b, we plot the extracted resonant frequency together with the fit done using the single mode approximation. The only free parameter of the fit is the cavity-bath coupling γ_0, while Λ_1 and 2Δ are fixed to the values of 0.76 and $398\,\mu\mathrm{V}$ derived in 3.4.2. The result we get is $\gamma_0 = (2.65 \pm 0.04) \times 10^{-3}$. As expected this value is different from the one before ($\gamma_0 = (2.28 \pm 0.04) \times 10^{-3}$) showing the effect of the population in the spectator mode.

3.4.6 Photo-assisted current measurement

In order to obtain the spectrum of the cavity at higher frequencies, we measured the photo-assisted current at different voltages and frequencies. To measure the current flowing through the junction, we used the DC setup B (2.3.3), while to excite the cavity with high frequency microwave signal, we connected the sample directly to the bias-tee without using any circula-

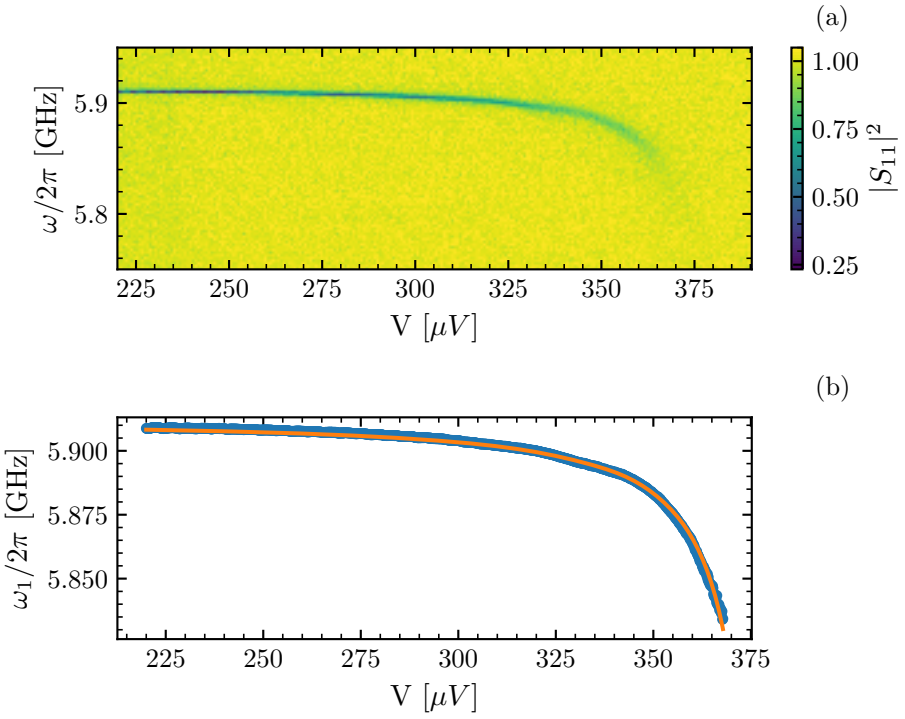

Figure 3.26: (a) Spectrum of the $n = 1$ mode obtained while pumping the $n = 0$ mode with a microwave signal of 7 mV amplitude. (b) Extracted resonant frequency of the mode together with the Lamb shift fit. From the fit we get a value of γ_0 equal to $(2.65 \pm 0.04) \times 10^{-3}$, which is 15 % higher than the value obtained without pumping.

tor. This allowed us to probe the cavity with microwaves with frequencies up to 25 GHz (the bandwidth of the bias tee). We pulse the amplitude of the injected RF signal and, using a lock-in amplifier, we measure the variation of the current over a modulation period. In figure 3.27, we show the variation of photo-assisted current (in arbitrary units) at frequencies near the first five modes of the cavity and for voltages close to the superconducting gap $2\Delta/e$.

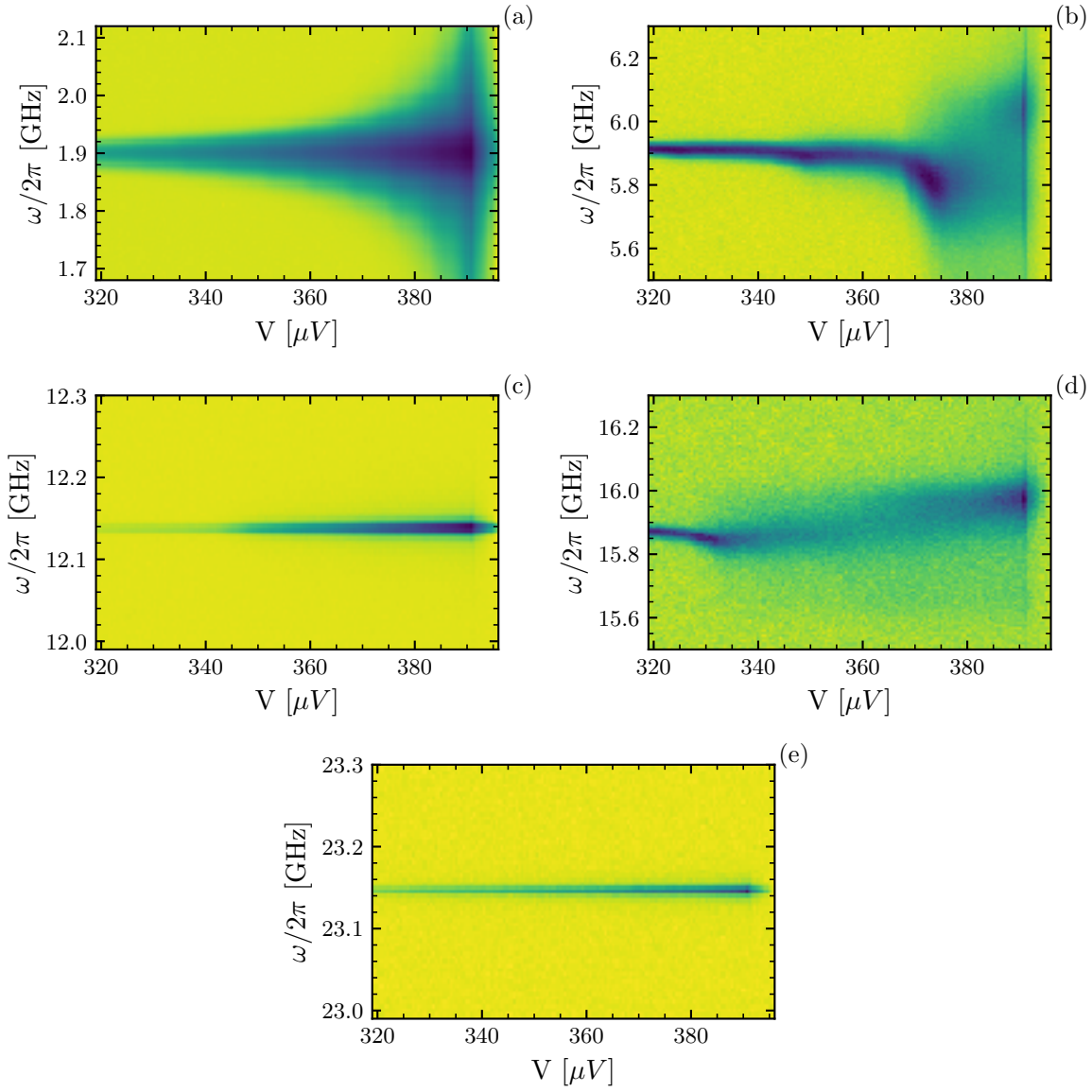

Figure 3.27: Variation of the photo-assisted current for different frequency at voltages close to $2\Delta/e$. The variation of the current, due to a modulation of the rf amplitude, allow us to measure the spectrum of the cavity at higher frequency and to distinguish the high impedance modes from the low impedance ones.

This measurement allows us to get the resonant frequency of the first five modes, which we report in table 3.2, and also to distinguish the strongly coupled modes from the weakly coupled ones. As expected the $n = 0$ (fig. 3.27a), $n = 1$ (fig. 3.27b) and $n = 3$ (fig. 3.27d) modes are high impedance modes, whose properties strongly depends on the voltage bias of

the junction. In particular, for the $n = 1$ and $n = 3$ modes, we observe a Lamb shift and the increase of loss for voltages with $eV > 2\Delta - \hbar\omega_n$. The $n = 2$ (fig. 3.27c) and $n = 4$ (fig. 3.27e) modes, being weakly coupled to the junction, have a constant resonant frequency and do not depend on the bias voltage up to $2\Delta/e$.

	n = 0	n = 1	n = 2	n = 3	n = 4
$\omega_n/2\pi$ [GHz]	1.9	5.91	12.13	15.87	23.14

Table 3.2: Resonant frequency of the first five modes, obtained measuring the variation of the photo-assisted current

3.4.7 Sonnet simulations adjustment and junction capacitance

In this paragraph, we compare the results discussed in the previous section with the ones obtained from the Sonnet simulations of the sample (chapter 1.4) and we use them to estimate the capacitance of the junction. The resonant frequency of the modes obtained from Sonnet differs from the one measured with the photo-assisted current. This discrepancy can be addressed to an incorrect estimation of the capacitance of the junction or to some inaccuracies in the electromagnetic simulations of the circuit. To distinguish these two different contributions we use the weakly coupled modes, whose resonant frequency, as shown in 1.4, does not depend on the capacitance of the junction but only on the design of the sample and on the kinetic inductance of the grAl. Since the geometry of the sample has been confirmed by SEM observation, we adjust the simulations by changing the value of kinetic inductance and looking how the resonant frequency of the $n = 2$ and $n = 4$ mode changes. We remind that the value of kinetic inductance used for the initial simulations was of 650 pH/□ and that it corresponds to the expected kinetic inductance just after the deposition of the film. It is possible, however, that the extra steps in the fabrication process can alter this number. In particular, we have seen, that baking the samples at temperatures higher than 100 °C can cause a drop of resistivity of the metallic film and hence a reduction of kinetic inductance.

Using Sonnet to simulate the open circuit cavity with the DBR, we find that with a kinetic inductance of 560 pH/□ the resonant frequencies of the weakly coupled modes are close to the one measured in the experiment and are equal to: $\omega_2 = 2\pi \times 12.2$ GHz and $\omega_4 = 2\pi \times 23.1$ GHz. In table 3.3 we report the electromagnetic properties of the first five modes obtained by simulating the circuit in absence of the junction and with the adjusted kinetic inductance.

	$\omega_n/2\pi$ [GHz]	$\tilde{Z}_n$ [kΩ]	$\kappa_c/2\pi$ [MHz]
n = 0	1.94	3.42	30
n = 1	6.88	5.31	0.3
n = 2	12.21	0.017	13
n = 3	18.25	1.97	0.1
n = 4	23.12	2×10^{-3}	10

Table 3.3: Properties of the modes obtained simulating the open circuit sample with a grAl kinetic inductance of 560 pH/□.

At this point we can estimate the value of the capacitance of the junction by calculating the shift of the resonant frequency of the modes caused by the junction itself. We add the admittance of the capacitance to the admittance seen by the junction extracted from Sonnet and we see that with a capacitance of 1.75 fF the resonant frequency of the $n = 1$ mode matches the one measured experimentally.

	$\omega_n/2\pi$ [GHz]	$\tilde{Z}_n$ [kΩ]	$\Lambda_{n,\mathrm{qp}}$
n = 0	1.89	3.28	0.64
n = 1	5.91	4.48	0.74
n = 2	12.19	0.017	0.05
n = 3	15.54	1.66	0.45
n = 4	23.12	2×10^{-3}	0.01
n = 5	25.34	1	0.35
n = 6	34.06	$< 1 \times 10^{-3}$	< 0.01
n = 7	35.09	710	0.3

Table 3.4: Properties of the modes obtained simulating the circuit with a grAl kinetic inductance of 560 pH/□ and a junction capacitance of 1.75 fF.

For this value of capacitance also the coupling of the mode is very close to the one obtained from the fit of the experimental data. Regarding the other modes, the expected resonant frequency of the $n = 0$ mode matches the measured one while the one of the $n = 3$ mode differs of approximately 200 MHz.

3.5 Cavity linewidth broadening

In this section, we discuss the properties of the spectral width κ of the cavity's mode at $2\pi \times 5.91$ GHz and how it depends on the voltage bias and on the injected microwave power. We have seen in section 3.1, that the intrinsic loss rate of the cavity increases drastically when the voltage bias approaches $2\Delta/e - \hbar\omega_1/e$ and that this is due to photo-assisted quasiparticle tunneling. We have also shown, in paragraph 3.3.4, that, in the strong coupling regime, every energy level experiences a different exchange rate of photons with the junction and that the absorption rate, which is a step like function, rising at $2\Delta/e - m\hbar\omega_1/e$, with m indicating the number of the level. Because of this, the loss rate of the cavity also depends on the cavity population. If it is small, such that high energy levels are not populated, κ remains constants as long as $V < 2\Delta/e - \hbar\omega_1$. However, if energy level, whose photon's absorption rate is nonzero, are populated, the linewidth of the cavity increases. To quantitatively understand this behavior, we compute the expected spectrum of the cavity, by numerically solving its master equation. In the last paragraph, we show the results obtained by measuring the spectrum of the cavity at higher power and we compare them with the simulations.

3.5.1 Simulation of the cavity linewidth

We start by solving the steady-state master equation for the cavity density matrix ρ in presence of a coherent drive. Because solving the master equation for a multi-mode cavity is numerically demanding, we only consider the $n = 1$ mode and we use, for the simulations,

the parameters derived from the fit of the Lamb shift: $\omega_1 = 2\pi \times 5.91\,\mathrm{GHz}$, $\Lambda_{1,\mathrm{qp}} = 0.76$, $\gamma_0 = 2.28 \times 10^{-3}$ and $2\Delta = 398\,\mu\mathrm{V}$. The hamiltonian of the system, in the frame rotating at the frequency of the pump ω_p, is given by:

$$\hat{H} = \eta\left(\hat{a} + \hat{a}^\dagger\right) - \delta\hat{a}^\dagger\hat{a} + \hat{H}_{LS}, \tag{3.43}$$

with η being the pump rate, $\delta = \omega_1 - \omega_p$ the frequency detuning and $\hat{H}_{LS}$ the Lamb shift hamiltonian defined in equation 3.28. The steady state master equation for the single-mode driven cavity can be written as:

$$-\frac{i}{\hbar}\Big[\hat{H}, \rho\Big] + \kappa\mathcal{L}_c(\rho) + \sum_{l_1=-\infty}^{\infty} \gamma_{l_1}\mathcal{L}_{l_1}(\rho) = 0, \tag{3.44}$$

with $\mathcal{L}_c(\rho)$ being the Lindblad dissipator of the annihilation operator:

$$\mathcal{L}_c(\rho) = \hat{a}\rho\hat{a}^\dagger - \frac{1}{2}\big\{\hat{a}^\dagger\hat{a}, \rho\big\}, \tag{3.45}$$

and $\mathcal{L}_{l_1}(\rho)$ the ones of the quantum jumps operators:

$$\mathcal{L}_{l_1}(\rho) = \hat{A}_{l_1}^\dagger\rho\hat{A}_{l_1} - \frac{1}{2}\Big\{\hat{A}_{l_1}\hat{A}_{l_1}^\dagger, \rho\Big\}. \tag{3.46}$$

κ is the loss rate of the cavity, fixed equal to $2\pi \times 5\,\mathrm{MHz}$. By solving equation 3.44, we can find the steady state density matrix ρ_{ss} which allow us to compute the mean field of the cavity $\langle\hat{a}\rangle = \mathrm{Tr}\,(\hat{a}\rho_{ss})$ and the cavity's reflected spectrum S_{11}:

$$S_{11} = 1 - i\frac{\kappa_c}{\eta}\langle\hat{a}\rangle. \tag{3.47}$$

κ_c is the coupling rate that we have shown in paragraph 3.1 to be equal to $2\pi \times 450\,\mathrm{kHz}$.

In figure 3.28 we show the absolute value of the reflected cavity spectrum $|S_{11}|^2$, computed for different pump rates η. For sufficiently weak pumping (fig. 3.28a and b) only the first energy level is populated and a single resonance peak is present. We extract the effective linewidth $\tilde{\kappa}$ by fitting the simulated spectra using equation 3.1 which describe a lorentzian lineshape:

$$S_{11} = 1 - \kappa_c\frac{\tilde{\kappa}/2 - i\delta}{(\tilde{\kappa}/2)^2 + \delta^2}. \tag{3.48}$$

The result, plotted in figure 3.29, shows that in this power regime and for voltages below $2\Delta/e - \hbar\omega_1/e$, $\tilde{\kappa}$ remains constant and equal to the value of $2\pi \times 5\,\mathrm{MHz}$ set in the simulation. As the voltage reaches $2\Delta/e - \hbar\omega_1/e$, where all photons are absorbed by the junction, $\tilde{\kappa}$ increases to the value given by the single photon exchange rate $\gamma_1|w_{0,1}|^2$.

If the pump is strong enough to populate higher energy levels (fig. 3.28 (c) and (d)), the spectrum shows an overall broadening of the linewidth, especially for voltages $V > 2\Delta/e - 2\hbar\omega_1/e$, and the appearance of other resonances. As discussed before, this second effect is due to the anharmonicity induced by the Lamb shift. It would be more natural to fit the calculated spectrum, in the high power regime, with a double lorentzian function. However, since in the experiment we are not able to properly resolve the different resonances (with the exception for the voltage points very close to where the splitting of the resonances

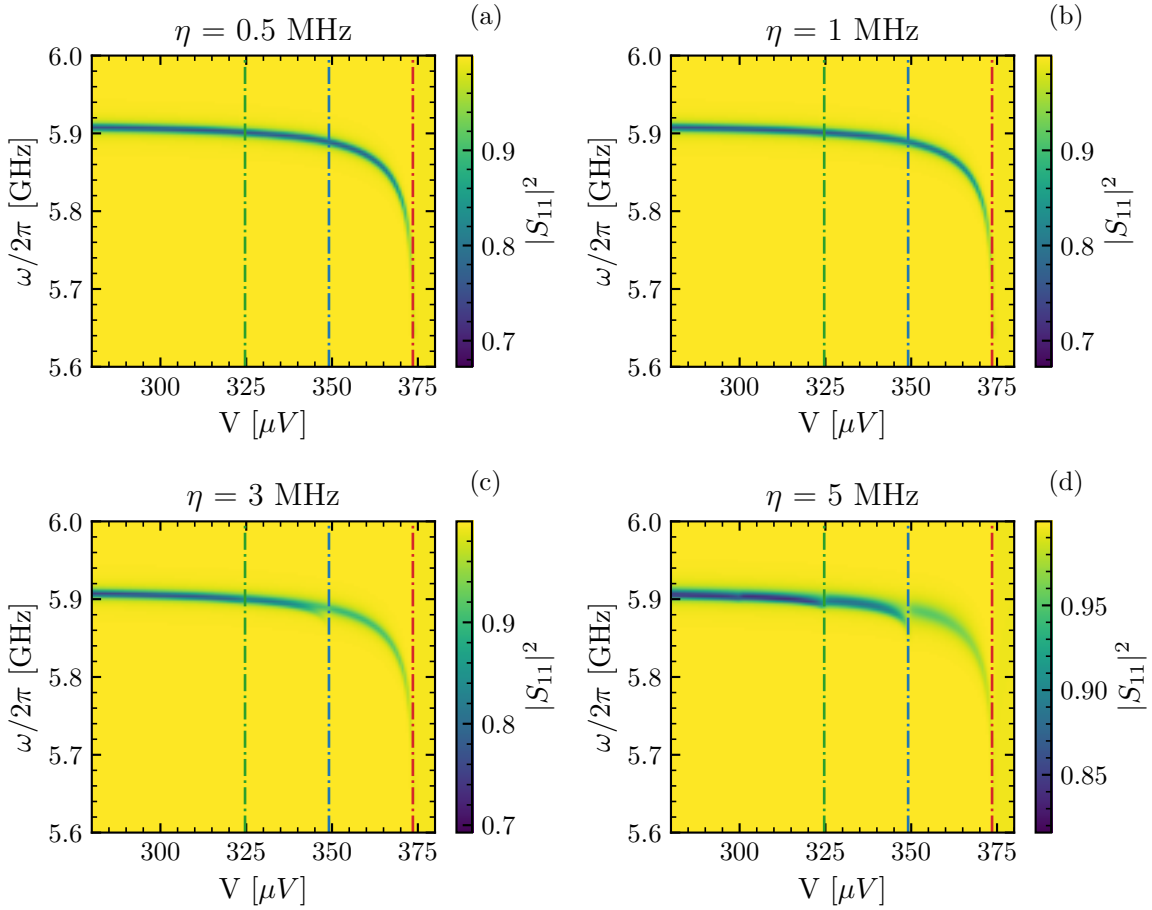

Figure 3.28: Spectrum of the cavity simulated at different pump rates η. The dashed lines indicate $eV = 2\Delta - m\hbar\omega_1$, with $m = 1, 2, 3$.

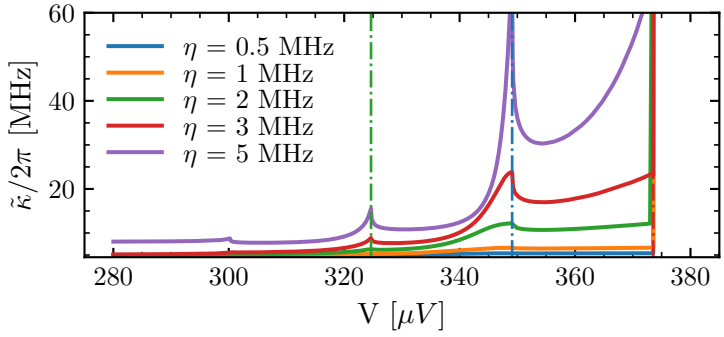

Figure 3.29: Effective cavity linewidth extracted with a lorentzian fit of the simulated cavity spectra.

happen) and we can only perform single lorentzian fit, we apply the same treatment to the simulated data. We fit $|S_{11}|^2$ and we plot the results in figure 3.29.

The main effect arising from the increment of injected power is the appearance of step-like features in the voltage dependence of $\tilde{\kappa}$. When a populated high energy level starts to

exchange photons with the junction a new loss channel is created and the linewidth of the cavity increases. The peaks appearing close to $2\Delta/e - m\hbar\omega_1$ are artifacts due to the single lorentzian fit.

3.5.2 Linewidth measurement

In section 3.1 we showed the cavity spectrum measured with an injected power of -140 dBm, and the extracted linewidth κ obtained with a lorentzian fit (figure 3.30).

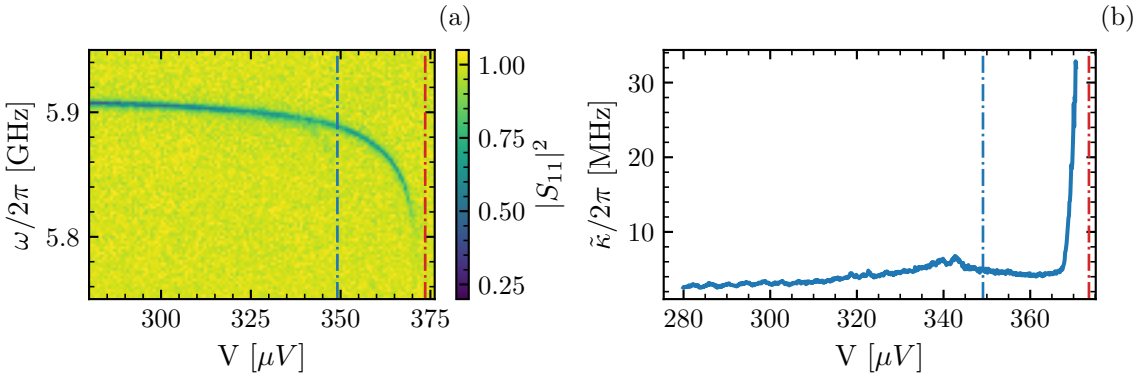

Figure 3.30: (a) $|S_{11}|$ spectrum measured with an injected microwave power of -140 dBm. The dashed lines correspond to the voltage point where $eV = 2\Delta - m\hbar\omega_1$, with $m = 1, 2$. (b) Linewidth of the cavity κ extracted fitting the spectrum with equation 3.48. The local maximum present close to the blue line is an artifact of the fit due to the splitting of two transition frequencies and does not correspond to an effective increment of intrinsic loss.

In this range of power, only a fade trace of the resonance due to the $\omega_1^{20}/2$ transition, is present. However, because we are not able to properly resolve it, we perform only a single lorentzian fit that fits both the absolute value and the phase of S_{11}. The voltage dependence of κ (plotted in 3.30 (b)) shows several features we can distinguish. First, as the voltage approaches the gap edge, κ slowly increases while showing small oscillations. These are not predicted by the simulations of the master equation and are due to the interaction between the cavity and the Cooper pairs degree of freedom of the junction. When the voltage is close to $2\Delta/e - 2\hbar\omega_1/e$ (blue dashed line in figure 3.30), κ reaches a local maximum due to the splitting of the transition frequencies and not to an effective increment of losses. After this voltage, κ remains almost constant before increasing again when $eV \approx 2\Delta - \hbar\omega_1$ (red dashed line). Here, the increment of κ is not as sharp as expected from the simulations but it happens in a region of few μV. This broadening depends on the shape of the γ functions (fig 3.13) that are not step-like functions but are smoothed either by voltage noise or a Dynes density of state. We take into account this effect by smoothing γ with a Gaussian with standard deviation σ_V. We find that we best explain the data when $\sigma_V = 2.4\,\mu\text{V}$ (figure 3.31).

High power regime

In figure 3.32 we show the spectrum of the cavity measured at higher microwave power.

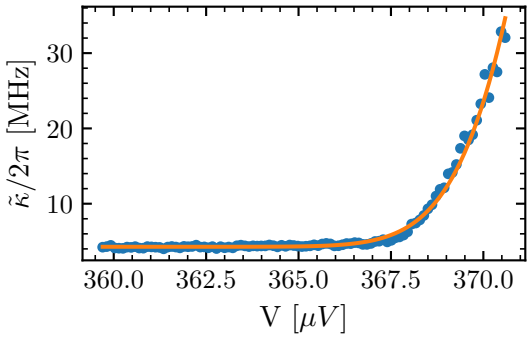

Figure 3.31: Variation of κ extracted from the fit of the spectrum. The increment of the linewidth is not as sharp as expected. We fit this behavior by smoothing the γ function by convolving them with a Gaussian of standard deviation $\sigma_V = 2.4\,\mu\text{V}$.

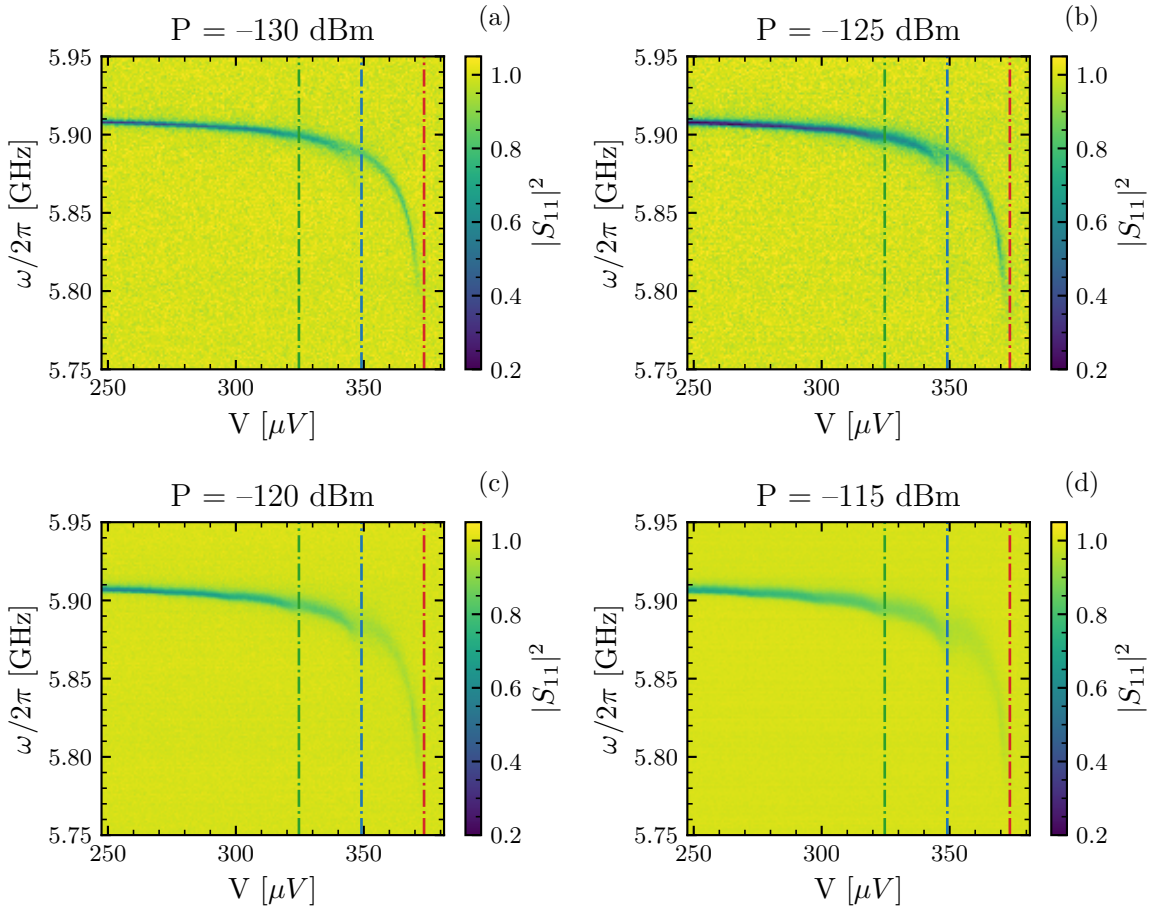

Figure 3.32: $|S_{11}$ measured with different injected microwave power (a) $P = -130$ dBm, (b) $P = -125$ dBm, (c) $P = -120$ dBm, (d) $P = -115$ dBm.

As in the simulations, we can see the effect of the junction induced anharmonicity at voltages near $2\Delta - 2\hbar\omega_1$, where multiphoton processes allow us to probe the $\omega_1^{20}/2$ transition. We fit the absolute value of the spectrum $|S_{11}|^2$ using equation 3.48 and plot the results

obtained for the resonant frequency and cavity linewidth in figure 3.33. The variation of $\tilde{\kappa}$ shows the expected step like behavior (see figure 3.29).

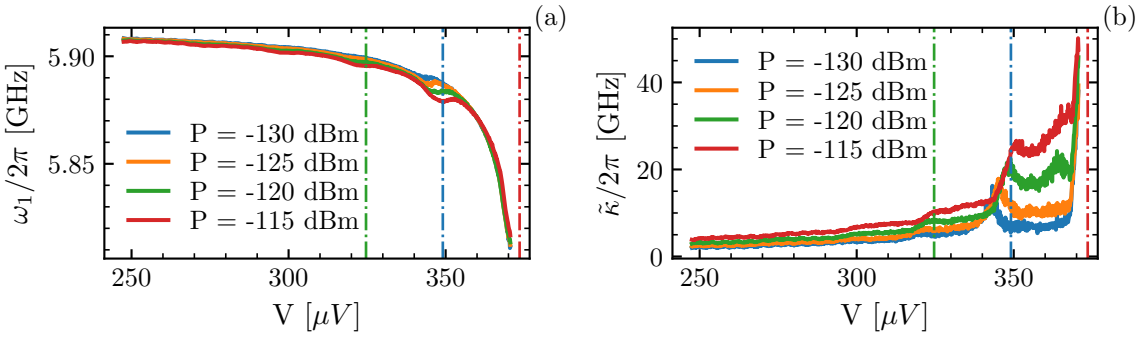

Figure 3.33: Variation of (a) the resonant frequency and (b) linewidth of the cavity as function of the voltage bias, for different injected microwave powers. When P increases dip in the frequency shift located at $eV \approx m\hbar\omega_1$ appear due to the higher energy level splitting. At the same time the linewidth of the cavity increases showing the expected step-like behavior.

3.6 Realization of an effective two level system

In this section we discuss how, exploiting the losses induced by the junction, we can restrain the dynamics of the cavity to a Fock state subspace. We focus, in particular, on the voltage region with $2\Delta - 2\hbar\omega_1 < eV < 2\Delta - \hbar\omega_1$, where, as shown in fig. 3.18, only the first energy level is not affected by the junction induced loss. We solve the steady state master equation for a driven single-mode cavity and we compute the mean value of the cavity's field and of the photon number operator. We show that, for sufficiently weak pumping, only the first energy level is populated. The cavity behaves, therefore, as an effective two-level system (TLS).

We compare the results of the simulations to the ones obtained experimentally by measuring the cavity field $\hat{a}$ and the photon number operator $\hat{a}^\dagger\hat{a}$ and we show that the model agrees quite well with the data.

3.6.1 Simulation of the cavity state

We characterize the state of the cavity by solving the single-mode master equation 3.44 and calculating the steady state density matrix ρ_{ss} as a function of the pump rate η. The frequency detuning δ is chosen such that the microwave drive is in resonance with the ω_1^{10} transition frequency. The other parameters of the simulations are the ones derived experimentally from the Lamb shift analysis and already used in 3.5.

In figure 3.34 we show the Wigner function of ρ_{ss} simulated for different values of η and with $V = 360\,\mu\text{V}$.

At low drive the cavity is in a coherent state: the field distribution is Gaussian with the mean value of both quadrature close to zero (fig. 3.34a). As η increases the Wigner function changes shape and becomes similar to the one of a two level system (fig. 3.34b and 3.34c). At very high pump rate, the cavity is neither in a coherent state or a two level system

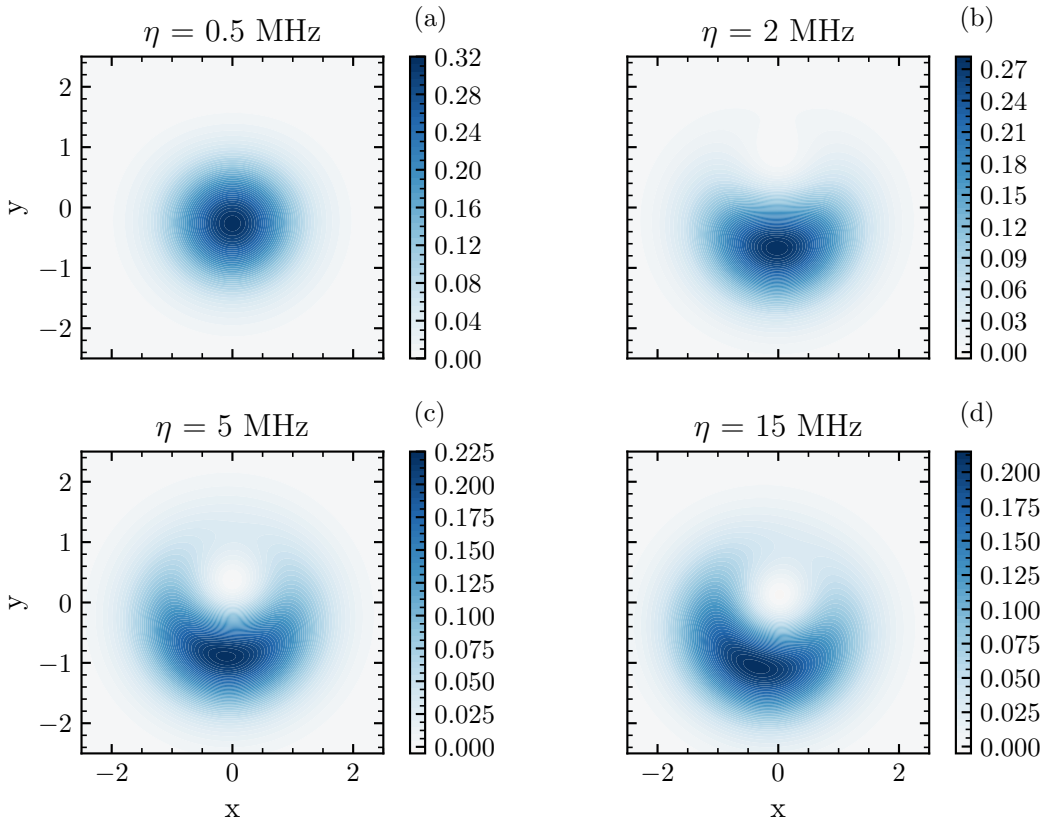

Figure 3.34: Wigner function of the steady state density matrix ρ_{ss} evaluated at different pump rates.

state (fig. 3.34d). To better understand this behavior we calculate the mean photon number $\langle \hat{a}^\dagger \hat{a} \rangle = \mathrm{Tr}\left(\hat{a}^\dagger \hat{a} \rho_{ss}\right)$ as a function of η and we compare the result, shown in 3.35, with the one calculated for an harmonic oscillator and a two level system, whose analytical expression are:

$$\langle \hat{a}^\dagger \hat{a} \rangle_{\mathrm{HO}} = \frac{4\eta^2}{\kappa^2}, \tag{3.49}$$

$$\langle \hat{a}^\dagger \hat{a} \rangle_{\mathrm{TLS}} = \frac{4\eta^2}{\kappa^2 + 8\eta^2}. \tag{3.50}$$

The mean number of photons do not follow the curve described by an harmonic oscillator. It increases much slower and shows a small plateau when $\langle \hat{a}^\dagger \hat{a} \rangle$ reaches 0.5 (red dashed line in fig 3.35). For sufficiently weak pumping the evolution of the cavity field is equivalent to the one of a TLS. We can distinguish two different regimes according to the pump rate: a first one, up to few MHz, where $\langle \hat{a}^\dagger \hat{a} \rangle$ can be parametrized using equation 3.50, and a second regime, for larger η, where the TLS description is not valid. The range of power in which the cavity behaves like an effective TLS depends on the junction induced loss rate of the second energy level that is given by $\gamma_2 |w_{0,2}|^2$.

Since the measurement of the mean number of photon involves higher order moments of the cavity field, which are more difficult to obtain, it can be useful to decompose $\langle \hat{a}^\dagger \hat{a} \rangle$ in its classical and quantum part: $\langle \hat{a}^\dagger \hat{a} \rangle = |\langle \hat{a} \rangle|^2 + \langle \hat{\delta}^\dagger \hat{\delta} \rangle$. The first term corresponds to the cavity

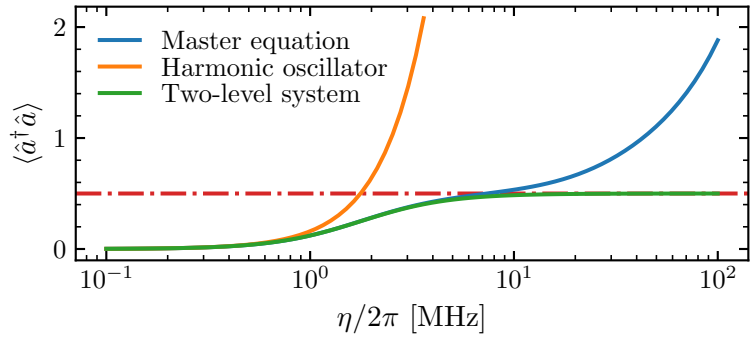

Figure 3.35: Mean photon number as a function of the pump rate η. In blue we plot the expectation value obtained from the steady state density matrix and we compare it with the same quantity obtained for an harmonic oscillator (orange) and for a two-level system (green). The red dashed line indicates $\langle \hat{a}^\dagger \hat{a} \rangle = 0.5$.

mean field and can be measured directly using a VNA. The second one instead, describes the contribution of the quantum fluctuations and it is given by the second order moment of the displaced cavity operator $\hat{\tilde{a}}$, defined such that $\langle \hat{\tilde{a}} \rangle = 0$. Figure 3.36 reports the variation of $|\langle \hat{a} \rangle|^2$ and $\langle \hat{\tilde{a}}^\dagger \hat{\tilde{a}} \rangle$ as a function of η, together with the curves describing the behavior of the same quantities in the case of an harmonic oscillator and a true two-level system that are given by:

$$|\langle \hat{a} \rangle|^2_{\mathrm{HO}} = \frac{4\eta^2}{\kappa^2}, \qquad \langle \hat{\tilde{a}}^\dagger \hat{\tilde{a}} \rangle_{\mathrm{HO}} = 0, \tag{3.51}$$

$$|\langle \hat{a} \rangle|^2_{\mathrm{TLS}} = \frac{4\eta^2\kappa^2}{(\kappa^2 + 8\eta^2)^2}, \qquad \langle \hat{\tilde{a}}^\dagger \hat{\tilde{a}} \rangle_{\mathrm{TLS}} = \frac{32\eta^4}{(\kappa^2 + 8\eta^2)^2}. \tag{3.52}$$

The simulation shows that $|\langle \hat{a} \rangle|^2$ increases with η reaching a maximum, it then decreases before increasing again when the TLS approximation breaks down. This behavior is similar to the one a of true TLS where $|\langle \hat{a} \rangle|^2$ goes through a maximum of 0.125 (black dashed line in figure 3.36a) when $\eta = \kappa/2\sqrt{2}$ and then decreases to zero at large η, when the state becomes a 50/50 mixture of $|0\rangle$ and $|1\rangle$ Fock state (which is rotationally invariant and has $\langle \hat{a} \rangle = 0$). The maximum reached by the solution of the master equation does not coincide with the maximum of 0.125 reached in a true TLS and it is slightly bigger. At the same time, the quantum fluctuations $\langle \hat{\tilde{a}}^\dagger \hat{\tilde{a}} \rangle$ of the master equation solution, increase reaching a maximum of approximately 0.35 and then decrease again when the TLS approximation is not valid anymore. In a true TLS instead, they increase from zero to 0.5 (red dashed line in 3.36b) and they remain constant. In conclusion, even if the mean number of photons of both the restrained cavity and the true TLS is 0.5 until η is approximately $2\pi \times 10\,\mathrm{MHz}$ (fig. 3.35), in the first case there is a higher contribution of the mean field term while in the second one quantum fluctuations are larger.

To validate that this behavior is an effect arising from the restriction of the cavity dynamics to a two energy levels Fock state subspace, we plot the mean number of photons and the mean field calculated at different voltages.

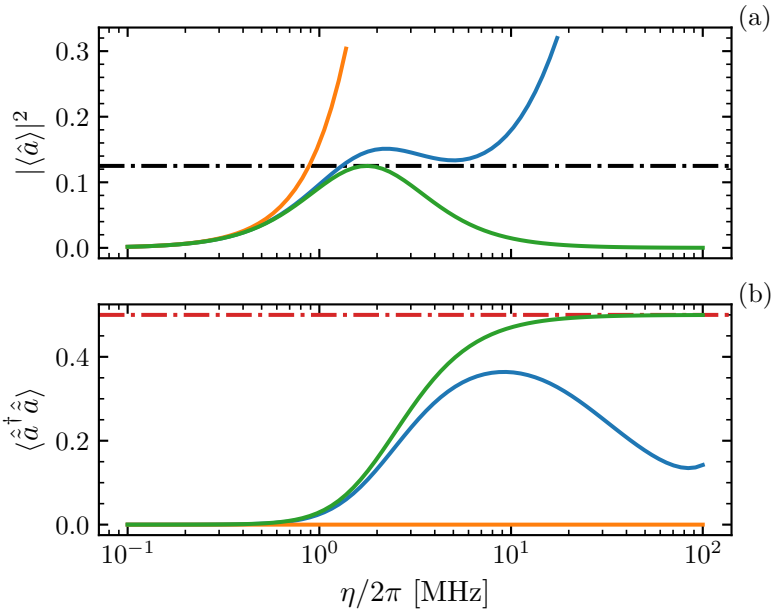

Figure 3.36: (a) Cavity mean field and (b) quantum fluctuations contribution to the mean photon number. The color legend is the same as in fig. 3.35. The black dashed line in (a) and the red dashed line in (b) indicate the maximum value of mean field and quantum fluctuations reached by a true TLS.

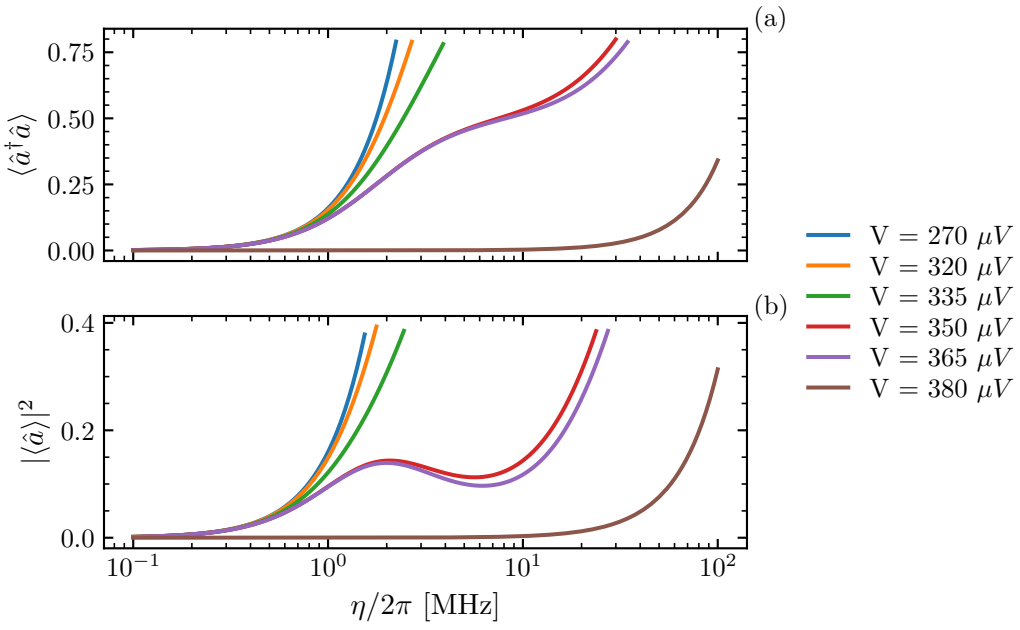

Figure 3.37: (a) Mean photon number and (b) cavity mean field as a function of the pump strength, calculated at different voltages.

When V is far from the gap edge $|\langle\hat{a}\rangle|^2$ and $\langle\hat{a}^\dagger\hat{a}\rangle$ follow, in the range of power considered, the curves describing an harmonic oscillator. As the voltage increases, the effect of the lossy

higher energy levels starts to be relevant and the two curves change. In the region where only the first energy level doesn't exchange photons with the junction we recover the curves previously discussed. At even larger voltages, where all the cavity states are lossy the number of photons is always zero, unless η is very strong.

TLS linewidth

Because the system behaves as an effective TLS, we parameterize its linewidth with the equations describing one of a TLS. From the steady state density matrix, evaluated at different pump detuning δ, we compute the spectrum of the cavity S_{11} that is given by:

$$S_{11} = 1 - i\frac{\kappa_c}{\eta}\langle\hat{a}\rangle, \tag{3.53}$$

with $\kappa_c = 2\pi \times 450\,\text{kHz}$. The reflected spectrum of a TLS is given by [48]:

$$S_{11}(\omega) = 1 - \kappa_c \frac{\tilde{\kappa}/2 - i\delta(\omega)}{(\tilde{\kappa}/2)^2 + \delta^2(\omega) + \gamma_p^2}, \tag{3.54}$$

with the parameter γ_p taking into account the linewidth broadening induced by the saturation of the excited energy level and equal to $\gamma_p = \sqrt{2}\eta$.
We fit the simulated curves with equation 3.54, leaving as free parameter the effective linewidth $\tilde{\kappa}$ and γ_p. The fit converges only for $\eta < 2\pi \times 5\,\text{MHz}$, compatibly with the fact that, for stronger pump, the TLS approximation is not valid anymore. In figure 3.38 we plot the variation of the fit parameters κ and γ_p as function of the pump rate η.

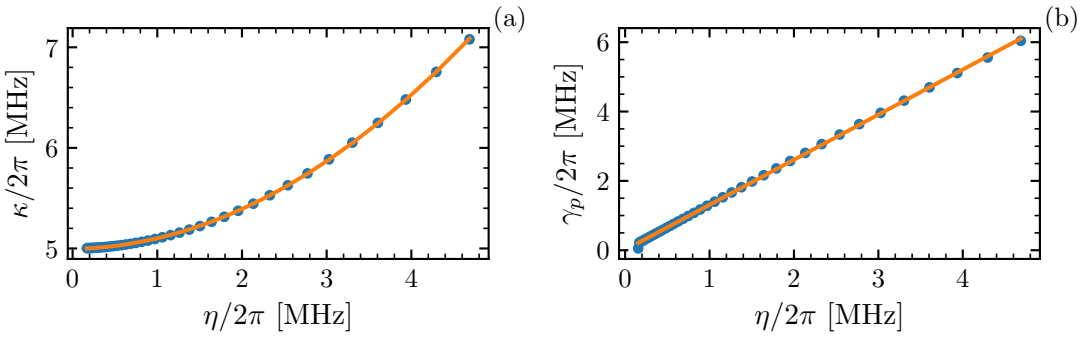

Figure 3.38: Variation of (a) κ and (b) γ_p for the simulated cavity linewidth as function of the pump rate η. The orange curves show the quadratic and linear dependence of κ and γ_p on η.

While in a TLS, κ doesn't depend on the pump rate and remains constant, in a cavity coupled to a junction it grows quadratically with η. At zero pump, however, it converges to the value of $2\pi \times 5\,\text{MHz}$ set in the simulations. γ_p instead increases linearly with η and the linear dependence is close to the on of a TLS with $\gamma_p \approx \sqrt{2}\eta$

3.6.2 Measurement of the cavity field

Cavity spectrum and mean field

We start the characterization of the cavity field by measuring its spectrum at different microwave powers with a voltage bias $V = 363\,\mu$V that we report in figure 3.39.

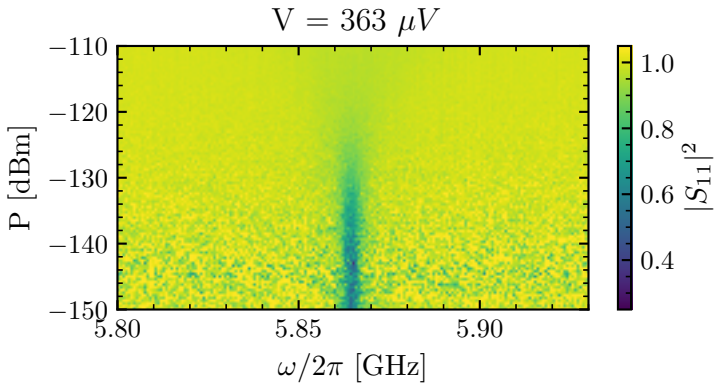

Figure 3.39: Spectrum of the cavity as function of the injected microwave power measured at $V = 363\,\mu$V.

As expected, the linewidth of the cavity increases with the strength of the pump before the resonance completely disappears. As discussed above this broadening is a saturation effect, in the region of power where the cavity behaves like a TLS while in the high power regime is due to the population of lossy levels. For low powers, we fit S_{11} with equation 3.54 using as free parameter the frequency detuning δ, the effective cavity linewidth $\tilde{\kappa}$ and the saturation parameter γ_p (we show the spectrum measured at $P = -130$ dBm together with its fit in figure 3.40).

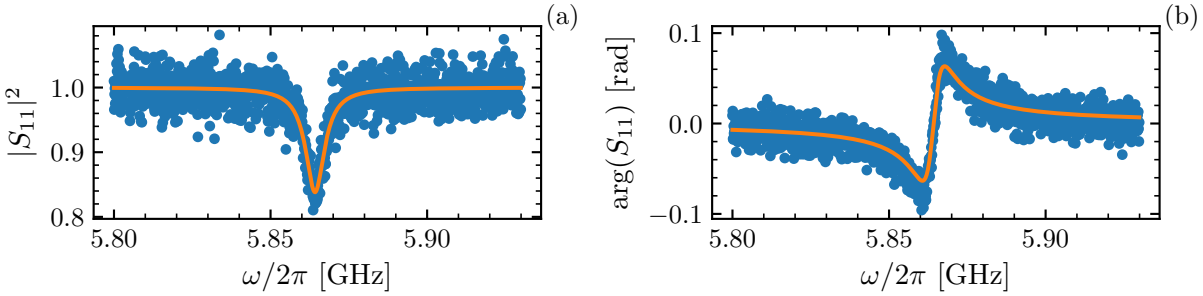

Figure 3.40: Spectrum of the cavity measured at 352 µV and with an injected power $P = -130$ dBm. From the fit, performed with a TLS lineshape function we get $\omega_1^{10} = 2\pi \times 5.86$ GHz, $\kappa = 2\pi \times 5.2$ MHz and $\gamma_P = 2\pi \times 2.6$ MHz.

The resonant frequency remains constant with power while the behavior of $\tilde{\kappa}$ and γ_p is shown in figure 3.41, for $P < -125$ dBm. From the evolution of this last parameter and using the results obtained from master equation simulations, we can calibrate the microwave pump and estimate precisely the power injected in the cavity. η is linked to the microwave

power through $\eta = \sqrt{\kappa_c P/(\hbar\omega_1)}$ and by imposing $\gamma_p \approx \sqrt{2}\eta$ (figure 3.41b) we find that the actual power injected in the cavity is -13.5 dB lower than the one we consider. This gives us an estimate of the extra attenuation of the cables of the setup. A variation of 10 % of the slope γ_p/η causes a change in the total attenuation of approximately -1 dB. Regarding the linewidth $\tilde{\kappa}$ we recover the quadratic dependence on η (figure 3.41a) as expected from the simulations. The value of $\tilde{\kappa}$ at low power is $2\pi \times 4.2$ MHz.

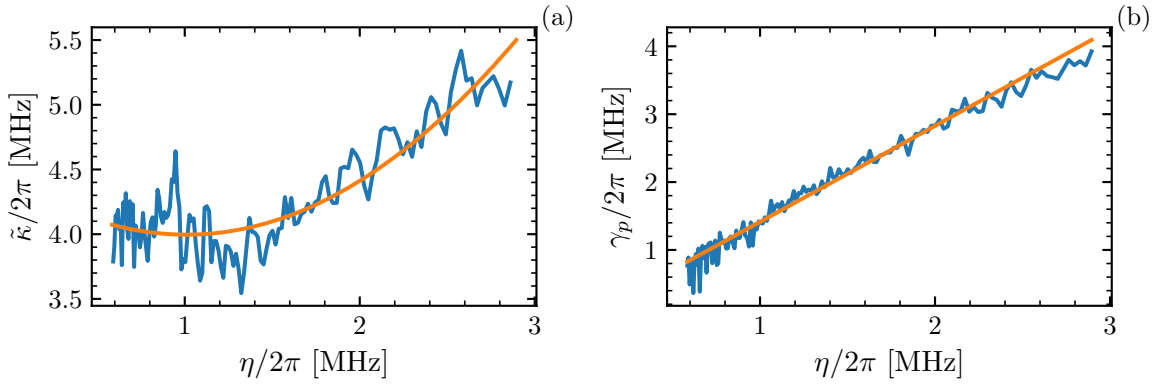

Figure 3.41: Variation of (a) the cavity linewidth κ and of the (b) saturation parameter γ_p as a function of the pump rate η. By imposing $\gamma_p = \sqrt{2}\eta$, we obtain an absolute calibration of the incoming power on the cavity

Using the calibration of the pump rate η we extract the cavity field $\hat{a}$, by inverting equation 3.53. We plot it in figure 3.42a, together with the fit performed numerically solving the master equation. $\Lambda_{1,\mathrm{qp}}$ and 2Δ are fixed to 0.75 and 398 μeV while we use as free parameters the cavity-bath coupling γ_0 and the coupling rate κ_c. The first, that depends on the junction normal resistance and on the population of the spectator modes, that we assume to be in vacuum, results to be equal to 1.55×10^{-3}, while κ_c given from the fit is $\kappa = 2\pi \times 430$ kHz, very close to the value of $2\pi \times 450$ kHz obtained in 3.1.

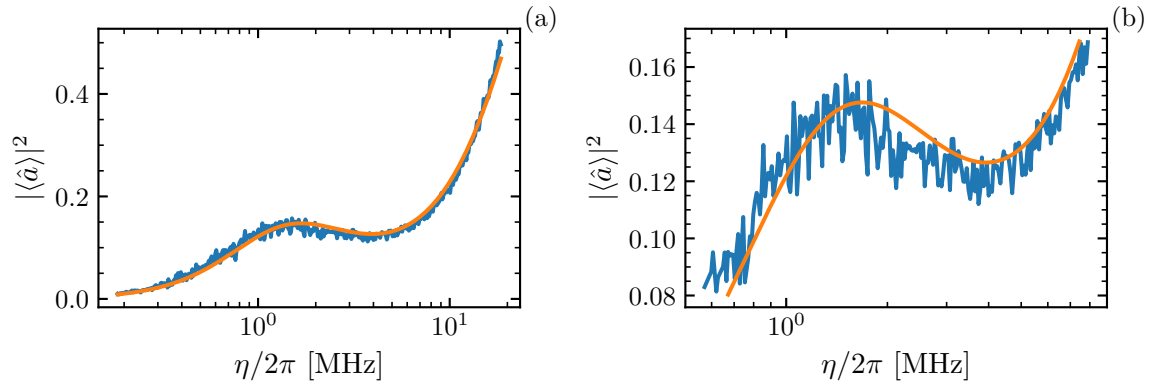

Figure 3.42: (a) Cavity mean field measured at $V = 363\,\mu$V. The fit (in orange) is performed by numerically solving the master equation. Panel (b) shows a zoom of the data and the fit near the local maximum of the field.

Figure 3.42b shows a zoom of the experimental data and of the fit in the range of η where it is possible to see how the cavity field reaches a local maximum and then decreases.

For comparison we also measure the cavity's mean field at different voltages (figure 3.43) and we confirm that the plateau is only present when $eV > 2\Delta - 2\hbar\omega_1$ (red and purple curves).

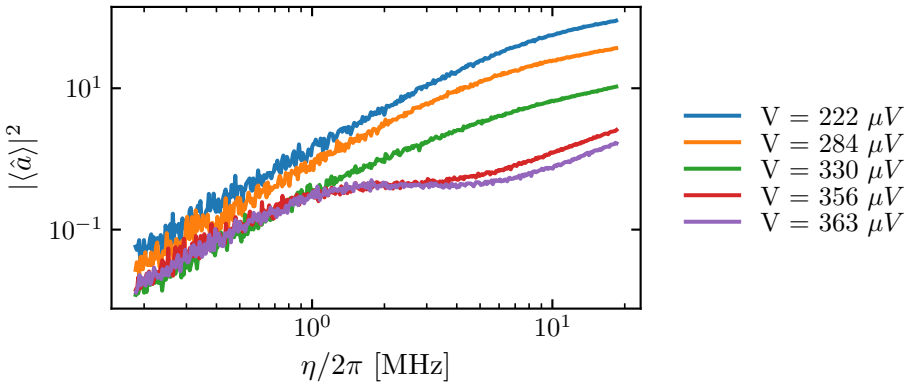

Figure 3.43: Cavity mean field measured at different voltages.

Quantum fluctuations

Since we cannot measure directly with the VNA the photon number fluctuations $\langle\hat{\tilde{a}}^\dagger\hat{\tilde{a}}\rangle$, we use the pumping and detection scheme presented in 2.3.2. To extract the cavity signal from the measured one we calibrate the noise added by the amplifier by performing a reference measurement when the cavity is in vacuum (as discussed more in detail in C). Since we perform a reflection measurement, we need to take into account in the calibration also the reflected pump and we do so by biasing the junction at 385 µV and measuring the moments of the reflected field. We choose this voltage because when eV is above $2\Delta - \hbar\omega_1 \approx 370$ µeV the cavity is empty due to high losses. We therefore assume that the cavity is in vacuum and use this measurement of the moments as reference measurement. Because the gain of the amplifier is not constant but drifts in time we alternate short measurement (typically 50/80 data points) between the voltage at which we want to measure the cavity and the reference voltage. The cut off frequency of the low pass digital filter of the card is set to 7 MHz and we vary the strength of the pump by changing the attenuation of the tunable attenuator present in the injection line. Thus, by alternating measurement of the state of the cavity (performed at 363 µV) and reference measurement and by subtracting the effects of the amplifier (equation C.6 and C.13) we calculate the cavity field and the photon number fluctuations at different pumps. We show the results in fig. 3.42.

Because the setup used for this measurement is different from the one previously calibrated, we fit $|\langle\hat{a}\rangle|^2$ to obtain the gain and the pump calibration. As before, the fit is done using as free parameters the cavity-bath coupling γ_0, the gain and the pump calibration and the result is plotted in 3.42a together with the data. The value of γ_0 we obtain is equivalent to the one derived from the measurement of the spectrum while the pump calibration differs of few dB.

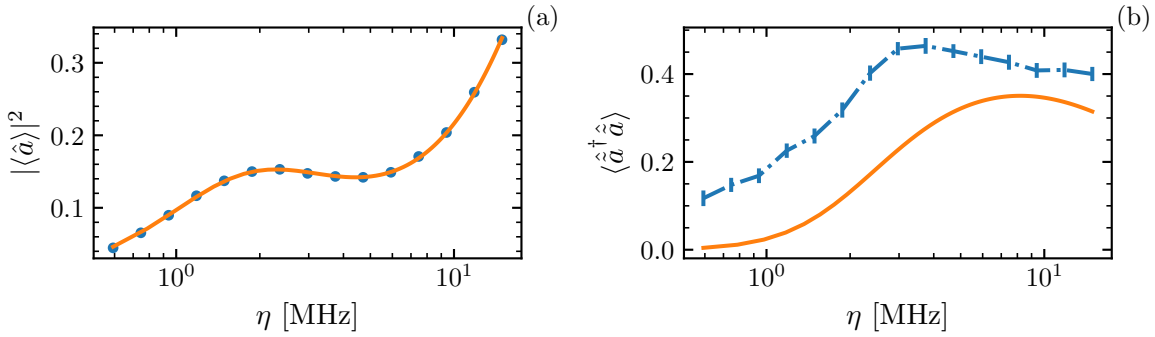

Figure 3.44: (a) Mean field $|\langle\hat{a}\rangle|^2$ and (b) quantum fluctuations $\langle\hat{a}^\dagger\hat{a}\rangle$ measured at $V = 363\,\mu V$. The amplitude of the fluctuations is not compatible with the results of the fit.

In figure 3.42b we plot also the photon number quantum fluctuations $\langle\hat{a}^\dagger\hat{a}\rangle$ where we show the measured data together with the expected curve. The two curves do not agree with each other and, in particular, the amplitude of the measured fluctuations is much bigger than the expected one. This is actually due to the tail of the Josephson emission. In figure 3.45 we show the mean number of photons (in arbitrary units) as a function of the voltage bias, in the absence of coherent drive.

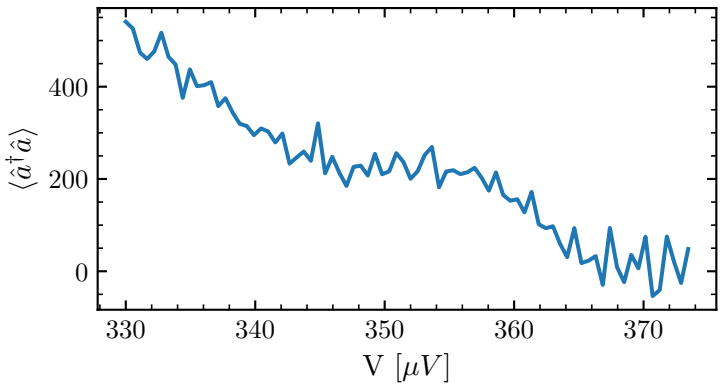

Figure 3.45: Number of photons (in arbitrary units) as function of the voltage bias, due to the Josephson emission.

Even at high voltage, there is a non zero contribution to the number of photons coming from the Josephson emission. If we remove the effect of these fluctuations from the one measured with the pump, the parameters obtained from the fit of the mean field better explain the data (figure 3.46) even if the fit doesn't match the measured curve.

Because of the field fluctuations due to the Josephson emission we are not able to further characterize the state of the cavity, by measuring for example the second order correlation function, and we have to restrain ourselves to the measurement of the low order moments of the cavity field operator.

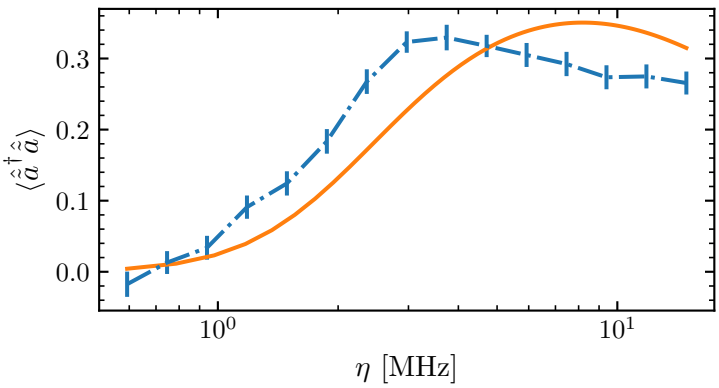

Figure 3.46: Quantum fluctuation together with the expected curve calculated using the parameters obtained from the fit of mean field.

Conclusions

In this chapter, we studied the interaction between the quasiparticle degree of freedom and the cavity. We have shown that the main effects arising from this interaction are a shift of the resonant frequency and an increase of intrinsic losses when the junction is biased at voltages near the superconducting gap. We have discussed how, in the strong coupling regime quantum effects are non negligible and give rise to Fock state dependent single photons processes. As a consequence, every cavity's energy level experiences a different Lamb shift and a different exchange rate of photons with the junction. Using the theory developed in [31], that we extended to the multi-mode cavity case, we were able to model the shift of the energy levels of the $n = 1$ mode of the cavity. By performing single and two tone spectroscopy we probed different transition frequencies, whose fit allowed us to obtain the junction-mode of the coupling $\Lambda_{1,\mathrm{qp}} = 0.75 \pm 0.01$ and the superconducting gap $2\Delta = (397 \pm 3)\,\mu\mathrm{eV}$. However, from the Lamb shift we couldn't precisely estimate the value of the cavity's bath coupling γ_0 since it depends also on the spectator modes that we couldn't measure directly.

We also studied the variation of the linewidth of the cavity and we have shown how it depends on the voltage bias and on the population of the cavity, that is directly linked to the pump strength. Using the solution of the single mode master equation we computed the spectrum of the cavity and the expected linewidth. The simulations show a good agreement with the data especially at high voltages ($eV > 2\Delta - 2\hbar\omega_1$).

Last, we have seen how exploiting the junction induced losses we can restrict the cavity's dynamics to the first two energy levels and realize an effective TLS. We performed measurements of the cavity's mean field and quantum fluctuations as function of the pump rate and show how these are well explained by a TLS model.

Chapter 4

Josephson emission and current

Contents

In this chapter, we present experimental results that we attribute to the inelastic tunneling of Cooper pairs through the junction while the different modes of the resonator are populated. We measure the dc current through the junction as well as the population in the $n = 1$ mode, which results in the emission of photons around 6 GHz by the circuit. From the previous observations of inelastic Cooper pair tunneling [24], one might expect to observe emission at 6 GHz and a dc current when the bias voltage is such that $2eV = m\hbar\omega_1$, where $m = 1, 2, \ldots$. Because the coupling parameter Λ_{cp} is on the order of 1.5, the processes with the highest probability are the one corresponding to the creation of $m = 1$ or $m = 2$ photons per tunneling event when the mode is initially in vacuum (see fig.3.12a). These arguments lead to the conclusion that a few emission peaks at voltages where the Josephson frequency is a multiple of 6 GHz should be observed.

Our data show that this approach is too naive to describe our system. In the first section, we present the joint measurement of the dc current and the 6 GHz photon emission intensity as a function of the bias voltage. We observe more than 70 peaks for both quantities with a periodic structure, whose period is close to the frequency of the $n = 0$ at 1.9 GHz, which happens to be also almost equal to $\omega_1/3$. This periodic structure extends over the entire gap, with a broad maximum both in current and 6 GHz emission intensity around $2eV/\hbar \approx 2\pi \times 80$ GHz, which corresponds to roughly $13\,\omega_1$.

In order to understand this behavior, in stark contrast with previous observations of inelastic Cooper pair tunneling, both the high quality factor of the $n = 1$ and higher order modes, as well as the multi-mode structure of the resonator have to be taken into account. This is the conjunction of these two effects that give rise to the observed broad periodic structure. In the absence of the other modes, because the loss rate of the $n = 1$ mode is much smaller (10^{-3}) than the pumping rate, which is given by E_J multiplied by a matrix element on the order of unity, a numerical solution of the master equation shows that a large population builds up in the mode, even when the Josephson frequency is a large multiple of ω_1. This comes from the fact that the matrix element of a high-order process m between $|n\rangle$ and $|n + m\rangle$ increases with n before going through a maximum. When the loss rate is sufficiently small, even if the initial pumping starting from vacuum is inefficient, because the population does not decay and the pumping becomes more and more efficient when the population grows, simulations show that a significant population could be observed up to $m \approx 13$ for our parameters. However, this effect alone does not quantitatively explain our data, because the presence of the other modes cannot be neglected. The resulting multi-mode master equation becomes difficult to solve because of the exponential growth of the Hilbert space dimension with the number of modes. In order to be able to still make some predictions, we use a phase space technique often used in quantum optics to transform the master equation into a Fokker-Planck equation, which can be simulated with stochastic classical trajectories. This transformation relies on an approximation, which is not fully justified for our system, but allows us to obtain numerical results that are in qualitative agreements with the observed dc current and emission at 6 GHz.

4.1 Emission spectrum and current measurements

Here, we show the data corresponding to the 6 GHz emission as a function of the voltage bias. We observe 72 emission peaks with different amplitude, spanning across the whole superconducting gap. In order to link this emission of photons to inelastic Cooper pair

tunneling, we also measure the current through the junction. However, we find that the voltages corresponding to the maxima of emission and the maxima of current do not always coincide. We attribute this effect to the fact that photons are emitted in other modes and that the current is not proportional only to the population in the $n = 1$ mode.

The microwave measurement shown in this section have been performed using the setup presented in chapter 2.3, while the junction is biased using the setup B (2.3.3) that allow us to measure the dc current. Unless stated otherwise, all the data have been measured at a constant temperature of 10 mK

4.1.1 Josephson emission spectrum

We start by showing, in figure 4.1a, the emission spectrum $|S|^2$ measured at different voltage bias with a spectrum analyzer. We distinguish several emission peaks at frequencies between $2\pi \times 5.86\,\text{GHz}$ and $2\pi \times 5.87\,\text{GHz}$[1], with the highest signal recorded close to 160 µV. This voltage corresponds to a Josephson frequency $\omega_J = 2eV/\hbar \approx 2\pi \times 77\,\text{GHz}$ that is approximately $13\omega_1$. At low bias (fig. 4.1b), the first peak is measured at $V \approx 20\,\mu\text{V}$ ($\omega_J \approx 2\pi \times 9.5\,\text{GHz}$) and it has a much smaller amplitude compared to the peaks measured at larger voltages.

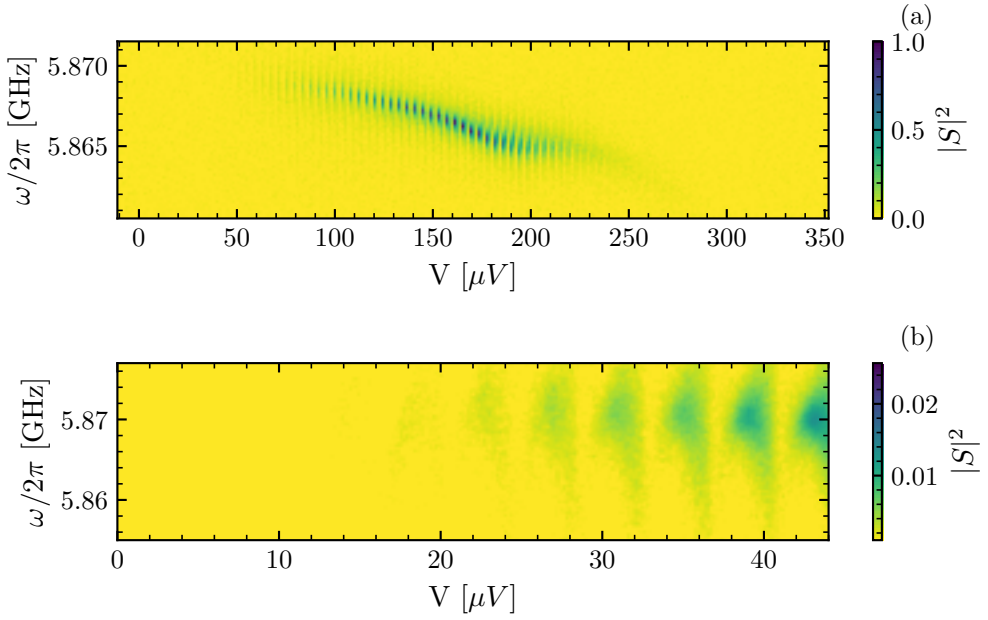

Figure 4.1: (a) Normalized emission spectra measured at different voltages. (b) shows a zoom of panel (a) when V is close to zero.

In the voltage range between 50 µV and 250 µV, where the signal to noise ratio is sufficiently good, we fit the spectrum with a lorentzian function and extract the emission frequency ω_{em} and linewidth κ_{em} that we show in figure 4.2. We observe oscillations both in

[1]This value slightly differs from the one discussed in chapter 3 since the two measurements were performed during different cool-downs.

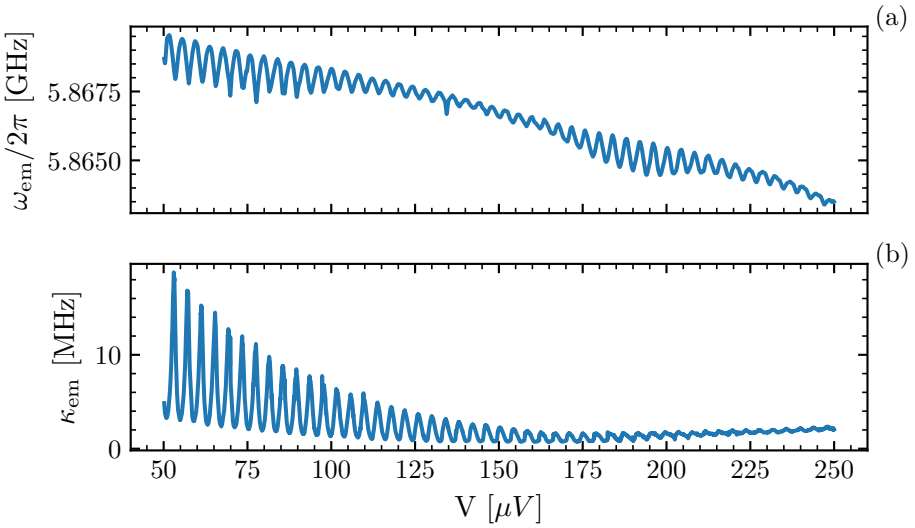

Figure 4.2: Variation of the (a) resonant frequency and (b) damping rate of the mode, extracted by fitting with a lorentzian function the spectra showed in figure 4.1.

the variation of ω_{em} and of κ_{em} but, while the resonant frequency changes of less than 1 %, the damping rate oscillates between $2\pi \times 3\,\text{MHz}$ and $2\pi \times 18\,\text{MHz}$ when V is small. The amplitude of these oscillations reduces as the voltage increases and κ_{em} reaches a minimum of $2\pi \times 0.8\,\text{MHz}$ when $V = 165\,\mu\text{V}$. The normalized spectrum measured at this voltage, together with its fit, is shown in figure 4.3.

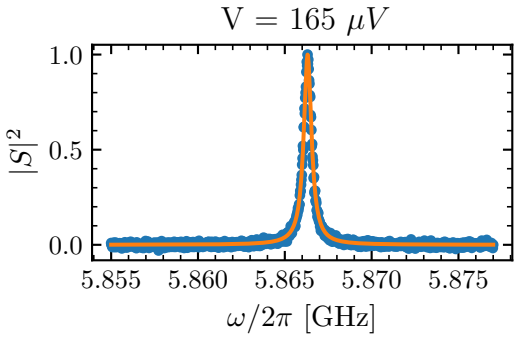

Figure 4.3: Emission spectrum measured at 165 µV. From the lorentzian fit (in orange) we obtain $\omega_{em} = 2\pi \times 5.86\,\text{MHz}$ and $\kappa_{em} = 2\pi \times 0.8\,\text{MHz}$.

4.1.2 Oscillation of the intensity of emission

To obtain the emitted power P_{em} as a function of the voltage bias, we alternate measurements of the emission spectrum with calibration measurements at zero bias, where the emission must be zero. We subtract the trace at zero bias from the ones at finite bias and integrate the

result over a bandwidth of 20 MHz. The results, plotted in figure 4.4, show the presence of 72 emission peaks with a periodic structure.

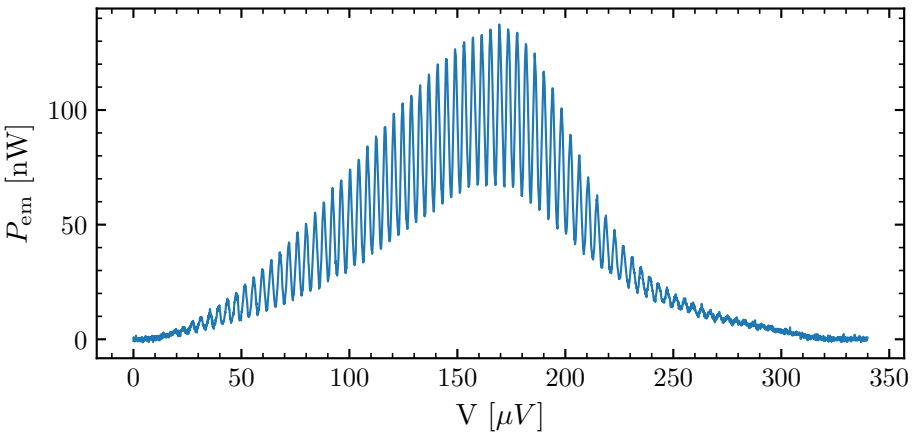

Figure 4.4: Power emitted from the junction as a function of the voltage bias.

At low voltages, we attribute this periodic peak structure to processes, where m_0 photons are created in the $n = 0$ mode and m_1 photons in the $n = 1$ mode, this process is resonant when $2eV = \hbar(m_0\omega_0 + m_1\omega_1)$. Because $\omega_1 \approx 3\omega_0$, this gives rise to a periodic peak structure with a period $\omega_1/3 \approx \omega_0$ in terms of Josephson frequency $2eV/\hbar$. Simulations detailed in 4.2 will show that the main period is fixed by the frequency of the $n = 1$ mode, which has the highest Λ_{cp} factor. We use here this result to confirm that the 1% precision claimed on the calibration of the bias voltage in 3.4 is justified.

We fit the peaks observed between 40 µV and 230 µV using a lorentzian function and find that they are spaced on average by (4.07 ± 0.02) µV and have a width of (3.2 ± 0.3) µV (the uncertainties are given by the standard deviation of the fit results). The spacing between every fourth peak (two peaks spaced such that two other peaks lie in between) is equal to 12.21 µV, which corresponds to Josephson frequency of $2\pi \times 5.91$ GHz. In the same voltage range, the average emission frequency is $2\pi \times 5.87$ GHz, which coincides with the observed peak spacing better than 1%.

4.1.3 Josephson current measurement

To better understand the emission spectra previously discussed, we measure the current through the junction for voltages below the superconducting gap. We do so by measuring the voltage drop across the 10 kΩ resistor present in the bias setup. Since we deal with current of few pA, for each voltage point, we perform a calibration measurement at zero bias and we subtract this contribution from the measured current. In this way we can remove the gain drift of the room temperature amplifier. We acquire several traces that we average and we plot the results in figure 4.5.

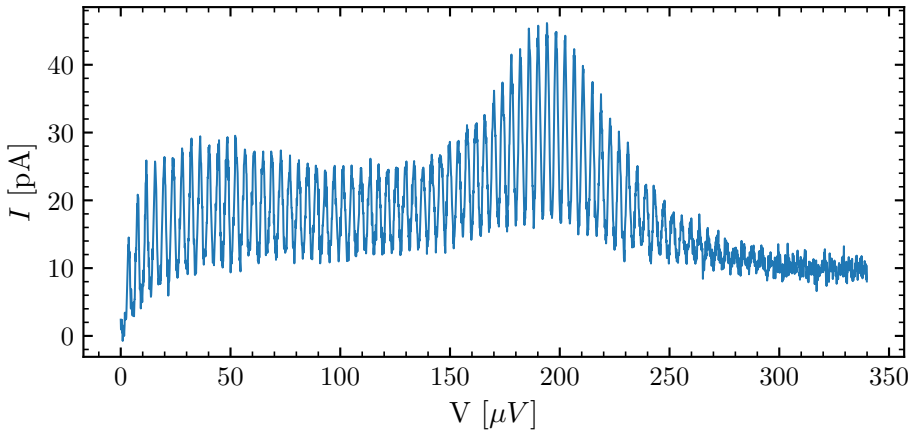

Figure 4.5: Junction sub-gap current as a function of bias voltage. The spacing between two successive peaks is almost equal to the ones observed in the emission (fig. 4.4) but the two combs are slightly dephased.

.

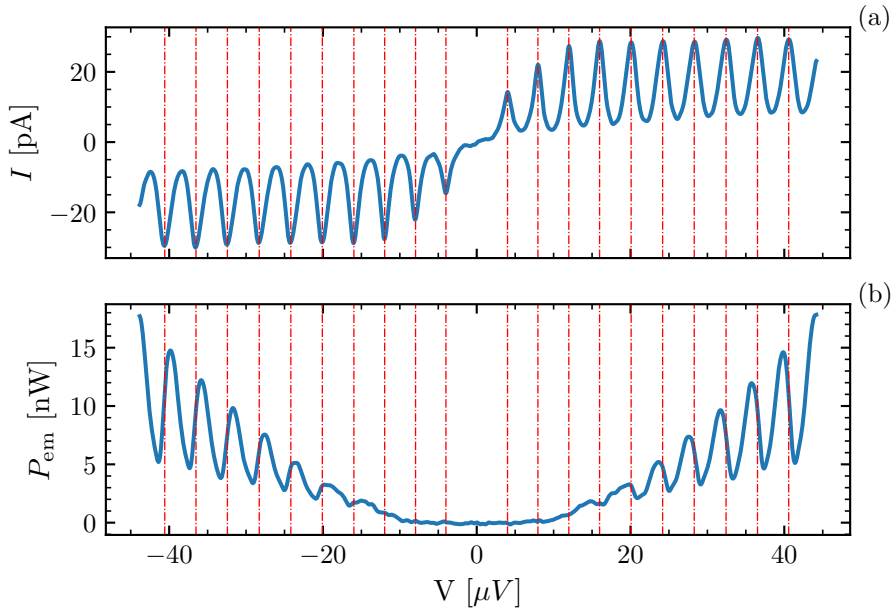

Figure 4.6: (a) Supercurrent and (b) junction emitted power as a function of the voltage bias. The red dashed lines are centered on the current peaks and indicate how not all the tunneling processes correspond emission of photons in this mode.

.

As in the case of the junction emitted power, we observe several peaks (approximately 76) from zero bias up to 300 µV. At larger voltages, peaks are not easily distinguished but we still measure a sub-gap current of approximately 10 pA. Because of energy conservation, the power emitted by photons leaking out of the different modes must be equal to the electrical power IV[28]. At zero temperature, the expression for the tunneling current is then given by:

$$I = 2e \sum_n \kappa_n \langle \hat{a}_n^\dagger \hat{a}_n \rangle (\omega_n/\omega_J), \tag{4.1}$$

If the $n = 1$ term dominates in the sum, we expect that I and P_{em} to have their maxima at the same voltages. Figure 4.6 show that this is not always the case. The first current peak is measured at $V = 4\,\mu\text{V}$ while emission only happens above 20 µV. In figure 4.8 we plot the normalized current versus the normalized emission at different voltages. Each of the panel shows the two quantities measured in a 11 µV range, starting from zero (panel 1) up to 275 µV (panel 25). We observe that the two curves are out of phase when $V < 190\,\mu\text{V}$ and in phase in the 190 µV to 240 µV range. This is a direct proof that other modes are populated and contribute to the sum of equation 4.1.

4.1.4 Emission and current temperature dependence

We have also measured the emission and current for different temperatures as shown in figure 4.7. As the temperature increases, the amplitude of the periodic pattern decreases, both for the emitted power and the current, while the number and the position of the peaks almost does not change.

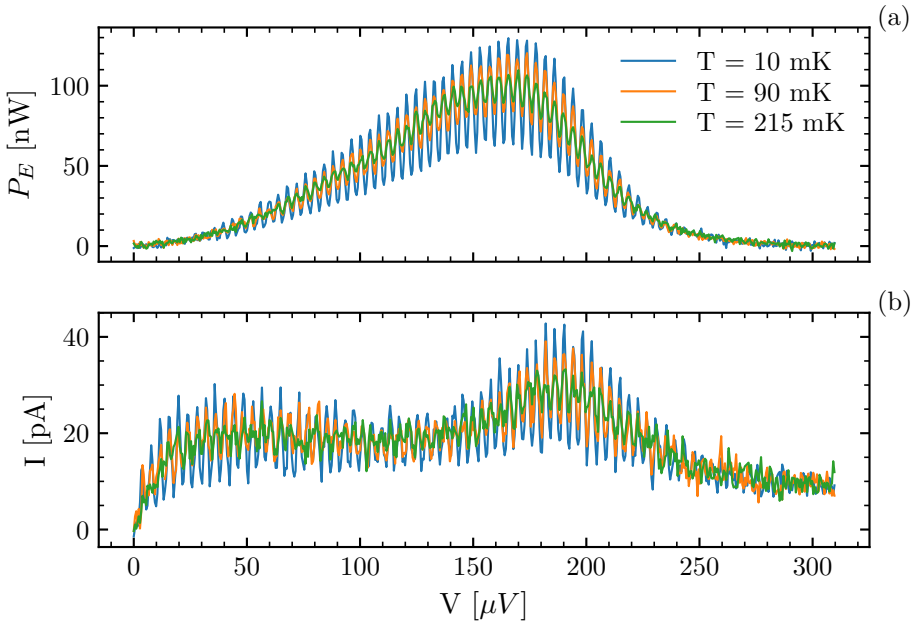

Figure 4.7: Power emitted from the junction around 6 GHz and current through the junction measured at $T = 10\,\text{mK}$, $T = 90\,\text{mK}$ and $T = 215\,\text{mK}$

.

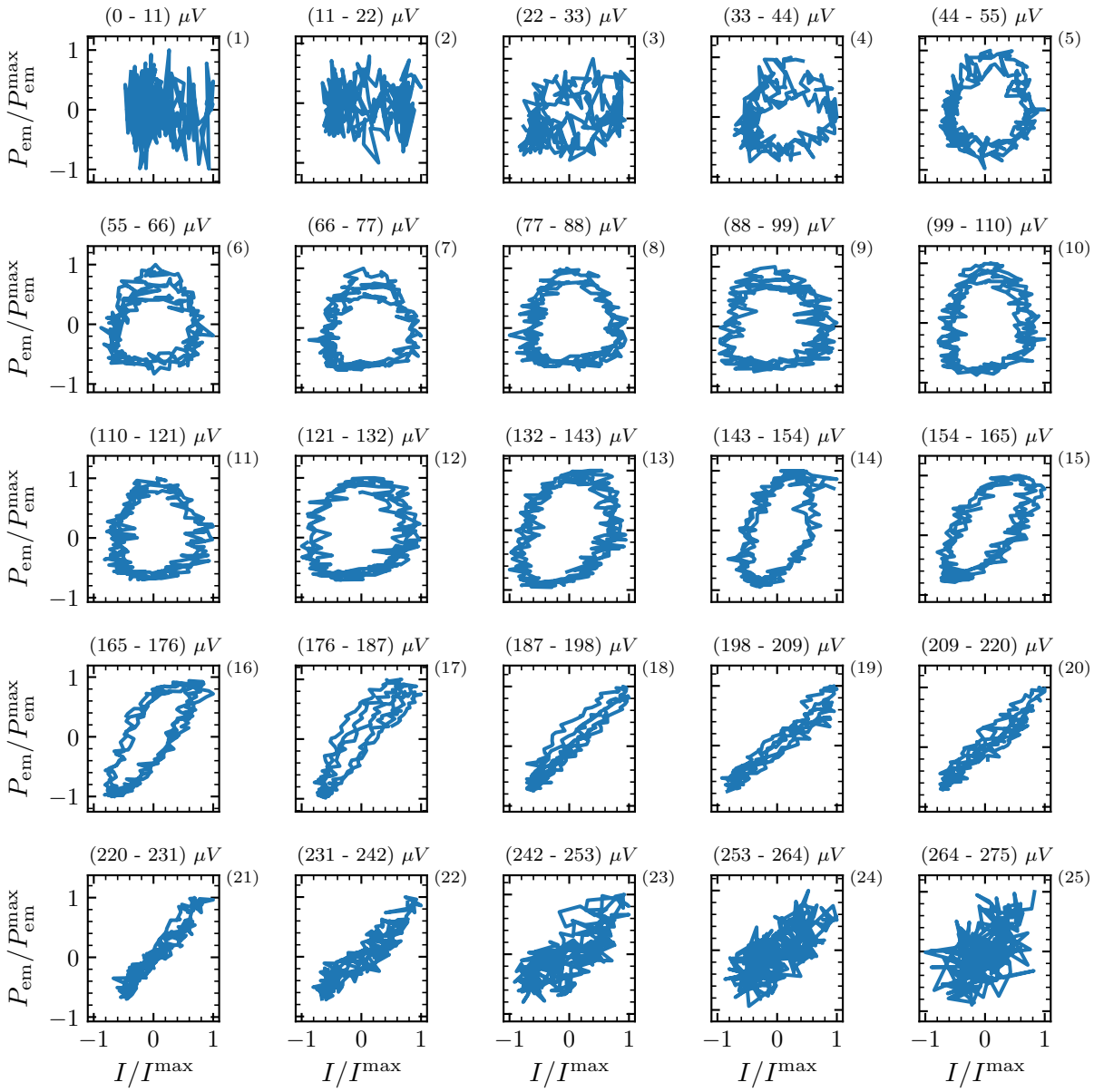

Figure 4.8: Normalized current versus normalized emission in different voltage ranges. At low voltage (below 190 µV) the two are out of phase while in the in the 190 µV to 240 µV range the curves are in phase.

4.2 Numerical simulation of the mode populations and current

In order to predict the occupation of the different modes and the current through the junction, we have to solve a multi-mode master equation, which becomes difficult when the number of modes exceeds four. In order to circumvent this problem, we first derive the equation giving the evolution of the Wigner W distribution in phase space. This equation is exact and contains the same information than the master equation for the density matrix and is still very hard to solve. However, by making the assumption that W varies slowly in phase space on a typical distance given by Λ_{CP}, we obtain a Fokker-Planck equation that can be efficiently simulated with classical stochastic trajectories even for a large number of modes. We show that this approach gives the same results than the quantum master equation in the case of two modes for parameters that are not very far from the experimental ones. We then show the predictions for six modes and compare them to our data. We manage to qualitatively reproduce the wide observed periodic structure

4.2.1 Multi-mode master equation

The Hamiltonian describing inelastic Cooper pair tunneling in our system can be written as [28]:

$$\hat{H} = \sum_n \hbar\omega_n \hat{a}_n^\dagger \hat{a} - E_J \cos(\hat{\Phi}_J). \tag{4.2}$$

The first term describes the resonant modes of the cavity while the second one is the Josephson Hamiltonian with E_J being the Josephson energy. The flux operator $\hat{\Phi}_J$ can be written as a sum of the dc voltage bias and the ac voltage of the resonator, leading to:

$$\hat{H} = \sum_n \hbar\omega_n \hat{a}_n^\dagger \hat{a} - \frac{E_J}{2}\left(e^{\sum_n i\Lambda_{n,\mathrm{cp}}(\hat{a}_n+\hat{a}_n^\dagger)-i\omega_J t} + \mathrm{h.c.}\right). \tag{4.3}$$

Here $\Lambda_{n,\mathrm{cp}} = 2\sqrt{2\tilde{Z}_n/R_K}$ is the n-th mode cavity-junction coupling[2], that depends on the mode effective impedance $\tilde{Z}_n$, while $\omega_J = 2eV/\hbar$ is the Josephson frequency set by the voltage bias. For a given mode, the matrix element of the displacement operator $e^{i\Lambda_n(\hat{a}_n+\hat{a}_n^\dagger)}$ can be again written in the Fock state basis using generalized Laguerre polynomials, as done in equation 3.17. The variation of the matrix elements with low m and l is shown in fig. 3.12.

The state of the cavity is described by its density matrix ρ, whose evolution is given by the master equation:

$$\dot{\rho} = -\frac{i}{\hbar}\left[\hat{H},\rho\right] + \sum_n \left[\kappa_n(n_n^{th}+1)\left(\hat{a}_n\rho\hat{a}_n^\dagger - \frac{1}{2}\left\{\hat{a}_n^\dagger\hat{a}_n,\rho\right\}\right) + \kappa_n n_n^{th}\left(\hat{a}_n^\dagger\rho\hat{a}_n - \frac{1}{2}\left\{\hat{a}_n\hat{a}_n^\dagger,\rho\right\}\right)\right], \tag{4.4}$$

with n_n^{th} being the number of thermal photons of the n-th mode. It is given by the Bose-Einstein distribution:

$$n_n^{th} = \frac{1}{e^{\hbar\omega_n/(k_B T)}-1}. \tag{4.5}$$

[2]From now on we will drop the subscript *cp* and will always refer to the coupling between cavity and Cooper pair degree of freedom.

The Josephson term is time dependent and this time dependence cannot be easily gauged away with a unitary transformation. One could try to use a rotating wave approximation to keep only the processes which are nearly resonant with the Josephson frequency [47], but, because the frequency of the different modes are nearly commensurate, there are in general many processes that are nearly resonant at a given voltage, which makes this approach rather complex. We have chosen to keep the time dependence and solve 4.4 for a sufficiently long time in order to reach the steady-state. Because the master equation is time dependent with a periodic dependence, the steady-state is not a stationary state but is also periodic with period $2\pi/\omega_J$. This has however no incidence on the populations of ρ that reach truly time independent asymptotic values, from which we compute the mean photon number per mode.

In order to solve 4.4, we use a Monte-Carlo wavefunction method, which is more efficient for systems with a large Hilbert space than the direct integration of the master equation [49]. In figure 4.9 and 4.10, we show the results of a simulation performed with two modes at $T = 0$. The simulation parameters are: $\omega_0 = 2\pi \times 1.9\,\mathrm{GHz}$, $\kappa_0 = 2\pi \times 25\,\mathrm{MHz}$, $\Lambda_0 = 1.16$, $\omega_1 = 2\pi \times 5.9\,\mathrm{GHz}$, $\kappa_1 = 2\pi \times 5\,\mathrm{MHz}$, $\Lambda_1 = 1.4$ and $E_J = 2\pi \times 200\,\mathrm{MHz}$. The Hilbert space for the $n = 0$ ($n = 1$) mode is truncated to the first 14 (20) Fock states. The current is deduced from the mean photon number per mode using the following equation

$$I = 2e \sum_n \kappa_n (\langle \hat{a}_n^\dagger \hat{a}_n \rangle - n_n^{th})(\omega_n/\omega_J), \tag{4.6}$$

This simulation qualitatively reproduces the periodic pattern that we experimentally observe at low voltages but fails to explain that this pattern extends for a wide voltage range.

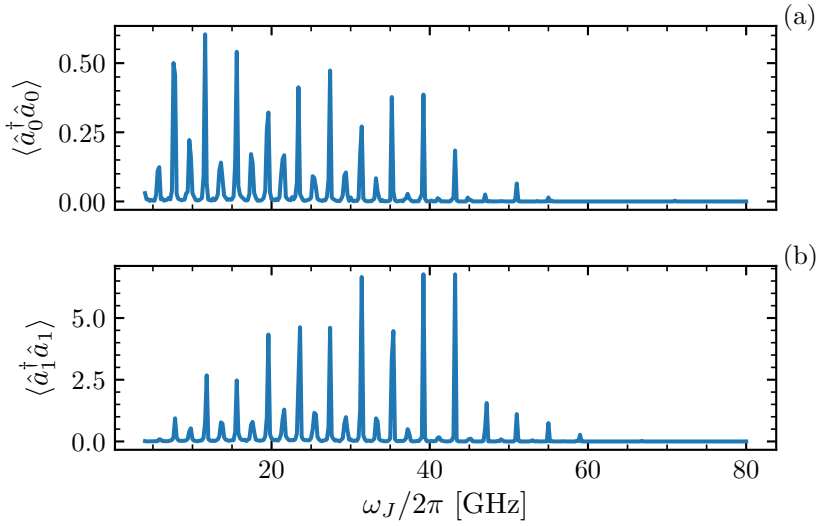

Figure 4.9: Mean photon number for the (a) $n = 0$ and (b) $n = 1$ mode obtained by solving the time dependent master equation, at $T = 0$, using the Monte Carlo wavefunction method.

4.2.2 Phase space method

We have just seen that two modes are not sufficient to explain emission and current at high voltages. But the numerical solution of the master equation becomes intractable when the

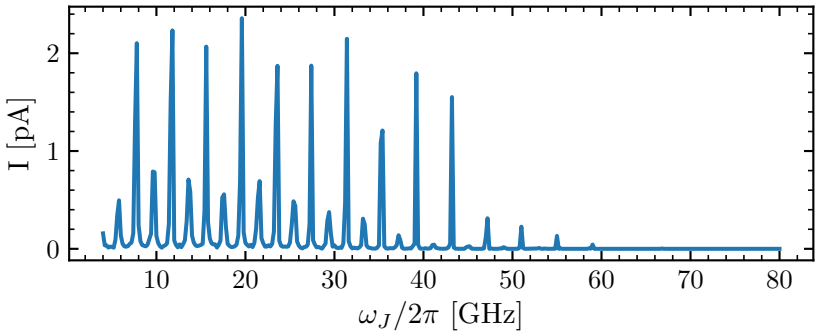

Figure 4.10: Tunneling current calculated from the mean photon number plotted in 4.9

number of modes is greater than four, even with the Monte-Carlo wavefunction method. A standard approach in quantum optics to obtain an easier numerical problem is to replace the quantum evolution by a stochastic evolution of the mode amplitudes considered as classical degree of freedom and to average over many realizations of this evolution. This approach is exact if the master equation can be transformed into a Fokker-Planck equation for a given phase space distribution, such as the Wigner distribution.

Here, we want to show that the classical equation of motions obtained by replacing the a_n operators in the Hamiltonian by classical degrees of freedom can lead to a reasonable estimate of the Wigner distribution. These equations are given by

$$\begin{aligned}\dot{a}_n &= -\frac{i}{\hbar}\frac{\partial H}{\partial a_n^\dagger} - \frac{\kappa_n}{2}a_n + \sqrt{\gamma_n}\xi_n \\ &= -i\omega_n a_n + i\Lambda_n E_J \sin\left(\omega_J t - \sum_n \Lambda_{n,\mathrm{cp}}(\hat{a}_n + \hat{a}_n^\dagger)\right) - \frac{\kappa_n}{2}a_n + \sqrt{\gamma_n}\xi_n,\end{aligned} \tag{4.7}$$

where the ξ_n are independent noise terms accounting both for quantum and thermal fluctuations. In order to justify this approach, we first rewrite the master equation 4.4 in terms of the Wigner distribution. We follow the calculation presented in [50, 51] and we start by introducing the characteristic symmetric function

$$\chi_S(z) = \mathrm{Tr}\left[\rho \prod_n e^{i(z_n^* \hat{a}_n^\dagger + z_n \hat{a}_n)}\right], \tag{4.8}$$

with $z = \{z_0, z_1, \ldots, z_n\}$. The equation of motion for the characteristic function is given by

$$\begin{aligned}\frac{\partial \chi_S}{\partial t} &= \mathrm{Tr}\left[\dot{\rho}\prod_n e^{i(z_n^*\hat{a}_n^\dagger + z_n\hat{a}_n)}\right] \\ &= \sum_n \left[-\left(i\omega_n + \frac{\kappa_n}{2}\right) z_n \frac{\partial}{\partial z_n} + \left(i\omega_n - \frac{\kappa_n}{2}\right) z_n^* \frac{\partial}{\partial z_n^*} - \kappa_n n_n^{th} z_n z_n^*\right]\chi_S + \\ &+ i\frac{E_J}{2}\prod_n \left[e^{\frac{\Lambda_n}{2}(z_n - z_n^*)} - e^{\frac{\Lambda_n}{2}(z_n^* - z_n)}\right]\left[\chi_S(z-\Lambda) - \chi_S(z+\Lambda)\right].\end{aligned} \tag{4.9}$$

The first terms correspond to the standard evolution for bare modes, while the last one describes the interaction between the modes due to the Josephson term. Here, we have used the property that commutators of displacement operators $D_n(i\Lambda_n) = \exp(i\Lambda_n(\hat{a}_n + \hat{a}_n^\dagger))$ can be written as

$$[D_n(iz_n^*), D_n(i\Lambda_n)] = \left(e^{\frac{\Lambda_n}{2}(z_n^* - z_n)} - e^{\frac{\Lambda_n}{2}(z_n - z_n^*)}\right) D_n(iz_n^* + i\Lambda_n). \tag{4.10}$$

The Wigner distribution is given by the Fourier transform of χ_S:

$$W(x,y) = \frac{1}{\pi^{2n}} \int dz_1 \dots dz_n \, \chi_S \prod_n e^{-iz_n(x_n - iy_n)} e^{-iz_n^*(x_n + iy_n)}. \tag{4.11}$$

Using this definition, we can rewrite 4.9 as:

$$\begin{aligned}\frac{\partial W(x,y)}{\partial t} = \frac{E_J}{2}\sin\left(\omega_J t - \sum_n 2\Lambda_n x_n\right)[W(x, y-\Lambda) - W(x, y+\Lambda)] + \\ + \sum_n \frac{\kappa_n}{2}\left[\frac{\partial}{\partial x_n}(x_n W(x,y)) + \frac{\partial}{\partial y_n}(y_n W(x,y))\right] + \\ + \sum_n \omega_n \left[\frac{\partial}{\partial y_n}(x_n W(x,y)) + \frac{\partial}{\partial x_n}(y_n W(x,y))\right] + \frac{1}{2}\sum_n \frac{\kappa_n}{2}\left(n_n^{th} + \frac{1}{2}\right)\left(\frac{\partial^2}{\partial x_n^2} + \frac{\partial^2}{\partial y_n^2}\right) W(x,y),\end{aligned} \tag{4.12}$$

with $x = \{x_0, x_1, \dots, x_n\}$ and $y = \{y_0, y_1, \dots, y_n\}$. This equation is still exact and fully equivalent to the master equation 4.4. However, it is not in the form of a Fokker-Planck equation and thus cannot be simulated by stochastic methods. We then make the following approximation:

$$W(x_n, y_n - \Lambda_n) - W(x_n, y_n + \Lambda_n) \simeq -2\Lambda_n \frac{\partial W(x,y)}{\partial y_n}. \tag{4.13}$$

This assumes that the Wigner function $W(x,y)$ varies in the phase space on a scale larger than Λ. This approximation is well justified at high temperatures but may not be true at low temperatures. Using 4.13, we obtain the following Fokker-Planck equation:

$$\frac{\partial W(x,y)}{\partial t} = -\sum_n \left(\frac{\partial A_n}{\partial x_n} + \frac{\partial B_n}{\partial y_n}\right) W(x,y) + \frac{1}{2}\sum_n \left(\frac{\partial^2}{\partial x_n^2} + \frac{\partial^2}{\partial y_n^2}\right) D_n W(x,y) \tag{4.14}$$

with:

$$A_n = \omega_n y_n - \frac{\kappa_n}{2} x_n, \qquad D_n = \frac{\kappa_n}{2}\left(n_n^{th} + \frac{1}{2}\right),$$

$$B_n = -\omega_n x_n + \Lambda_n E_J \sin\left(\omega_J t - \sum_n \Lambda_n x_n\right) - \frac{\kappa_n}{2} y_n$$

Equation 4.14 is equivalent to the set of stochastic equations:

$$dx_n = \left(\omega_n y_n - \frac{\kappa_n}{2} x_n\right) dt + \sqrt{\frac{\kappa_n}{2}\left(n_n^{th} + \frac{1}{2}\right)}\, \xi_n^x \tag{4.15}$$

$$dy_n = \left(-\omega_n x_n - \frac{\kappa_n}{2} y_n - \Lambda_n E_J \sin\left(\omega_J t - \sum_n \Lambda_n x_n \right) \right) dt + \sqrt{\frac{\kappa_n}{2}\left(n_n^{th} + \frac{1}{2} \right)}\, \xi_n^y \quad (4.16)$$

with ξ_n^x and ξ_n^y being independent gaussian noises with a standard deviation given by $\sigma_n = \sqrt{\kappa_n(n_n^{th} + 0.5)/2}$. These equations can be efficiently simulated even for a large number of modes.

From the moments of the Wigner distribution, given by the solutions of equation 4.15 and 4.16, we compute the average of the symmetrically ordered products of $\hat{a}$ and $\hat{a}^\dagger$. This allow us to calculate the mean number of photons $\langle \hat{a}_n^\dagger \hat{a}_n \rangle$ for each mode.

To validate the solutions of the classical equation of motion and check the approximation of the truncated Wigner function, we compare the mean number of photons calculated by solving the master equation with the Monte Carlo wavefunction method (MWF) with the one obtained using the classical stochastic trajectories (CST). We do it for the two-mode cavity case we studied before and for several values of temperature T and Josephson energy E_J. The results are plotted in figure 4.11. We observe that at high temperatures, the two solutions coincide even for different values of E_J (4.11a, 4.11b and 4.11c). As the temperature decreases the mean number of photons calculated with the classical trajectories becomes smaller than the one obtained from the solution of the master equation and this difference is more accentuated at large bias. This is linked to the Wigner function approximation (equation 4.13) that is not valid at low temperature, where the variation of W happen on a scale of the order of Λ.

4.2.3 Comparison with experimental data

We now show the results obtained simulating the cavity field using the classical stochastic equations discussed before and we compare them to the experimental data. In the simulation, we consider the first six strongly coupled modes and we use, as parameters, the results derived from Sonnet and discussed in 1.4 and 3.4.7. Below, we report the table with frequencies and coupling of the considered modes. The Josephson energy is fixed to $E_J/h = 710\,\text{MHz}$ (see appendix B) while the coupling rate of all the modes is chosen $\kappa_n = 2\pi \times 1\,\text{MHz}$, with the exception of the first mode, whose coupling is $\kappa_0 = 2\pi \times 25\,\text{MHz}$.

	$\omega_n/2\pi$ [GHz]	Λ_n
n = 0	1.89	1.28
n = 1	5.91	1.5
n = 3	15.54	0.9
n = 5	25.34	0.7
n = 7	35.09	0.6
n = 9	44.34	0.54

Table 4.1: Parameters of the modes used for the simulation.

The results for the mean number of photons of the $n = 1$ mode are shown in figure 4.12a. Here we can distinguish 82 emission peaks spaced by approximately $2\pi \times (1.96 \pm 0.02)\,\text{GHz}$ and with a width of $2\pi \times (530 \pm 30)\,\text{MHz}$. As mentioned before, the main period of the structure, is linked to the frequency of the strongest coupled mode, which is the $n = 1$. Every fourth peak is in fact spaced by ω_1. The width of the peaks is, instead, smaller than

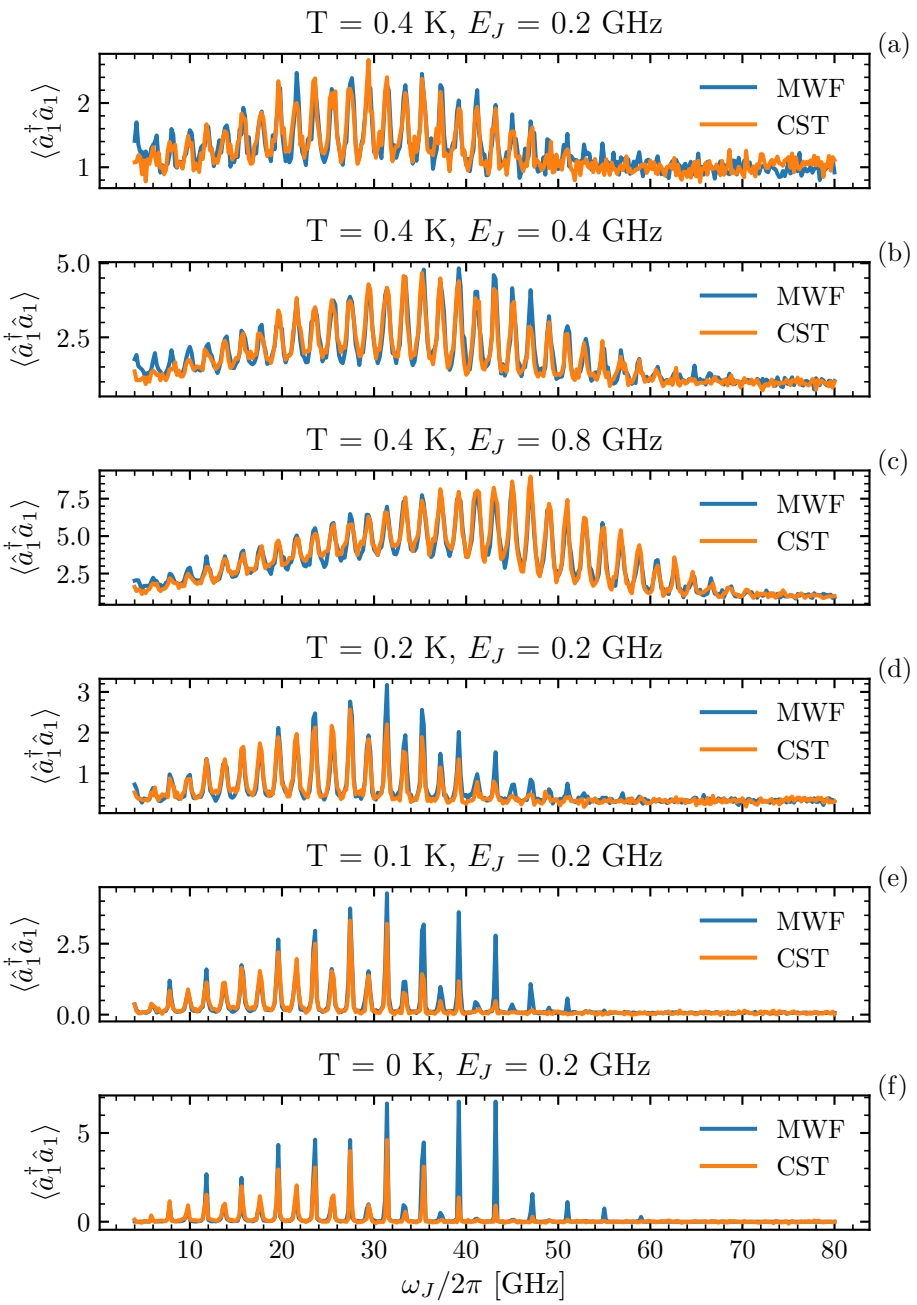

Figure 4.11: Comparison between the simulated mean number of photons for a two-mode cavity

the one measured experimentally ($\simeq 1.45\,\text{GHz}$). This could be due to voltage noise that we have neglected so far. We take it into account, by convolving the results of the simulation with a gaussian of variance σ_V. We find that the widths of the peaks of the data match the ones of the simulation when $\sigma_V = 0.8\,\mu\text{V}$. The simulated noisy spectrum is shown in figure 4.12b.

Because we didn't had time to perform a calibration of the gain, we cannot compare the

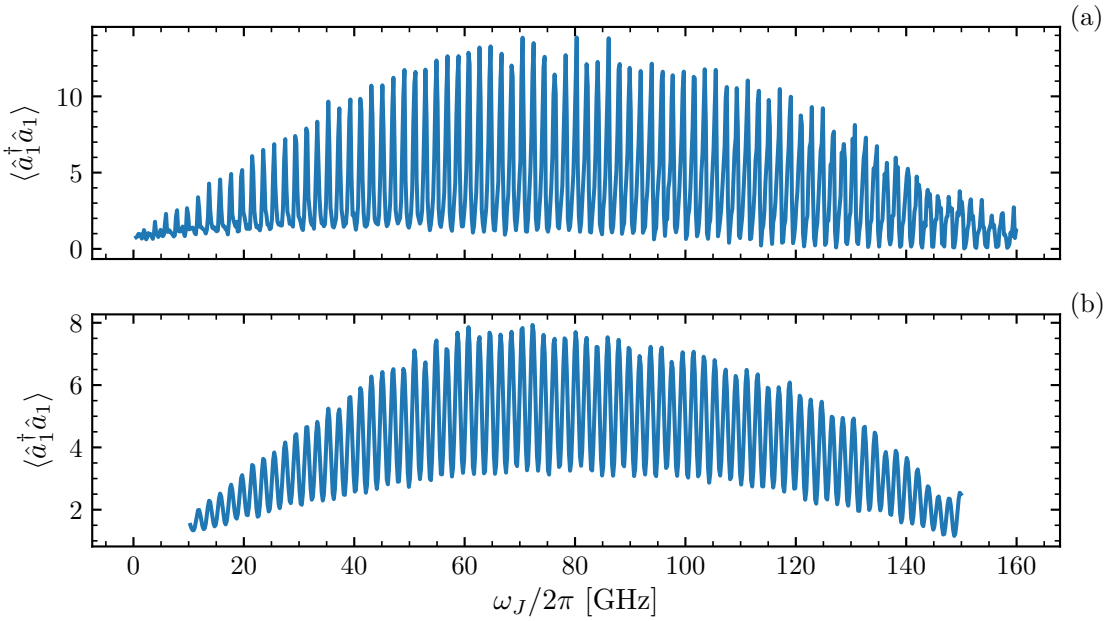

Figure 4.12: (a) Results of the simulation for the mean number of photons of mode $n = 1$ using the parameters of table 4.1. Panel (b) shows the same curve of (a) but with the assumption of gaussian voltage noise with $\sigma_V = 0.8\,\mu\text{V}$

simulated number of photons with the emission intensity. We can do so, however, for the supercurrent that we plot in figure 4.13 together with the data.

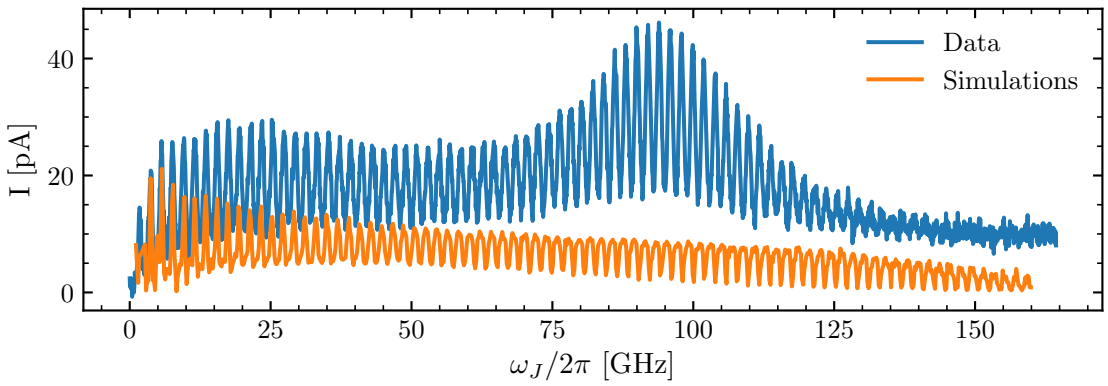

Figure 4.13: Comparison between measured supercurrent and the one simulated using the parameters of table 4.1.

We observe that the amplitude of the simulated curve is smaller than the experimental data and that not all the peaks of the two curves are in phase. We find that to better explain the current we have to replace the frequency ω_1 with the measured emission frequency ω_{em} and we need to increase the damping rate of the modes with $n \geq 1$ to $\kappa_n = 2\pi \times 8\,\text{MHz}$. The resonant frequency of the high order modes is also adjusted by performing a new measurement

of the photo-assisted current as the one done in 3.4.6. The result of the simulations obtained using these parameters is shown in figure 4.14.

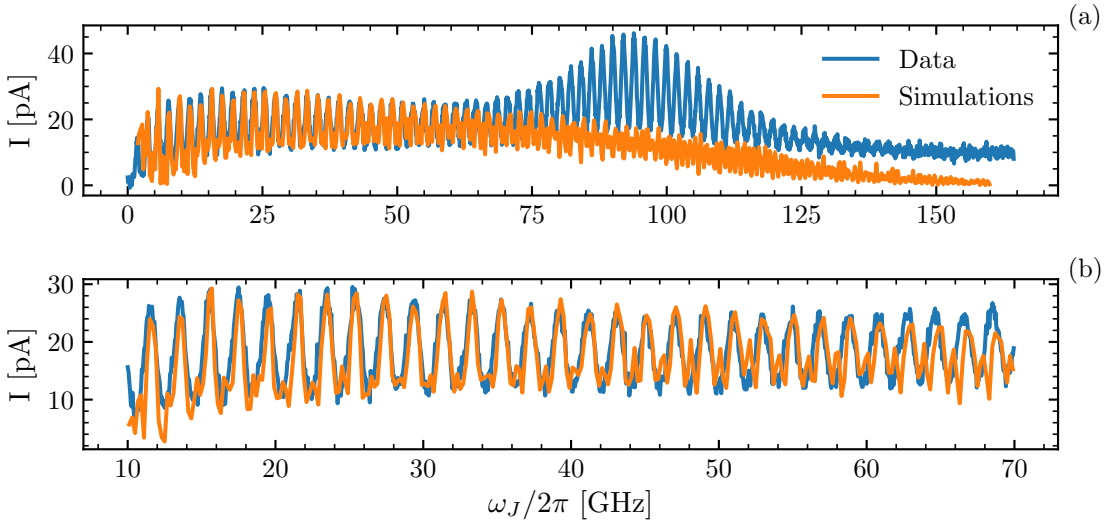

Figure 4.14: Simulated supercurrent compared with experimental data. The simulation is performed by replacing ω_1 with ω_{em} and by increasing the damping rate of the modes.

In this case there is a good agreement between data and simulations, especially when $V < 80\,\mu\text{V}$, as shown in 4.14b. At larger voltages the two curves do not coincide and the amplitude of the simulated current decreases. At high voltages, the presence of higher order modes ($n > 6$) that we neglected so far may be important. Also, as discussed in 4.2.2 this discrepancy may come from the fact that the classical stochastic approach is not valid at low temperature, especially at large bias (see figure 4.11).

Conclusions

In this chapter we showed measurements of emission of photons from the $n = 1$ mode of the cavity as a function of the voltage bias. We discussed how because of the large number of strongly coupled modes and of the high quality factor of the cavity, the emission is characterized by a periodic structure that is spread across the whole superconducting gap with a period that is connected to the resonant frequency ω_1. To prove that multi-mode effect are non negligible we measured the dc current flowing through the junction and we showed how not every current peak corresponds to an emission peak in the $n = 1$ mode and that hence also other modes must be populated.

To describe the experimental data, because of the large Fock space needed for the simulations, we used a phase space method that consists in writing the master equation in the form of a Fokker-Planck equation. This correspondence can be made when the Wigner function varies in phase space on a scale which is large compared to Λ. We have shown how this approximation is well verified at large temperature but not so much at lower temperatures when V is large. Even using this method, having a good quantitative agreement between simulations and data is not easy seen the large number of parameters involved in the simulations. Nonetheless by simulating the classical stochastic equations for a six modes cavity we obtained numerical results that are in qualitative agreement with the measurements.

Conclusions and perspectives

This thesis work aimed to study the quantum dynamics of a microwave cavity strongly coupled to a Josephson junction. To reach the strong coupling regime, where quantum effects are non negligible, the characteristic impedance of the resonating modes of the cavity has to be comparable to the quantum resistance R_K. We achieved this condition by micro-fabricating cavities using two high kinetic inductance superconductors: NbSi and granular Aluminum. We focused, in particular, on the last one and we designed a cavity having a 6 GHz mode with a characteristic impedance of 4.5 kΩ and a coupling rate to the measurement line of 450 kHz (chapter 1). These parameters put our experiment in a regime where the combination of quantum and nonlinear effects had to be taken into account to describe the state of the cavity.

We have shown that, when the junction is biased close to the superconducting gap, where quasiparticle tunneling can happen, a description of the evolution of the modes, that relies on the master equation treatment, is needed (chapter 3). We have, in fact, observed Fock state dependent single photon processes: we measured a different Lamb shift for the $|1\rangle$ and $|2\rangle$ states and we showed how the dynamics of the cavity can be confined to the $|0\rangle$ and $|1\rangle$ states. We have been able to explain these effects treating the junction as an environment, to which the cavity, described as an open quantum system, is coupled.

At voltages smaller than the superconducting gap, we have measured the photon emission due to inelastic Cooper pair tunneling (chapter 4) and we have shown how high order nonlinear processes, as well as the presence of more than one mode strongly coupled to the junction, cause a nontrivial dependence of the cavity field as a function of the voltage. To explain the data, we used a semi-classical approach that consists in using classical stochastic equation of motion to simulate quantum trajectories. By doing so we could efficiently calculate the state of the cavity considering a large number of modes. Because of time limitations however, we could not investigate more the interaction between the cavity and the Cooper pairs degree of freedom and numerical simulations on how the Josephson hamiltonian modifies the spectrum of the cavity modes are still needed.

Since this was the first experiment of this kind performed in our group, several improvements, regarding both the design of the sample and the measurement setup can be made. The first one concerns replacing the junction with a SQUID in order to have the possibility of tuning the Josephson energy E_J. This would allow us to reduce the number of photons emitted by the junction near the superconducting gap and to perform a better characterization of the quantum state of the cavity when its dynamics are confined to a Fock space of limited size. Measurement of the second order correlation function, for example, were not made possible by the fluctuations of the field caused by the Josephson emission. Tuning E_J could also help us in the characterization of the emission spectrum measured at lower voltages. The second change is linked to the coupling rate of the cavity to the measurement line.

Now that we have a better understanding of how the intrinsic loss rate of the modes changes as a function of the voltage it appears clear that an higher κ_c would have helped in having a better signal to noise ratio. Regarding the microwave setup, having a larger measurement bandwidth could allow for the measurement of other cavity modes. We have seen how the presence of spectator modes has a big impact both on the evolution of the properties of the cavity and on the emission spectra. Having a characterization of these modes could simplify the analysis of the measured data.

As follow-up of this experiment, a system where the cavity is coupled to NIN or SIN junctions can be studied. A research direction of our group is to use high impedance cavity coupled to a tunnel junction as a single microwave photon detector or to study the finite frequency quantum admittance of mesoscopic system. In a broader perspective, this thesis work confirms the great potential of high kinetic inductance superconductors for the realization of qubit [52], parametric amplifiers [53] or for the engineering of quantum states of light [54] or for the realization of quantum phase-slip junctions [55].

Appendix A

Mattis-Bardeen conductance

The Mattis Bardeen theory [56] describes the electrodynamics properties of superconductors in the microwave regime. It allows, starting from the knowledge of the superconducting gap Δ and of the normal state conductance σ_n, to express the complex conductivity $\sigma = \sigma_1 - i\sigma_2$ as a function of microwave frequency and temperature:

$$\frac{\sigma_1}{\sigma_n} = \frac{2}{\hbar\omega}\int_{\Delta}^{\infty} \frac{[f(E) - f(E+\hbar\omega)](E^2 + \Delta^2 + \hbar\omega E)}{\sqrt{E^2 - \Delta^2}\sqrt{(E^2 + \hbar\omega^2) - \Delta^2}} dE, \tag{A.1}$$

$$\frac{\sigma_2}{\sigma_n} = \frac{1}{\hbar\omega}\int_{\Delta-\hbar\omega}^{\Delta} \frac{[1 - 2f(E+\hbar\omega)](E^2 + \Delta^2 + \hbar\omega E)}{\sqrt{\Delta^2 - E^2}\sqrt{(E^2 + \hbar\omega^2) - \Delta^2}} dE, \tag{A.2}$$

where Δ can be approximated by:

$$\Delta(T) \simeq 1.74\Delta_0\sqrt{1 - \frac{T}{T_c}}, \tag{A.3}$$

with $\Delta_0 \simeq 1.76 k_B T_c$ being the superconducting gap at zero temperature and T_c the superconductor critical temperature.

These two equations are valid for frequencies below the superconducting gap ($\hbar\omega < 2\Delta$) and express the ratio between real and imaginary part of the complex conductivity σ and the normal metal conductivity σ_n. Here $f(E) = (1 + e^{E/k_B T})^{-1}$ is the Fermi-Dirac distribution function. The behavior of the two equations as a function of the reduced temperature and for different frequencies is shown in fig. A.1. Equation A.1 describes the dissipative part of the conductivity which is due to thermally excited quasiparticles. It, in fact, decreases with temperature and vanishes at $T = 0$. Since we are considering the case of $\hbar\omega < 2\Delta$, the contribution of photo-excited quasiparticles can be neglected. At low frequency, and below the critical temperature, σ_1 shows a peak, known as the coherence peak, which is due to a peak of the coherence factor that describes the scattering of a quasiparticle upon absorption of a photon of energy $\hbar\omega$ [57].

The equation A.2 gives the imaginary part of the conductivity and is responsible for the kinetic inductance. It is maximum at lower frequencies and decreases as temperature increases.

The complex conductivity σ is related to the surface impedance, which is defined as the ratio between the electric field and the current density integrated over the surface [58]. It can be

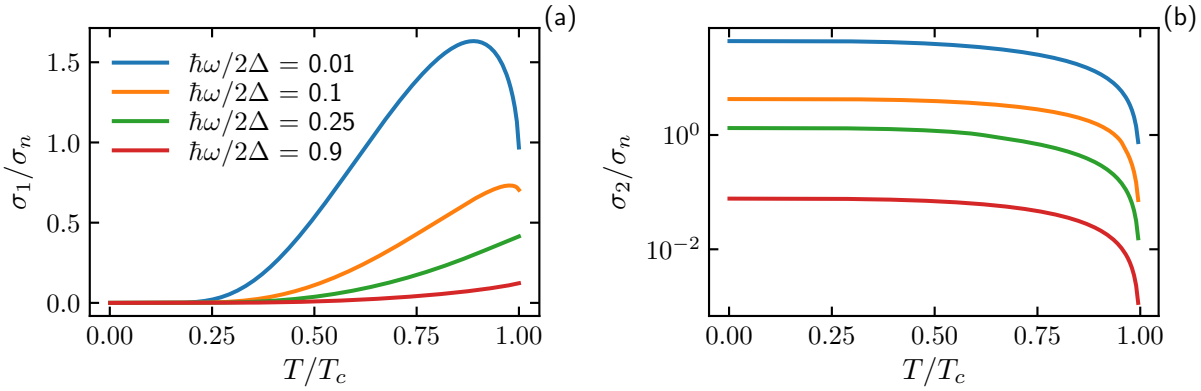

Figure A.1: Variation of the real (a) and imaginary (b) part of the complex conductivity as a function of the temperature for different frequencies.

written as a series of a resistance and of an inductance:

$$Z_s = R_s + i\omega L_k. \tag{A.4}$$

In the case of a thin superconducting film where the thickness t is smaller than the London penetration depth λ_L, the surface impedance can be written as [58]:

$$Z_s = \frac{1}{t\sigma} = \frac{1}{t(\sigma_1 - i\sigma_2)}, \tag{A.5}$$

giving a surface resistance and a surface kinetic inductance equal to:

$$R_s = \frac{\sigma_1}{t(\sigma_1^2 + \sigma_2^2)}, \tag{A.6}$$

$$L_k = \frac{\sigma_2}{t\omega(\sigma_1^2 + \sigma_2^2)}. \tag{A.7}$$

These two equations, together with equations A.1 and A.2, completely define the superconductor surface resistance and its kinetic inductance. They allow us to predict how the resonant frequency and the intrinsic losses of a resonator change with temperature and frequency.

Another variable that can change the electrodynamics properties of a superconductor is the DC bias current. To explain how this happen we need to express the dependence of the superconducting gap Δ on the current I and we can do so by following the derivation presented in [59]. At zero temperature and in the dirty limit case (where the electronic mean free path l_e is smaller than the coherence length ξ and of the London penetration depth λ_L), the gap can be expressed as a function of the superconducting phase gradient φ as:

$$\Delta = \Delta_0 e^{-\pi\zeta/4}, \tag{A.8}$$

with $\zeta = D\varphi^2/(2\Delta)$ and D being the diffusion coefficient. In this case Δ_0 refers to gap at zero temperature and zero bias current.

By writing the current density as a function of the phase gradient it is possible to express the ratio of the bias current I to the critical one I_c as:

$$\frac{I}{I_c} = 1.897 e^{-3\pi\zeta/8} \sqrt{\zeta} \left(\frac{\pi}{2} - \frac{2}{3}\zeta \right). \tag{A.9}$$

By solving this equation for ζ, for a given ratio of I/I_c, and by using equation A.8 we can find the dependence of Δ with respect to I. As shown in fig. A.2 the gap decreases as the bias current approaches the critical one up to reaching a minimum value of around $0.8\Delta_0$ when $I = I_c$.

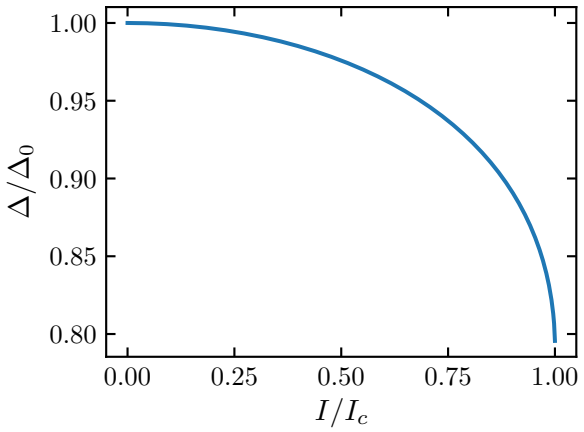

Figure A.2: Reduced gap as a function of the reduced bias current.

By plugging this reduced gap in equations A.1 and A.2 we can find the dependence of the complex conductivity on the bias current.

Appendix B

Junction resistance and Josephson energy

To evaluate the junction normal resistance and its Josephson energy, we monitor the total resistance of the sample, which include also the normal resistance of the cavity's metal, as function of the temperature during a cooldown.

From the data shown in figure B.1 we can distinguish two superconducting transitions happening at two different critical temperatures. The first one, at $T \simeq 1.85\,\mathrm{K}$, is the one of the granular aluminum of the cavity, while the second one, close to $T \simeq 1.3\,\mathrm{K}$, is the superconducting transition of the aluminum junction. In between these two temperatures we measure the normal resistance of the junction that is $R_N = 220\,\mathrm{k}\Omega$.

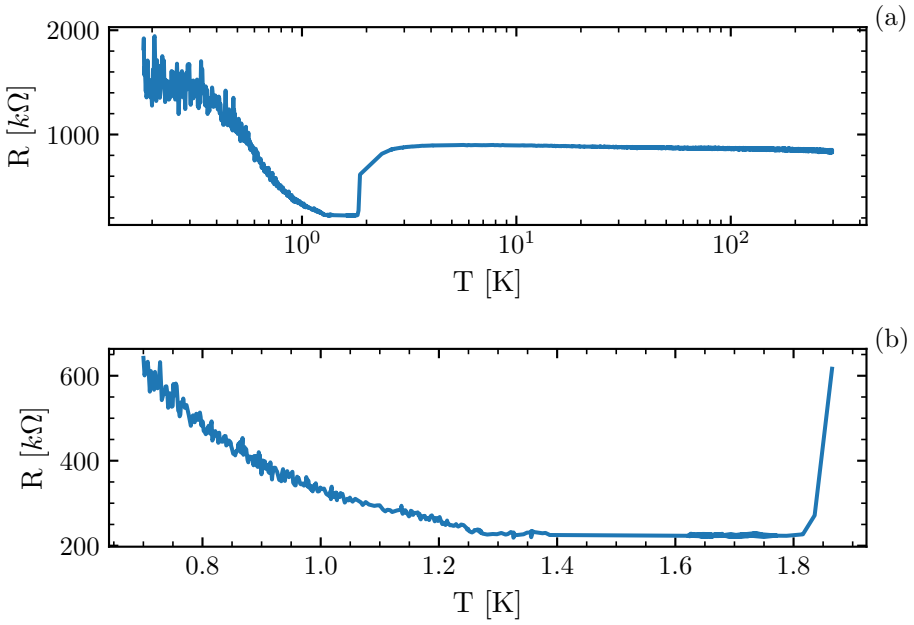

Figure B.1: Resistance of the sample as a function of the temperature measured during a cooldown of the fridge. Panel (a) shows the variation from 300 K to 10 mK, while panel (b) is a zoom close to the two superconducting transitions

Using Ambegaokar-Baratoff relation [60] for the estimation of the junction critical current I_c:

$$I_c \simeq \frac{\pi\Delta}{2eR_N}, \tag{B.1}$$

we get $I_c \simeq 1.4\,\mathrm{nA}$ with a Josephson energy $E_J = \Phi_0 I_c/(2\pi h) \simeq 705\,\mathrm{MHz}$. The value of Δ used is the one derived experimentally in chapter 3 of $2\Delta/e = 397\,\mu\mathrm{V}$.

Using the value of the junction resistance we can also estimate the room temperature normal resistance of the granular aluminum of the cavity. This is equal to $616\,\mathrm{k}\Omega$, which corresponds to a resistance per square of $770\,\Omega/\square$. Using equation A.7 and the critical temperature of 1.85 K we obtain a kinetic inductance for the granular aluminum of $L_k = 570\,\mathrm{pH}/\square$. This value is close to the one we obtain from the analysis of the resonant frequency of the low coupled modes (3.4).

Appendix C

Measurement of the statistical moments of the cavity field

In microwave experiments, the average power of the cavity signal is too small to be measured directly and for this reason, typical microwave detection setups, as the one described in 2.3.2, involve the use of amplifiers. For properly characterizing the measured field, it is important to know the effect that these amplifiers have on the cavity quantum field $\hat{a}$.

A generic phase-insensitive amplifier transforms the quantum field in the following way [61]:

$$\hat{a} \rightarrow \sqrt{G}\hat{a} + \sqrt{G-1}\hat{h}^{\dagger}_{\text{amp}}, \tag{C.1}$$

with G being the gain of the amplifier and $\hat{h}^{\dagger}_{\text{amp}}$ a bosonic mode that describes the amplifier added noise. If G is sufficiently big ($G \gg 1$) the field after the amplification stage can be written as:

$$S = \hat{a} + \hat{h}^{\dagger} \tag{C.2}$$

The S field commutes with its conjugate and behaves like a classical variable given by the two quadratures of the measured field:

$$S = X_S + iY_S \tag{C.3}$$

Since the noise power of the amplifier is much bigger than the average power of a photon exiting from the cavity, we are interested in describing how to extract the cavity field $\hat{a}$ from the measurement of the field S. We follow the theory presented in [42], where it is shown that the statistical moments of the measured distribution are linked to the moments of the cavity field through:

$$\langle (S^{\dagger})^n S^m \rangle = \sum_{i,j=0}^{n,m} \binom{m}{j} \binom{n}{i} \langle (\hat{a}^{\dagger})^i \hat{a}^j \rangle \langle \hat{h}^{n-i} (h^{\dagger})^{m-j} \rangle. \tag{C.4}$$

If the cavity is in vacuum, all the moments with $\langle (\hat{a}^{\dagger})^n \hat{a}^n \rangle$, with $n \neq m$, are zero and the set of equations C.4 simply reduces to:

$$\langle (S^{\dagger})^n S^m \rangle_{|0\rangle\langle 0|} = \langle \hat{h}^n (\hat{h}^{\dagger})^m \rangle. \tag{C.5}$$

Performing a reference measurement with the cavity in vacuum allows to measure the anti-normally ordered modes of the $\hat{h}$ field. Once the moments $\langle \hat{h}^n (\hat{h}^{\dagger})^m \rangle$ are known, it is possible

to solve the set of equations C.4 and obtain the normally ordered modes of the cavity field. The first three moments of the $\hat{a}$ field are given by:

$$\langle \hat{a} \rangle = \langle S \rangle - \langle \hat{h}^\dagger \rangle \tag{C.6}$$

$$\langle \hat{a}^\dagger \rangle = \langle S^\dagger \rangle - \langle \hat{h} \rangle \tag{C.7}$$

$$\langle \hat{a}^\dagger \hat{a} \rangle = \langle S^\dagger S \rangle - \langle \hat{h}\hat{h}^\dagger \rangle - \langle S \rangle \langle \hat{h} \rangle - \langle S^\dagger \rangle \langle \hat{h}^\dagger \rangle + 2\langle \hat{h} \rangle \langle \hat{h}^\dagger \rangle \tag{C.8}$$

To compute the contribution of the quantum fluctuations to the photon number one can either use equation C.6 and C.8 and calculate $\langle \hat{\tilde{a}}\hat{\tilde{a}}^\dagger \rangle$ as:

$$\langle \hat{\tilde{a}}^\dagger \hat{\tilde{a}} \rangle = \langle \hat{a}^\dagger \hat{a} \rangle - |\langle \hat{a} \rangle|^2, \tag{C.9}$$

or can compute the second order moments of the displaced field $\hat{\tilde{a}}$. This is defined as:

$$\hat{\tilde{a}} = \tilde{X}_S + i\tilde{Y}_S - (\tilde{X}_h + i\tilde{Y}_h), \tag{C.10}$$

with $\tilde{X}_{S,h}$ and $\tilde{Y}_{S,h}$ being the displaced quadratures of the measured signal and of the reference, obtained from:

$$\tilde{X}_{S,h} = X_{S,h} - \langle X_{S,h} \rangle, \tag{C.11}$$

$$\tilde{Y}_{S,h} = Y_{S,h} - \langle Y_{S,h} \rangle. \tag{C.12}$$

$\langle \hat{\tilde{a}}^\dagger \hat{\tilde{a}} \rangle$ can be therefore calculated as:

$$\langle \hat{\tilde{a}}^\dagger \hat{\tilde{a}} \rangle = \langle \tilde{X}_S^2 \rangle + \langle \tilde{Y}_S^2 \rangle - \langle \tilde{X}_h^2 \rangle - \langle \tilde{Y}_h^2 \rangle \tag{C.13}$$

Appendix D

Résumé

Le but de cette thèse est d'étudier la dynamique quantique d'une cavité de grande impédance caractéristique Z_c couplée galvaniquement à une jonction Josephson polarisée en tension. La jonction est caractérisée par une énergie Josephson E_J et une résitance à l'état normal R_N. La configuration expérimentale étudiée ici est décrite par le schéma de la figure D.1.

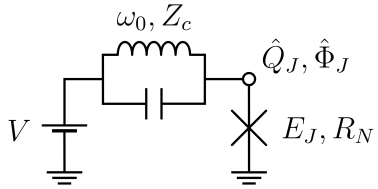

Figure D.1: Représentation schématique du circuit consistant en un résonateur LC, avec une impédance caractéristique Z_c et une fréquence de résonance ω_0, couplé galvaniquement à une jonction Josephson polarisée en tension, avec une énergie E_J et une résistance à l'état normal R_N.

Dans ce circuit, le mode électromagnétique du résonateur est couplé au transport des charges à travers le circuit. La population de photons dans le résonateur est affectée (création/ annihilation) par le passage par effet tunnel de paires de Cooper et/ou de quasiparticules. Le couplage entre le champ électromagnétique de la cavité et la jonction Josephson est lié aux fluctuations du vide de la cavité. Ces fluctuations de point zéro sont directement liées à l'impédance caractéristique du mode résonant. La tension vue par la jonction est, en fait, la somme de la polarisation continue V et de la tension ac du mode résonant. Ce dernier terme est directement proportionnel au rapport entre l'impédance caractéristique Z_c et le quantum de résistance $R_K = h/e^2 \approx 25.8\,\mathrm{k}\Omega$. Lorsque l'impédance caractéristique Z_c est comparable à R_K, le régime de couplage fort est atteint et les effets quantiques deviennent pertinents.

Pour comprendre comment le passage des charges par effet tunnel affecte la dynamique de la cavité, nous devons faire la distinction entre les deux processus tunnel possibles qui peuvent se produire dans une jonction Josephson. Dans le cas de l'effet tunnel des paires de Cooper, la présence d'un mode à la fréquence ω_0 entraîne un courant non nul en dessous du gap pour $2eV = \hbar\omega_0$. Ce courant correspond à l'effet tunnel inélastique des paires de Cooper : l'effet tunnel se produit en même temps que l'émission d'un photon dans le résonateur [24, 29]. La variation de charge à travers la jonction peut être exprimée en termes d'opérateur de déplacement de cavité comme :

$$e^{\frac{i}{\hbar}2e\hat{\Phi}_J} = e^{i\Lambda_{\mathrm{cp}}(\hat{a}+\hat{a}^\dagger)}. \tag{D.1}$$

Les opérateur $\hat{\Phi}_J$ et $\hat{Q}_J$ étant conjugués, le terme de gauche de l'équation D.1 correspond à l'opérateur de translation de la charge Q_J de $2e$. Le second terme est l'opérateur de déplacement de la cavité, écrit en termes d'opérateurs de création et d'annihilation de photons $\hat{a}^\dagger$ et $\hat{a}$ avec $\Lambda_{\mathrm{cp}} = 2\sqrt{\pi Z_c/R_K}$ étant le paramètre de couplage entre la cavité et la jonction. Chaque fois qu'une paire de Cooper traverse la jonction, l'état de la cavité est déplacé de Λ_{cp}. Par conséquent, la jonction agit comme une source pour la cavité chaque fois que la tension est en résonance avec la fréquence de résonance du mode $2eV = n\hbar\omega_0$ (avec n étant un nombre entier). De plus, dans le régime de couplage fort, si le taux d'amortissement de la cavité est beaucoup plus faible que l'énergie Josephson, le champ dans la cavité entre dans un régime hors d'équilibre et la théorie $P(E)$ [21] qui décrit habituellement le transport à travers la jonction n'est plus valable.

En l'absence de résonateur, le courant de quasi-particules à travers la jonction Josephson n'apparaît que si $V > 2\Delta/e$. Cependant, en présence d'un champs micro-onde dans la cavité, des processus photo-assistés peuvent apparaître. La jonction peut en effet absorber les photons stockés dans la cavité et un effet tunnel de quasi-particules photo-assisté peut se produire si $eV > 2\Delta - \hbar\omega_0$. Comme pour les paires de Cooper, lorsque la charge à travers la jonction change, l'état de la cavité est déplacé de $i\Lambda_{\mathrm{qp}}$, Λ_{qp} étant le paramètre de couplage pour le degré de liberté des quasiparticules ($\Lambda_{\mathrm{qp}} = \sqrt{\pi Z_c/R_K}$). Pour des valeur de V faibles devant le gap ($eV \ll \Delta$), le résonateur est à peine affecté par la jonction. Lorsque la tension dépasse $eV = 2\Delta - \hbar\omega_0$, la jonction absorbe des photons et le résonateur subit une augmentation des pertes intrinsèques. En raison des relations de causalité (Kramers-Kronig), l'augmentation du taux de perte de la cavité correspond à une variation de la fréquence de résonance du mode [27, 44]. Dans le régime de couplage faible, ce comportement peut être modélisé en considérant une admittance de jonction dépendant de la puissance [25]. Dans le régime de couplage fort ($\Lambda > 1$), la description classique décrivant la jonction comme un élément électrocinétique n'est plus valable. Les fluctuations du vide ont un effet prédominant et les niveaux d'énergie du résonateur subissent un déplacement (Lamb shift). Les échanges d'énergie entre le résonateur et la jonction dépendent de l'état quantique du champ électromagnétique dans la cavité. Cela signifie que différents états de Fock du résonateur subissent un décalage de Lamb différent et un taux d'échange de photons différent.

Cavités à haute impédance

Afin d'atteindre le régime de couplage fort, une cavité à haute impédance est nécessaire. Les résonateurs micro-ondes standards ont une impédance typique proche de $50\,\Omega$ et sont donc éloignés du régime quantique. La recherche de "superinductances", qui conduit à de grands Z_c, est devenue un axe de recherche important avec l'objectif à long terme de manipuler les signaux micro-ondes au niveau du photon unique en utilisant des tensions continues. Différentes voies ont été suivies, notamment des chaînes de jonctions Josephson [11–13], des structures à forte inductance électromagnétique [14], ou des supraconducteurs à forte inductance cinétique [15, 16].

Dans cette thèse, nous considérons cette dernière option et nous nous concentrons sur l'aluminium granulaire, un supraconducteur obtenu par le dépôt de Al dans une atmosphère contrôlée d'oxygène. Ce matériau a une résistivité beaucoup plus élevée ($\sim 10^3$) à tempéra-

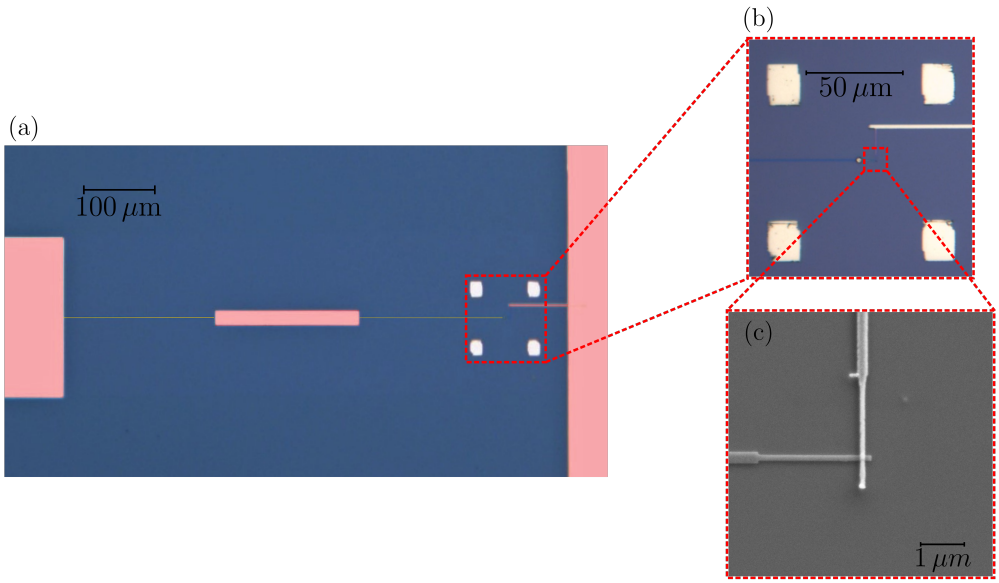

Figure D.2: (a) Image optique de la cavité quart d'onde en fausses couleurs. En rouge, nous colorons les parties en Al, c'est-à-dire la ligne 50 Ω à gauche, la deuxième section du Bragg et le plan de masse à droite. Les parties en jaune sont les parties en grAl : la première section du Bragg et la cavité $\lambda/4$. (b) Zoom du premier panneau à la position de la jonction. (c) Image MEB d'une jonction typique réalisée pour l'expérience.

ture ambiante que les supraconducteurs classiques. En conséquence, la densité des paires de Cooper à l'état supraconducteur est beaucoup plus faible et, pour un courant supraconducteur donné, l'énergie cinétique des paires est importante, donnant lieu à une inductance importante. Nous avons conçu une cavité quart d'onde d'onde couplée à une ligne de mesure 50 Ω à travers un réflecteur de Bragg distribué (DBR) (figure D.2). Le DBR est utilisé pour améliorer la réflectivité, et donc le facteur de qualité, de la cavité. Celui que nous avons réalisé est constitué de trois lignes, en géométrie 'microstrip', qui alternent haute et basse impédance. Le premier et dernier tronçon de la cavité sont réalisés en grAl et ont la même géométrie, tandis que le second est fabriqué en Al pur. En raison de la différence d'inductance des différentes lignes, la différence d'impédance est très élevée et est encore améliorée par l'utilisation de lignes de différentes largeurs. La jonction est une jonction Al/AlOx/Al avec $R_N \simeq 200\,\mathrm{k}\Omega$ placée à l'extrémité de la cavité et mise à la masse de l'autre côté. Avec cette conception, nous avons réussi à obtenir une cavité multimode dont le mode résonnant à 6 GHz, indiqué par ω_1, possède une impédance caractéristique de 4.8 kΩ, ainsi qu'un grand facteur de qualité ($\sim$ 20000). Ce mode n'est cependant pas le seul mode fortement couplé présent dans le circuit : les modes de cavité d'ordre élevé (jusqu'à 25 GHz) ont une impédance supérieure à 1 kΩ alors que le DBR fait en sorte qu'il existe un mode de haute impédance, de basse fréquence résonnant autour de 2 GHz.

Effet du passage tunnel des quasi-particules sur la dynamique de la cavité

Pour étudier l'interaction entre le résonateur et la jonction Josphson polarisée proche du gap ($eV \sim 2\Delta$), nous étudions le spectre en réflexion S_{11} du mode $\omega_1 \simeq 6\,\mathrm{GHz}$ de la cavité en fonction de la tension de polarisation de la jonction. Un tracé de $|S_{11}|^2$, mesuré à des tensions inférieures à $2\Delta/e$ ($\Delta \approx 200\,\mu\mathrm{eV}$), est présenté dans la figure D.3.

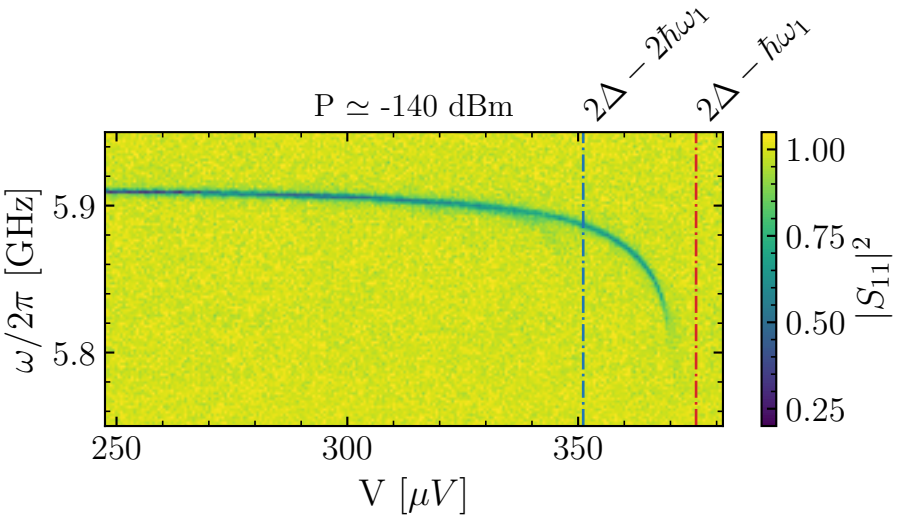

Figure D.3: $|S_{11}|^2$ mesuré à des tensions inférieures à $2\Delta/e$. La fréquence de résonance de la cavité diminue à mesure que la tension se rapproche de $2\Delta/e - \hbar\omega_1/e$ (ligne pointillée rouge). Une seconde résonance est visible à des tensions juste en dessous de $2\Delta/e - 2\hbar\omega_1/e$ comme indiqué par la ligne bleue.

Lorsque la valeur de la tension de polarisation s'approche de $2\Delta/e - \hbar\omega_1/e$ (ligne pointillée rouge), avec $\omega_1 \approx 2\pi \times 5.91\,\mathrm{GHz}$, la fréquence de résonance de la cavité subit un décalage négatif d'environ $2\pi \times 100\,\mathrm{MHz}$. Lorsque la tension de polarisation est supérieure à $eV > 2\Delta - \hbar\omega_1$, la jonction absorbe les photons de la cavité. Cela augmente le taux de perte intrinsèque, qui devient beaucoup plus important que le taux de couplage et fait disparaître la résonance.

Le spectre montre également l'apparition d'une faible résonance à des tensions proches de $2\Delta - 2\hbar\omega_1$ (ligne bleue pointillée). C'est une conséquence du régime de couplage fort qui fait que les niveaux d'énergie se déplacent différemment en fonction de la tension. Ici, les transitions $|0\rangle \rightarrow |1\rangle$ et $|1\rangle \rightarrow |2\rangle$ ont des fréquences de résonance différentes. Pour mieux sonder cette propriété, nous effectuons une mesure par spectroscopie à deux tons. Nous accordons le premier ton à la fréquence de transition ω_1^{10} et, en utilisant un second ton micro-ondes, nous mesurons S_{11} comme indiqué sur la figure D.4.

Cette fréquence de transition suit la même tendance que ω_1^{10} avec un décalage de fréquence négatif de $2\pi \times 40\,\mathrm{MHz}$ lorsque $eV \approx 2\Delta - 2\hbar\omega_1$ au lieu de $eV \approx 2\Delta - \hbar\omega_1$. La résonance disparaît à des tensions supérieures à $2\Delta/e - 2\hbar\omega_1/e$ (ligne bleue en pointillés). Là encore, cela est dû à l'absorption des photons par la jonction, pour des tensions supérieures à $2\Delta/e -$

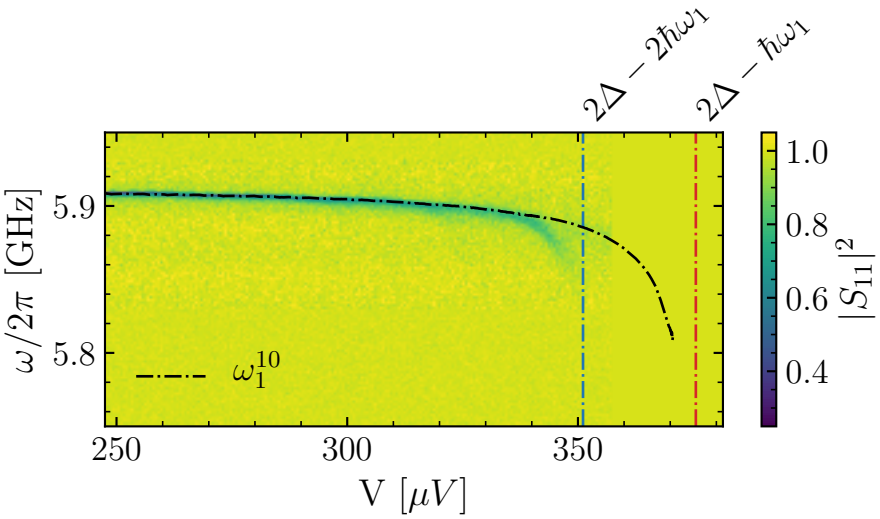

Figure D.4: $|S_{11}|^2$ mesuré avec la spectroscopie à deux tons. La première pompe est réglée sur la première fréquence de transition du niveau d'énergie (ligne noire en pointillés). Avec une seconde pompe, nous acquérons le spectre de la cavité.

$2\hbar\omega_1/e$, le passage tunnel de quasiparticules photo-assisté par l'absorption de deux photons est autorisé.

Une autre caractéristique découlant du régime de couplage fort est que, lorsque $2\Delta - 2\hbar\omega_1 < eV < 2\Delta - \hbar\omega_1$, l'état du champ électromagnétique dans le résonateur est réduit au sous-espace généré par les états $|0\rangle$ et $|1\rangle$. Ceci est dû au fait que seul le premier niveau d'énergie n'est pas affecté par la perte induite par la jonction et que la cavité se comporte donc comme un système à deux niveaux. Nous vérifions ce comportement en mesurant le champ moyen de la cavité $|\langle\hat{a}\rangle|^2$ en fonction du taux de pompage η (figure D.5) Dans la région de tension qui nous intéresse ($V = 363\,\mu\text{V}$), le champ moyen montre un effet de saturation qui est typique pour un système à 2 niveaux et qui n'est pas présent aux tensions plus basses.

Pour expliquer ces deux effets, nous utilisons la théorie présentée dans [31], où la jonction est traitée comme un environnement et le résonateur comme un système quantique ouvert. En partant du hamiltonien tunnel, nous dérivons l'équation maîtresse, dans le formalisme de Lindblad, pour la matrice de densité du champ électromagnétique de la cavité ρ et nous la résolvons numériquement pour obtenir l'état d'équilibre. Nos donnes sont en bon accord avec ce modéle.

Émission et courant de Josephson

En ce qui concerne l'effet tunnel inélastique des paires de Cooper à travers la jonction, nous mesurons l'émission de photons dans le mode à 6 GHz ainsi que le courant continu qui sont montrés dans la figure D.6.

Nous observons plus de 70 pics d'émissions et de courant, avec une structure périodique qui s'étend sur tout le gap. Cette caractéristique est liée à la combinaison de la haute

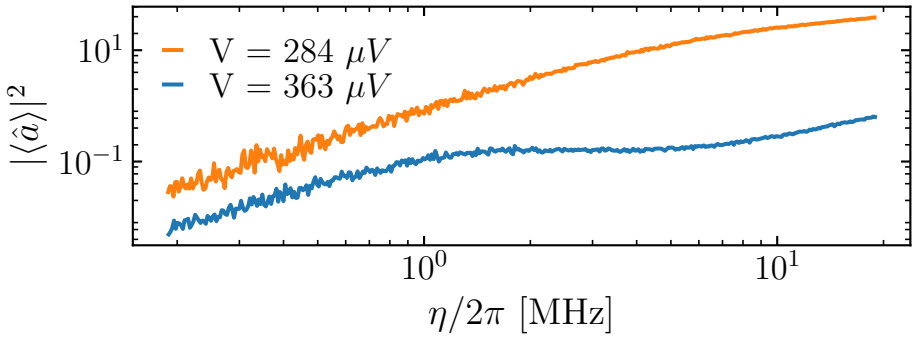

Figure D.5: Evolution du champ moyen dans la cavité en fonction de la puissance pour différentes tesion V. Lorsque $2\Delta - 2\hbar\omega_1 < eV < 2\Delta - \hbar\omega_1$, $|\langle\hat{a}\rangle|^2$ montre un effet de saturation comme dans un vrai TLS.

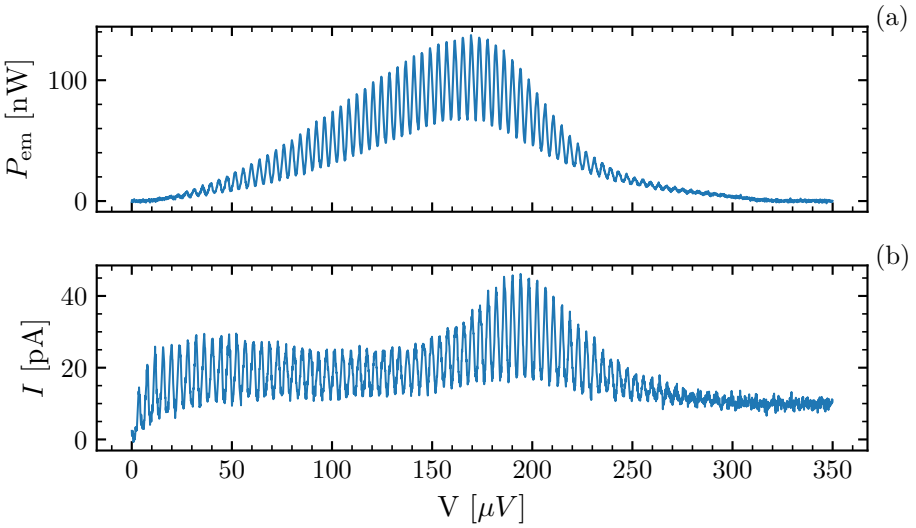

Figure D.6: (a) Puissance émise par la jonction à 6 GHz. (b) Courant à travers la jonction en fonction de la tension de polarisation.

impédance et du facteur de qualité élevé du mode à 6 GHz ainsi qu'à la structure multimode de la cavité. Aux basses tensions, nous attribuons cette structure périodique à des processus, où m_0 photons sont créés dans le mode $\omega_0 \approx 2$ GHz et m_1 photons dans le mode $\omega_1 \approx 6$ GHz. Ce processus est résonnant lorsque $2eV = \hbar(m_0\omega_0 + m_1\omega_1)$ et parce que $\omega_1 \approx 3\omega_0$, il donne lieu à une structure périodique avec une période $\omega_1/3 \approx \omega_0$ en termes de fréquence Josephson $2eV/\hbar$.

Cependant, la présence de deux modes n'explique pas quantitativement les données, surtout à haute tension. Pour mieux comprendre nos résultats, nous devons également prendre en compte les modes de haute fréquence. L'équation maîtresse multimode résultante devient cependant difficile à résoudre en raison de la croissance exponentielle de la dimension de l'espace de Hilbert avec le nombre de modes. Nous utilisons alors une tech-

nique souvent utilisée en optique quantique pour transformer l'équation maîtresse en une équation de Fokker-Planck dans l'espace des phases, qui peut être simulée avec des trajectoires stochastiques classiques. Cette transformation repose sur une approximation, qui n'est pas totalement justifiée pour notre système, mais qui nous permet d'obtenir des résultats numériques en accord qualitatif avec le courant continu et l'émission observés à 6 GHz.

Bibliography

[1] V. Bouchiat et al. "Quantum Coherence with a Single Cooper Pair". In: *Physica Scripta* T76.1 (1998), p. 165. DOI: 10.1238/physica.topical.076a00165.

[2] Y Nakamura, Yu A Pashkin, and J S Tsai. "Coherent control of macroscopic quantum states in a single-Cooper-pair box". In: *Nature* 398 (1999). DOI: 10.1038/19718.

[3] J. M. Martinis et al. "Rabi Oscillations in a Large Josephson-Junction Qubit". In: *Phys. Rev. Lett.* 89 (2002), p. 117901. DOI: 10.1103/PhysRevLett.89.117901.

[4] J. Koch et al. "Charge-insensitive qubit design derived from the Cooper pair box". In: *Phys. Rev. A* 76 (2007), p. 042319. DOI: 10.1103/PhysRevA.76.042319.

[5] A. Wallraff et al. "Strong coupling of a single photon to a superconducting qubit using circuit quantum electrodynamics". In: *Nature* 431.7005 (2004), pp. 162–167. DOI: 10.1038/nature02851.

[6] J. M. Fink et al. "Climbing the Jaynes-Cummings ladder and observing its $\sqrt{n}$ nonlinearity in a cavity QED system". In: *Nature* 454.7202 (2008), pp. 315–318. DOI: 10.1038/nature07112.

[7] M. Hofheinz et al. "Synthesizing arbitrary quantum states in a superconducting resonator". In: *Nature* 459.7246 (2009), pp. 546–549. DOI: 10.1038/nature08005.

[8] A. Blais et al. "Quantum-information processing with circuit quantum electrodynamics". In: *Phys. Rev. A* 75 (2007), p. 032329. DOI: 10.1103/PhysRevA.75.032329.

[9] T. Walter et al. "Rapid High-Fidelity Single-Shot Dispersive Readout of Superconducting Qubits". In: *Phys. Rev. Applied* 7 (2017), p. 054020. DOI: 10.1103/PhysRevApplied.7.054020.

[10] F. Arute et al. "Quantum supremacy using a programmable superconducting processor". In: *Nature* 574 (2019), pp. 505–510. DOI: 10.1038/s41586-019-1666-5.

[11] D. B. Haviland and P. Delsing. "Cooper-pair charge solitons: The electrodynamics of localized charge in a superconductor". In: *Phys. Rev. B* 54 (10 1996), R6857–R6860. DOI: 10.1103/PhysRevB.54.R6857.

[12] C. Altimiras et al. "Tunable microwave impedance matching to a high impedance source using a Josephson metamaterial". In: *Applied Physics Letters* 103.21 (2013). DOI: 10.1063/1.4832074.

[13] L. Planat et al. "Fabrication and Characterization of Aluminum SQUID Transmission Lines". In: *Phys. Rev. Applied* 12.6 (2019), p. 064017. DOI: 10.1103/PhysRevApplied.12.064017.

[14] Chloe Rolland. "Strong coupling quantum electrodynamics of a voltage biased Josephson junction". PhD thesis. Université Lille 1, 2016.

[15] C. A. Marrache-Kikuchi et al. "Thickness-tuned superconductor-insulator transitions under magnetic field in a-NbSi". In: *Physical Review B* 78.14 (2008), pp. 1–6. DOI: 10.1103/PhysRevB.78.144520.

[16] N. Maleeva et al. "Circuit quantum electrodynamics of granular aluminum resonators". In: *Nature Communications* 9.1 (2018), pp. 1–7. DOI: 10.1038/s41467-018-06386-9. eprint: 1802.01859.

[17] M. H. Devoret et al. "Effect of the electromagnetic environment on the Coulomb blockade in ultrasmall tunnel junctions". In: *Physical Review Letters* 64.15 (1990), pp. 1824–1827. DOI: 10.1103/PhysRevLett.64.1824.

[18] S. M. Girvin et al. "Quantum fluctuations and the single-junction Coulomb blockade". In: *Physical Review Letters* 64.26 (1990), pp. 3183–3186. DOI: 10.1103/PhysRevLett.64.3183.

[19] D. V. Averin, Yu. V. Nazarov, and A. A. Odinstov. "Incoherent tunneling of the cooper pairs and magnetic flux quanta in ultrasmall Josephson junctions". In: *Physica B: Physics of Condensed Matter* 165-166 (1990), pp. 945–946. DOI: 10.1016/S0921-4526(09)80058-6.

[20] A. A. Odintsov, G. Falci, and G. Schön. "Single-electron tunneling in systems of small junctions coupled to an electromagnetic environment". In: *Physical Review B* 44.23 (1991), pp. 13089–13092. DOI: 10.1103/PhysRevB.44.13089.

[21] M. H. Devoret and H. Grabert. *Single Charge Tunneling: Coulomb Blockade Phenomena In Nanostructures*. Springer US, 1992. ISBN: 978-1-4757-2166-9.

[22] P. Delsing et al. "Effect of high-frequency electrodynamic environment on the single-electron tunneling in ultrasmall junctions". In: *Phys. Rev. Lett.* 63.11 (1989), pp. 1180–1183. DOI: 10.1103/PhysRevLett.63.1180.

[23] A. N. Cleland, J. M. Schmidt, and J. Clarke. "Influence of the environment on the Coulomb blockade in submicrometer normal-metal tunnel junctions". In: *Phys. Rev. B* 45.6 (1992), pp. 2950–2961. DOI: 10.1103/PhysRevB.45.2950.

[24] M. Hofheinz et al. "Bright side of the coulomb blockade". In: *Physical Review Letters* 106.21 (2011), p. 217005. DOI: 10.1103/PhysRevLett.106.217005.

[25] A. H. Worsham et al. "Quantum tunneling currents in a superconducting junction". In: *Phys. Rev. Lett.* 67 (1991), pp. 3034–3037. DOI: 10.1103/PhysRevLett.67.3034.

[26] J. Basset, H. Bouchiat, and R. Deblock. "Emission and absorption quantum noise measurement with an on-chip resonant circuit". In: *Physical Review Letters* 105.16 (2010), p. 166801. DOI: 10.1103/PhysRevLett.105.166801.

[27] M. Silveri et al. "Broadband Lamb shift in an engineered quantum system". In: *Nature Physics* 15.6 (2019), pp. 533–537. DOI: 10.1038/s41567-019-0449-0.

[28] V. Gramich et al. "From Coulomb-Blockade to Nonlinear Quantum Dynamics in a Superconducting Circuit with a Resonator". In: *Physical Review Letters* 111.24 (2013), p. 247002. DOI: 10.1103/PhysRevLett.111.247002.

[29] C. Rolland et al. "Antibunched Photons Emitted by a dc-Biased Josephson Junction". In: *Physical Review Letters* 122.18 (2019), p. 186804. DOI: 10.1103/PhysRevLett.122.186804.

[30] O. Parlavecchio et al. "Fluctuation-Dissipation Relations of a Tunnel Junction Driven by a Quantum Circuit". In: *Phys. Rev. Lett.* 114 (12 2015), p. 126801. DOI: 10.1103/PhysRevLett.114.126801.

[31] J. Estève, M. Aprili, and J. Gabelli. "Quantum dynamics of a microwave resonator strongly coupled to a tunnel junction". In: (2018). arXiv: 1807.02364.

[32] S. M. Girvin. *Circuit QED: Superconducting Qubits Coupled to Microwave Photons*. Oxford Scholarship Online, 2014. ISBN: 978-0-199-68118-1.

[33] W. E. Smith. "Energy and dispersion in electromagnetic systems". In: *Australian Journal of Physics* 18 (Aug. 1965), p. 287. DOI: 10.1071/PH650287.

[34] C. G. Montgomery, R. H. Dicke, and E. M. Purcell. *Principles of Microwave Circuits*. Institution of Electrical Engineers, 1987. ISBN: 978-0-863-41100-7.

[35] D. M. Pozar. *Microwave Engineering*. 4th ed. Wiley, 2012. ISBN: 978-0-470-63155-3.

[36] R. P. Clayton. *Analysis of Multiconductor Transmission Lines*. 2nd ed. Wiley, 2007. ISBN: 978-0-470-13154-1.

[37] R. P. Clayton. *Inductance: Loop and Partial*. 1st ed. Wiley, 2010. ISBN: 978-0-470-46188-4.

[38] O. Crauste et al. "Thickness dependence of the superconductivity in thin disordered NbSi films". In: *Journal of Physics: Conference Series* 150.4 (2009). DOI: 10.1088/1742-6596/150/4/042019.

[39] J Zmuidzinas. "Superconducting Microresonators: Physics and Applications". In: *Annual Review of Condensed Matter Physics* 3.1 (2012), pp. 169–214. DOI: 10.1146/annurev-conmatphys-020911-125022.

[40] J. M. Kreikebaum et al. "Improving wafer-scale Josephson junction resistance variation in superconducting quantum coherent circuits". In: *Superconductor Science and Technology* 33.6 (2020). DOI: 10.1088/1361-6668/ab8617.

[41] Cyril Vaneph. "Observation du phénomène de blocage anormal de photon dans le domaine micro-onde". PhD thesis. Université Pierre et Marie Curie, 2017.

[42] C. Eichler, D. Bozyigit, and A. Wallraff. "Characterizing quantum microwave radiation and its entanglement with superconducting qubits using linear detectors". In: *Phys. Rev. A* 86 (2012). DOI: 10.1103/PhysRevA.86.032106.

[43] Qing Hu et al. "Observation of nondissipative quasiparticle tunnel currents in superconducting tunnel junctions". In: *Phys. Rev. Lett.* 64 (1990), pp. 2945–2948. DOI: 10.1103/PhysRevLett.64.2945.

[44] J. Basset, H. Bouchiat, and R. Deblock. "High-frequency quantum admittance and noise measurement with an on-chip resonant circuit". In: *Phys. Rev. B* 85 (2012), p. 085435. DOI: 10.1103/PhysRevB.85.085435.

[45] J. R. Tucker and M. J. Feldman. "Quantum detection at millimeter wavelengths". In: *Rev. Mod. Phys.* 57 (1985), pp. 1055–1113. DOI: 10.1103/RevModPhys.57.1055.

[46] K. E. Cahill and R. J. Glauber. "Ordered Expansions in Boson Amplitude Operators". In: *Phys. Rev.* 177 (1969). DOI: 10.1103/PhysRev.177.1857.

[47] J. R. Souquet and A. A. Clerk. "Fock-state stabilization and emission in superconducting circuits using dc-biased Josephson junctions". In: *Physical Review A* 93.6 (2016), p. 060301. DOI: 10.1103/PhysRevA.93.060301.

[48] C. Cohen-Tannoudji, J. Dupont-Roc, and G. Grynberg. *Atom—Photon Interactions: Basic Process and Appilcations*. 2nd ed. Wiley, 2004. ISBN: 978-0-471-29336-1.

[49] K. Mølmer, Y. Castin, and J. Dalibard. "Monte Carlo wave-function method in quantum optics". In: *J. Opt. Soc. Am. B* 10.3 (1993), pp. 524–538. DOI: 10.1364/JOSAB.10.000524.

[50] H. Carmichael. *Statistical Methods in Quantum Optics 1*. Springer, 2002. ISBN: 978-3-642-08133-0.

[51] C. Gardiner and P. Zoller. *Quantum Noise: A Handbook of Markovian and Non-Markovian Quantum Stochastic Methods with Applications to Quantum Optics*. Springer, 2004. ISBN: 978-3-642-06094-6.

[52] L. Grünhaupt et al. "Granular aluminium as a superconducting material for high-impedance quantum circuits". In: *Nature Materials* 18.8 (2019). DOI: 10.1038/s41563-019-0350-3. eprint: 1809.10646.

[53] B. Ho Eom et al. "A wideband, low-noise superconducting amplifier with high dynamic range". In: *Nature Physics* 8.8 (2012), pp. 623–627. ISSN: 17452481. DOI: 10.1038/nphys2356.

[54] S. Puri, S. Boutin, and A. Blais. "Engineering the quantum states of light in a Kerr-nonlinear resonator by two-photon driving". In: *npj Quantum Information* 3.1 (2017), pp. 1–6. ISSN: 20566387. DOI: 10.1038/s41534-017-0019-1.

[55] J. E. Mooij and Yu V. Nazarov. "Superconducting nanowires as quantum phase-slip junctions". In: *Nature Physics* 2.3 (2006), pp. 169–172. ISSN: 17452481. DOI: 10.1038/nphys234.

[56] D. C. Mattis and J. Bardeen. "Theory of the anomalous skin effect in normal and superconducting metals". In: *Physical Review* 111.2 (1958), pp. 412–417. DOI: 10.1103/PhysRev.111.412.

[57] M. Tinkham. *Introduction to Superconductivity*. 2nd ed. Dover Publications, 2004. ISBN: 0486435032.

[58] J. I. Gittleman and B. Rosenblum. "Microwave Properties of Superconductors". In: *Proceedings of the IEEE* 52.10 (1964), pp. 1138–1147. DOI: 10.1109/PROC.1964.3301.

[59] A. J. Annunziata et al. "Tunable superconducting nanoinductors". In: *Nanotechnology* 21.44 (2010). DOI: 10.1088/0957-4484/21/44/445202.

[60] V. Ambegaokar and A. Baratoff. "Tunneling Between Superconductors". In: *Phys. Rev. Lett.* 10 (11 1963), pp. 486–489. DOI: 10.1103/PhysRevLett.10.486.

[61] A. A. Clerk et al. "Introduction to quantum noise, measurement, and amplification". In: *Rev. Mod. Phys.* 82 (2010). DOI: 10.1103/RevModPhys.82.1155.

université PARIS-SACLAY
ÉCOLE DOCTORALE
Physique en l'Île-de-France (PIF)

Titre: Dynamique quantique d'une cavité micro-onde à haute impédance fortement couplée à une jonction Josephson

Mots clés: Électrodynamique quantique des circuits, Supraconducteurs à haute impédance, Émission de Josephson, Décalage de Lamb

Résumé: Le but de cette thèse est d'étudier les propriétés et la dynamique d'une cavité micro-onde à haute impédance couplée galvaniquement à une jonction Josephson polarisée en tension. La cavité est réalisée en aluminium granulaire, un supraconducteur désordonné à haute inductance cinétique, qui nous a permis d'obtenir des modes avec un facteur de qualité élevé (jusqu'à 30 000) et une grande impédance caractéristique allant jusqu'à 5 kOhm dans la gamme du GHz. L'occupation et les propriétés des modes de la cavité sont fortement influencées par les processus tunnel se produisant dans la jonction connectée à la cavité. Comme l'impédance caractéristique des modes est comparable au quantum de résistance, des processus non linéaires d'ordre élevé sont observés. À basse tension par rapport au gap supraconducteur de la jonction, le processus dominant est le passage tunnel inélastique des paires de Cooper, qui peuple les différents modes de la cavité. Nous mesurons directement l'émission de photons dans un mode à 6 GHz et observons plus de 70 pics d'émission en fonction de la tension de polarisation, une signature claire de la non-linéarité élevée. Aux tensions plus élevées proches du gap, le tunneling des quasi-particules domine. Ce processus dissipatif modifie à la fois la fréquence de résonance et la largeur des modes. Un traitement quantique de ce processus dissipatif en termes de décalage de Lamb et de sauts quantiques est nécessaire pour expliquer quantitativement nos mesures. Ces résultats montrent le potentiel de l'aluminium granulaire pour réaliser des expériences d'optique quantique dans un régime où le transport de charge et les photons micro-ondes sont fortement couplés.

Title: Quantum dynamics of a high impedance microwave cavity strongly coupled to a Josephson junction

Keywords: Circuit quantum electrodynamics, High impedance superconductors, Josephson emission, Lamb shift

Abstract: The purpose of this thesis is to investigate the properties and the dynamics of a high impedance microwave cavity galvanically coupled to a DC biased Josephson junction. The cavity is realized in granular Aluminum, a disordered superconductor with high kinetic inductance, which allowed us to obtain modes with a high quality factor (up to 30000) and a large characteristic impedance up to 5 kOhm in the GHz range. The occupation and the properties of the cavity modes are strongly affected by the charge tunneling processes occurring in the junction connected to the cavity. Because the characteristic impedance of the modes is comparable to the quantum of resistance, high order non-linear processes are observed. At low voltages compared to the superconducting gap of the junction, the dominant process is the inelastic tunneling of Cooper pairs, which populates the different cavity modes. We directly measure the photon emission in one mode at 6 GHz and observe more than 70 emission peaks as a function of bias voltage, a clear signature of the high non-linearity. At larger voltages close to the gap, quasiparticle tunneling dominates. This dissipative process modifies both the resonance frequency and the linewidth of the modes. A quantum treatment of this dissipative process in terms of Lamb shift and quantum jumps is required to quantitatively explain our measurements. These results show the potential of granular Aluminum to realize microwave quantum optics experiments in a regime where charge transport and microwave photons are strongly coupled.

Université Paris-Saclay
Espace Technologique / Immeuble Discovery
Route de l'Orme aux Merisiers RD 128 / 91190 Saint-Aubin, France